Western Graduate&PostdoctoralStudies

Western University
Scholarship@Western

Electronic Thesis and Dissertation Repository

12-4-2017 10:30 AM

Investigation of ductile crack growth and normalization method for SE(T) specimen using finite element analyses

Cheng Qian
The University of Western Ontario

Supervisor
Zhou, Wenxing
The University of Western Ontario

Graduate Program in Civil and Environmental Engineering
A thesis submitted in partial fulfillment of the requirements for the degree in Master of Engineering Science
© Cheng Qian 2017

Follow this and additional works at: https://ir.lib.uwo.ca/etd

Part of the Structural Engineering Commons

Recommended Citation

Qian, Cheng, "Investigation of ductile crack growth and normalization method for SE(T) specimen using finite element analyses" (2017). *Electronic Thesis and Dissertation Repository*. 5046.
https://ir.lib.uwo.ca/etd/5046

This Dissertation/Thesis is brought to you for free and open access by Scholarship@Western. It has been accepted for inclusion in Electronic Thesis and Dissertation Repository by an authorized administrator of Scholarship@Western. For more information, please contact wlswadmin@uwo.ca.

ABSTRACT

The fracture toughness resistance curve (e.g. *J-R* curve) is widely used in integrity assessment and strain-based design of oil and gas pipelines with respect to planar defects (i.e. cracks). This thesis includes two-dimensional (2D) and three-dimensional (3D) finite element analyses (FEA) of ductile crack growth of X80-grade pipeline steel based on the Gurson-Tvergaard-Needleman (GTN) constitutive model, and investigation of the normalization (NM) method to generate the *J-R* curve for the single-edge tension (SE(T)) specimen.

First, the GTN model implemented in the computational cell is adopted in the commercial software ABAQUS to calibrate the micromechanical parameters for the pipeline steel. Subsequently, the stable fracture process of six SE(T) and four single-edge bend (SE(B)) specimens tested are simulated in 3D and 2D FEA. Results have shown that the GTN model is a viable tool to predict the fracture behavior of the specimens, in terms of predicting the load-displacement curve, *J-R* curve and crack front profile of the fracture specimen. In addition, the stress field near the crack-tip as well as various constraint parameters are examined.

Second, based on the calibrated micromechanical parameters, a series of SE(T) specimens with various geometric configurations are modelled. The applicability of the NM method to generate *J-R* curves for SE(T) specimens is investigated, followed by the proposal of the so-called '*k* factor-based NM method' based on the *J*-CMOD relationship, to improve the computational efficiency of the conventional NM method.

The outcomes of this study will facilitate and improve the evaluation of *J-R* curves for the SE(T) specimen using the NM method.

Keywords

Pipeline; Fracture toughness; *J-R* curve; GTN model; Finite element analysis; Stress field; Constraint parameter; SE(T) specimen; (*k* factor-based) normalization method

DEDICATION

To my mother and grandmother

ACKNOWLEDGEMENTS

My deepest gratitude goes first and foremost to my supervisor Dr. Wenxing Zhou. It is his profound insight, great guidance, and continuous patience that walked me through my entire journey of the graduate study. The completion of this thesis would not have been possible without his insightful and helpful comments. Dr. Wenxing Zhou has always been encouraging me in my confusing days. His rigorous research attitude, respectable dignity and every beautiful spirit will always influence my whole life.

I would also like to thank Dr. Timothy Newson, Dr. Ayman Mohamed El Ansary and Dr. Takashi Kuboki for being my examiners. Their constructive advice makes the final thesis complete. Special thanks to Dr. Yifan Huang for his valuable guidance on the software and fundamentals for my research. The financial support provided by TransCanada and the Natural Sciences and Engineering Research Council of Canada (NSERC) and by the Faculty of Engineering at Western University is much acknowledged.

Grateful thanks are expressed to the faculty and staff, especially to Dr. Michael Bartlett, Dr. Craig Miller, Dr. Robert Klassen, Dr. Ashraf El Damatty, Dr. Aiham Adawi and Ms. Kristen Edwards. My special thanks to all my colleagues in my research group for their help on my academic journey. I would like to thank my friends, Dr. Yu Guo, Daoping Guo, Wei Xiang, Sarah Stevenson and Ji Bao for their continuous support.

Finally, I want to thank my mother and grandmother for bringing me up, giving me endless love and being always supportive in every step of my life.

CONTENTS

ABSTRACT i

DEDICATION ii

ACKNOWLEDGEMENTS iii

CONTENTS iv

List of Figures viii

List of Tables xii

List of Abbreviations and Symbols xiii

Chapter 1 Introduction 1

  1.1 Background 1

  1.2 Fundamentals of fracture mechanics 1

    1.2.1 Overview 1

    1.2.2 Fracture mechanisms 2

    1.2.3 Linear elastic fracture mechanics 3

    1.2.4 Elastic plastic fracture mechanics 6

    1.2.5 Fracture toughness resistance curve 11

    1.2.6 Resistance curve test methods 14

    1.2.7 Constraint effects 14

  1.3 Research objectives and significance 15

  1.4 Thesis format and outline 16

Chapter 2 Literature Review: Mechanism and modelling of ductile fracture 17

2.1 Approaches to analyze ductile fracture 17

2.1.1 Global approach 17

2.1.2 Local approach 17

2.2 Physical damage mechanism of ductile material 19

2.3 GTN model for dilatant plasticity 21

2.3.1 Yield condition and flow rule 21

2.3.2 Void nucleation 24

2.3.3 Void growth 26

2.3.4 Void coalescence 27

2.4 Computational cell methodology 31

2.5 Micromechanical parameters 33

2.5.1 Overview 33

2.5.2 *q*-parameters 34

2.5.3 In-plane length scale D 34

2.5.4 Initial VVF f_0 37

2.5.5 Critical VVF f_C 38

2.5.6 VVF at failure f_F 39

2.5.7 Nucleation strain ε_N 40

2.5.8 Void volume fraction of nucleated voids f_N 41

2.5.9 Standard deviation of nucleation strain s_N 42

2.5.10 Out-of-plane length scale D_Z 43

2.6 Application of the Gurson model 43

Chapter 3 Numerical modelling of ductile crack growth 46

3.1 Previous test results 46

3.2 Material property 48

3.3 Finite element model and numerical procedure 49

3.3.1 Finite element model 49

3.3.2 Evolution of P, CMOD, CTOD, Δa, and J-integral 53

3.4 Calibration of micromechanical parameters 55

3.4.1 Calibration using 2D model of SE(B) specimen 55

3.4.2 Validation of calibrated micromechanical parameters 57

3.5 Numerical results and initiation toughness J_{IC} 61

3.6 Crack-tip stress fields 64

3.6.1 Overview 64

3.6.2 Opening stress distribution 65

3.7 Crack-tip constraint parameters 70

3.7.1 Overview 70

3.7.2 Constraint distribution ahead of the crack tip 71

3.7.3 Through-thickness constraint distribution 75

3.7.4 Relation between constraint parameters 80

Chapter 4 Normalization method for SE(T) specimen 83

4.1 Overview 83

4.2 Review of NM method 83

4.2.1 Procedure of NM method 83

4.2.2 Evolution of NM method 88

4.3 Validation of NM method for SE(T) specimens 92

4.4 *J*-CMOD relationship 99

4.4.1 *J*-CMOD relationship for test specimens 99

4.4.2 *J*-CMOD relationship for growing-crack FE models 100

4.4.3 *J*-CMOD relationship for stationary-crack FE models 101

4.5 Evaluation of *J* using CMOD and *k* 102

4.6 *k* equation 107

4.7 Validation of proposed *k* equation 108

4.8 *k* factor-based NM method 111

4.9 Evaluation of *J*-*R* Curve Using *k* factor-based NM method 111

Chapter 5 Summary, conclusions and recommendations 114

5.1 Summary 114

5.2 Conclusions 115

5.3 Recommendations 117

Appendix A 119

Appendix B 124

Appendix C 127

References 128

Curriculum Vitae 141

List of Figures

Fig. 1.1 Three loading modes in fracture mechanics 2

Fig. 1.2 Mechanism of brittle and ductile facture 3

Fig. 1.3 Stress field near the crack tip 4

Fig. 1.4 Elastic plastic and nonlinear elastic stress-strain relationships 7

Fig. 1.5 Schematic of *J*-integral 8

Fig. 1.6 Effect of plasticity on the crack-tip stress fields under SSY 10

Fig. 1.7 Schematic of CTOD definitions 11

Fig. 1.8 Schematic *J*-*R* curve for a ductile material 12

Fig. 1.9 Schematic of small-scale specimens 13

Fig. 1.10 A schematic illustration of constraint effect on fracture toughness 15

Fig. 2.1 Engineering approaches and models for ductile fracture 19

Fig. 2.2 Schematic of the micro-mechanisms of ductile fracture 20

Fig. 2.3 Yield surface dependence on the hydrostatic tension and porosity 22

Fig. 2.4 Homogenization treatment of void growth 27

Fig. 2.5 Schematic illustration of void coalescence 28

Fig. 2.6 Relation between f^* and f 29

Fig. 2.7 Schematic illustration of Eqs. (2.6), (2.7) and (2.8) (from 2D FEA) 29

Fig. 2.8 Modelling of ductile crack growth using CCM 31

Fig. 2.9 Micromechanical parameters 33

Fig. 2.10 Nucleation function A_1/f_N 42

Fig. 3.1 Geometric information of fracture specimens 47

Fig. 3.2 Stress-strain curves 48

Fig. 3.3 2D plane strain FE model of SE(B) specimen ($a_0/W = 0.25$) 51

Fig. 3.4 3D FE model of SE(T) specimen (SG, $a_0/W = 0.35$, $B/W = 1$) 53

Fig. 3.5 Determination of CMOD and CTOD 53

Fig. 3.6 P-CMOD curves and J-R curves for 2D SE(B) specimens with $a_0/W = 0.175$ ... 55

Fig. 3.7 P-CMOD curves and J-R curves for 2D SE(B) specimens with $a_0/W = 0.25$ 57

Fig. 3.8 P-CMOD curves and J-R curves for 3D SE(T) specimens 59

Fig. 3.9 Comparison of post-test measured and predicted crack front profiles 60

Fig. 3.10 P-CMOD and J-R curves for FE models 63

Fig. 3.11 Variation of fracture toughness (J_{IC} /$J_{1\mathrm{mm}}$/ $J_{1.5\mathrm{mm}}$) with a_0/W 64

Fig. 3.12 Distribution of $\sigma_{\theta\theta}/\sigma_0$ versus distance from initial crack tip at the mid-plane in stationary-crack analysis (PS, $B/W = 1$, $a_0/W = 0.2$, 0.35 and 0.5) 66

Fig. 3.13 Distribution of $\sigma_{\theta\theta}/\sigma_0$ versus distance from instantaneous crack tip at the mid-plane in growing-crack analysis (PS, $B/W = 1$, $a_0/W = 0.2$, 0.35 and 0.5) 67

Fig. 3.14 Distribution of $\sigma_{\theta\theta}/\sigma_0$ in the crack plane (PS, $a_0/W = 0.2$, $B/W = 1$) 68

Fig. 3.15 Distribution of $\sigma_{\theta\theta}/\sigma_0$ at $r\sigma_0/J = 2$ along the crack front for PS specimens 69

Fig. 3.16 Distribution of Q in the mid-plane for PS model (a_0/W = 0.2, 0.35 and 0.5, B/W = 1) at different loading levels (stationary-crack and growing-crack analyses) 72

Fig. 3.17 Distribution of A_2 in the mid-plane for PS model (a_0/W = 0.2, 0.35 and 0.5, B/W = 1) at different loading levels (stationary-crack and growing-crack analyses)............... 73

Fig. 3.18 Distribution of h in the mid-plane for PS model (a_0/W = 0.2, 0.35 and 0.5, B/W = 1) at different loading levels (stationary-crack and growing-crack analyses).................. 74

Fig. 3.19 Distribution of T_z in the mid-plane for PS model (a_0/W = 0.2, 0.35 and 0.5, B/W = 1) at different loading levels (stationary-crack and growing-crack analyses)............... 75

Fig. 3.20 Through-thickness distribution of Q for PS models.. 76

Fig. 3.21 Variation of Q parameter at mid-plane with a_0/W (PS, B/W = 1) 76

Fig. 3.22 Through-thickness distribution of A_2 for PS models.. 77

Fig. 3.23 Variation of A_2 parameter at mid-plane with a_0/W (PS, B/W = 1)..................... 77

Fig. 3.24 Through-thickness distribution of h for PS models... 78

Fig. 3.25 Variation of h parameter at mid-plane with a_0/W (PS, B/W = 1)....................... 78

Fig. 3.26 Through-thickness distribution of T_z for PS models.. 79

Fig. 3.27 Variation of T_z parameter at mid-plane with a_0/W (PS, B/W = 1)..................... 79

Fig. 3.28 Relation between Q-h 80

Fig. 3.29 Relation between Q-T_Z 81

Fig. 3.30 Relation between A_2-h 81

Fig. 3.31 Relation between A_2-T_Z.. 82

Fig. 4.1 Load-CMOD curve.. 84

Fig. 4.2 Normalized load versus normalized CMOD 86

Fig. 4.3 Normalization function shown fitted to the normalization data 87

Fig. 4.4 Data adjusted to place all points on the analytical NM function 87

Fig. 4.5 The resulting *J*-*R* curve 88

Fig. 4.6 Comparison of *J*-*R* curves obtained from UC method and NM method 95

Fig. 4.7 *J*-*R* curves obtained from UC method and NM method for 21 FE models 97

Fig. 4.8 J_N-V_N relationship for test specimens 99

Fig. 4.9 J_N-V_N relationship for GTN models with growing crack 100

Fig. 4.10 J_N-V_N relationship for stationary-crack PS FE models with $B/W = 1$ 102

Fig. 4.11 Variation of k with V_N for various a_0/W for PS FE models with $B/W = 1$ 104

Fig. 4.12 Variation of k with V_N for various n for PS FE models with $B/W = 1$ 105

Fig. 4.13 Variation of k with V_N for FE models with $n = 10$, various B/W and PS/SG .. 106

Fig. 4.14 Comparison of *J*-CMOD curves determined using η factor- and k factor-based methods for GTN models 109

Fig. 4.15 Variation of relative error e_{J2} with CMOD 109

Fig. 4.16 *J*-CMOD curves determined by the η factor- and k factor-based methods for test specimens 110

Fig. 4.17 *J*-*R* curves determined by UC method, conventional NM method and k factor-based NM method 113

List of Tables

Table 3.1 Specimen number 46

Table 3.2 Calibrated micromechanical parameters.. 56

Table 4.1 Crack lengths obtained from 9-point average technique and UC method........ 93

Table 4.2 Error of the predicted *J-R* curves using NM method for six test specimens 96

Table 4.3 Error of the predicted *J-R* curves using NM method for 21 FE models........... 98

Table 4.4 Coefficients α and β 107

Table 4.5 Values for *k* factor-based NM method.. 112

Table A. 1 Micromechanical parameters from literature.. 119

Table B. 1 Coefficients t_i for K_i 126

Table B. 2 Coefficients u_i for C_i 126

Table B. 3 Coefficients N_{ij} for η_{pl} 126

Table B. 4 Coefficients ψ_i for γ_{LLD}.. 126

Table C. 1 Coefficients of NM function for test SE(T) specimens 127

Table C. 2 Coefficients of NM function for GTN-based FE SE(T) models................... 127

List of Abbreviations and Symbols

A_{N1}, A_{N2}: Nucleation intensities due to plastic strain-controlled and stress-controlled nucleation, respectively

A_{pl}: Plastic area under the load-displacement record

A_2: Constraint parameter

a: Crack length

a_{bi}: Blunting corrected crack length

a_f: Final crack length

a_0: Initial crack length

B: Specimen thickness in z-direction

B_e: Effective specimen thickness which is used for elastic unloading compliance measurement of crack size

B_N: Net specimen thickness characterized by the distance between the roots of the side grooves in side-grooved specimens

b_0: Original remaining ligament from the original crack front to the back edge of the specimen, calculated as W-a_0

C: $\Delta V/\Delta P$, Crack mouth opening displacement compliance

C_i: Compliance of the deformed specimen

C_1, C_2: Power-law fitting coefficients for J-R curve

D: In-plane length scale of the computational cell

D_z: Out-of-plane length scale of the computational cell

D_1 and D_2: Fitting coefficient in the power-law and straight-line normalization function

d: Mean particle diameter in Roy's intercept method

d_n: Non-dimensional constant in estimating the in-plane length scale using critical CTOD

d_s: Infinitesimal arc length along the contour Γ

d_x, d_y, d_z: Average dimensions of the inclusion in Franklin's equation

E: Young's modulus

E_{2D}: Elastic modulus in the 2D analysis

e_{a1}: Relative error of initial crack lengths obtained from the UC method and 9-point average technique

e_{a2}: Relative error of final crack lengths obtained from the UC method and 9-point average technique

e_{a3}: Relative error of crack extensions obtained from the UC method and 9-point average technique

e_{J1}: Relative error of J-integral obtained by the UC and NM methods

e_{J2}: Relative error of J-integral obtained by the η-factor and k-factor based methods

F_r: Compliance rotation correction factor

f: Void volume fraction

$\dot{f}$: Rate of change of void volume fraction

f_0: Initial void volume fraction

f_C: Critical void volume fraction

f_F: Void volume fraction at failure

f_{gr}: Void volume fraction due to the growth of existing voids

$\dot{f}_{gr}$: Void volume fraction rate due to the growth of existing voids

f_{ij}: Dimensionless function in the calculation of stress fields at the crack tip using the stress intensity factor

f_N: Void volume fraction of nucleated voids

$f_{N\sigma}$: Void volume fraction of nucleated voids for stress-controlled nucleation

$f_{N\varepsilon}$: Void volume fraction of nucleated voids for plastic strain-controlled nucleation

f_{nucl}: Void volume fraction due to the nucleation of new voids

$\dot{f}_{nucl}$: Void volume fraction rate due to the nucleation of new voids

f_v: Volume fraction of particle

f^*: Modified void volume fraction

f_u^*: Ultimate value of f^*

G: Energy release rate

g_1, g_2: Quadratic functions in Cuesta et al.'s study

H: Daylight length (distance between grips)

h: Stress triaxiality

I_n: Integration constant in HRR solutions

i: Number of the loading step

J-integral: Elastic-plastic energy release rate which characterizes the local stress-strain field around the crack front

J_{IC}: The J-integral value at the beginning stage of material crack growth resistance development

J_k: J-integral determined by the k factor-based method

J_N: Normalized J-integral by the initial remaining ligament and effective yield strength

$J_{\mathrm{NM}\Delta a}$: J-integral determined by the NM method

J_{pl}: Plastic component of J-integral

J_Q: A preliminary estimate of J_{IC} characterized by the intersection of the regression J-R curve and the 0.2 mm-offset line

$J_{\mathrm{UC}\Delta a}$: J-integral determined by the UC method

J_η: J-integral determined by the η factor-based method

$J_{1\mathrm{mm}}$: The J-integral value at crack extension Δa=1 mm

$J_{1.5\mathrm{mm}}$: The J-integral value at crack extension Δa=1.5 mm

K or K_I: Stress intensity factor

K_{IC}: Critical stress intensity factor

k: Empirical factor that relates V_N to J_N

L, M, N and O: Fitting coefficients of the normalization function

l: Characteristic length parameter in defining A_2 parameter

l_m: Mean linear intercept in Roy's intercept method

l_0, l_1, l_2, l_{11}, l_{22}, l_{33}: Coefficients in Cuesta et al.'s study

m: Dimensionless constraint factor in J-CTOD relation

m_1, m_2: Line parameters in Cuesta et al.'s study

N_A: Areal density of voids

N_v: Number of carbides per unit length or per unit volume

n: Strain hardening exponent in the power-law fit

n_j: Component of the unit normal vector to Γ

n_{M1} and n_{M2}: Hardening exponents of material 1 and 2, respectively

$n_{R\text{-}O}$: Hardening exponent in Ramberg-Osgood stress-strain relationship

P: Applied force

P_{max}: Maximum load

P_N: Normalized force

P_Y: Limit load

Q: Constraint parameter

q_1, q_2, q_3: Constitutive parameters in GT(N) yield function

R: Radius of the cavity

R_0: Initial radius of the cavity

R^2: Coefficient of determination

$(R/R_0)_C$: Critical void growth ratio

r and θ: coordinates in the polar coordinate system originated from the crack-tip

r_p: Size of the plastic zone

r_{pll}: Void space ratio in the plastic limit load model

S: Specimen span

s_N: Standard deviation of nucleation strain

s_1, s_2 and s_3: Functions of the hardening exponent in defining A_2 parameter

T_i: Component of the traction vector on the contour Γ

T_Z: Constraint parameter

u_i: Components of the displacement vector

V: Crack mouth opening displacement

$(V_D)_C$: Critical void damage variable

V_{matrix}: Volume of matrix material

V_N: Normalized crack mouth opening displacement by initial crack length

V_{pl}: Plastic crack mouth opening displacement

V_{pl}': Normalized plastic crack mouth opening displacement

V_{void}: Void volume

W: Specimen width in y-direction

w: Strain energy density per unit volume

x, y, z: Cartesian coordinate system

Y: Geometry factor for the stress intensity factor

Γ: An arbitrary counter-clockwise path surrounding the crack-tip

$\mathit{\Gamma}_0$: Cohesive energy in cohesive zone model

$(\mathit{\Gamma}_0)_C$: Critical cohesive energy

Δa: Sum of stable crack extension and crack-tip blunting

Δa_b: Crack advance due to blunting

Δa_d: Crack extension due to ductile tearing

Δl: Punch displacement

α and β: Fitting coefficients in the proposed k factor-based normalization method

α_{coal}, β_{coal}: Fitting coefficients in the plastic limit load model

$\alpha_{R\text{-}O}$: Coefficient in the Ramberg-Osgood stress-strain relationship

δ: Crack tip opening displacement

δ_a: Accelerating factor in the modified void volume faction

δ_{IC}: Critical crack tip opening displacement at fracture initiation

δ_{ij}: Kronecker delta

ε: Strain

ε_N: Mean void nucleation strain

ε^{pl}: Plastic strain

$\dot{\varepsilon}^{pl}$: Plastic strain rate

ε_{ij}: Strain tensor, in which i and j are the subscripts of tensors

ε_{eq}^{p}: Equivalent plastic strain

$\dot{\varepsilon}_{eq}^{p}$: Equivalent plastic strain increment

ε_0: Yield strain or reference strain

ε_1, ε_2, ε_3: Principle strain

η_{pl} (or η), η_{LLD}, η'_{LLD}, γ_{LLD}: Plastic factors in J-integral calculation

λ_s: Mean center-to-center particle spacing in Roy's intercept method

v: Poisson's ratio

ς: Coefficient in the power-law form H function

σ: Stress

σ_e: von Mises stress

σ_f: Flow stress

σ_{ij}: Stress tensor, in which i and j are the subscripts of tensors

$\tilde{\sigma}_{ij}$ and $\tilde{\varepsilon}_{ij}$: Dimensionless functions of n and θ, and stress state (plane strain or plane stress) in HRR solutions

σ_{M1} and σ_{M2}: Yield strength of material 1 and 2, respectively

σ_m: Hydrostatic stress

σ_N: Mean value of nucleating stress

σ_{TS}: Ultimate tensile strength

σ_Y: Effective yield strength, an assumed value of uniaxial yield strength which presents the influence of plastic yielding upon fracture test parameters, calculated as: $\sigma_Y = 0.5(\sigma_{YS} + \sigma_{TS})$

σ_{YS}: 0.2%-offset yield strength

σ_0: Reference stress

σ_1, σ_2, σ_3: Principle strain

$\sigma_{\theta\theta}$: Nodal stress component along the crack plane (opening stress with $\theta = 0°$)

χ: Numerical constant for determining the in-plane length scale using J_{IC}

Φ: Yield surface

Abbreviations

ASTM: American Society of Testing and Materials

BSI: British Standard Institution

CCM: Computational cell methodology

CGM: Complete Gurson model

C(T): Compact tension

CTOD: Crack tip opening displacement, also denoted as δ

CMOD: Crack mouth opening displacement, also denoted as V

DCPD: Direct current potential drop method

EPFM: Elastic plastic fracture mechanics

FEA: Finite element analysis

FFS: Fitness-for-service

FPZ: Fracture process zone

GT: Gurson-Tvergaard

GTN: Gurson-Tvergaard-Needleman

HAZ: Heat affected zone

HRR: Hutchinson-Rice-Rosengren

LEFM: Linear elastic fracture mechanics

LLD: Load-line displacement

LSY: Large-scale yielding

NDT: Nil-ductility temperature test

NM: Normalization

PS: Plane-sided

SEM: Scanning electron microscopy

SE(B): Single edge notched bending

SE(T): Single edge notched tension

SG: Side-grooved

SSY: Small-scale yielding

UC: Unloading compliance

VVF: Void volume fraction

2D: Two dimensional

3D: Three dimensional

Chapter 1 Introduction

1.1 Background

Canada has been endowed with an abundance of hydrocarbon natural resources [1]. Among all transportation modes, steel transmission pipelines are one of the safest and most efficient modes for transporting hydrocarbons with a massive volume over a long distance. The development of the Canadian oil and gas pipeline system started nearly 60 years ago, and today the system contains about 112,000 kilometers of federally-regulated pipelines.

Although rare, failures of oil and gas pipelines do occur and can have severe consequences in terms of the human safety, environmental damage and economic loss [2]. Planar defects in the pipe base metal and weldments can pose a significant threat to the structural integrity of pipelines. Planar defects, in contrast to blunt or three-dimensional defects, are cracks or crack-like flaws that result from various causes such as stress corrosion cracking, fatigue, welding, and interference by excavation equipment. The fitness-for-service (FFS) assessment of pipelines containing planar defects relies heavily on the theory and application of fracture mechanics. A brief introduction of the fundamentals of fracture mechanics is provided in the following sections.

1.2 Fundamentals of fracture mechanics

1.2.1 Overview

Fracture mechanics can be divided into linear elastic fracture mechanics (LEFM) and elastic plastic fracture mechanics (EPFM) [3]. LEFM describes the fracture behavior of a material when the non-linear plastic deformation is restricted within a small region surrounding the crack tip, known as the small-scale yielding (SSY) condition. EPFM applies to the large-scale yielding (LSY) condition, which corresponds to significant plastic deformation near the crack tip. Both LEFM and EPFM are applied extensively in pipeline integrity assessment.

In terms of the direction of the loading relative to the crack, three different loading modes are classified in fracture mechanics, namely the opening (Mode I), in-plane shearing (Mode II), and out-of-plane shearing modes (Mode III) (see Fig. 1.1, in which *x*, *y* and *z* represent a Cartesian coordinate system). The deformation near the crack tip in any analysis can be treated as one or a combination of these three local displacement modes. Also, the stress field in the vicinity of the crack tip can be treated as one or a combination of these three types of stress fields. Since the opening mode is most relevant to the pipeline integrity assessment, the remainder of this thesis is focused on this loading mode.

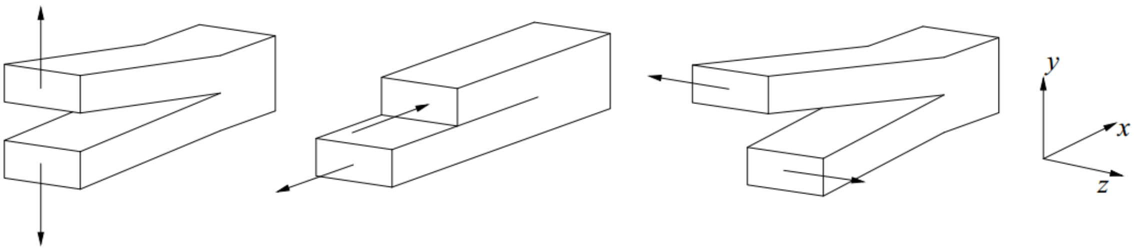

(a) Mode I: opening mode **(b) Mode II: in-plane shearing mode** **(c) Mode III: out-of-plane shearing mode**

Fig. 1.1 Three loading modes in fracture mechanics

1.2.2 Fracture mechanisms

Fracture can be categorised into brittle and ductile fracture, depending on the extent of the plastic deformation before the onset of crack initiation or propagation. Materials (e.g. ceramic) exhibiting brittle fracture behavior absorb little energy prior to fracture. Figure 1.2(a) shows the mechanism of brittle fracture: it results from the splitting apart of the atomic planes of the material, and is often accompanied by a shiny, flat fracture surface [3].

Materials failing by ductile fracture undergo significant plastic deformation in the vicinity of the planar defect before fracture failure [4]. For instance, failure associated with leakage or rupture of high-toughness pipeline steels is usually preceded by ductile fracture, where crack grows slowly and stably [5]. Figure 1.2(b) shows the mechanism of ductile fracture. As is shown, two populations of different sized impurities (i.e. large inclusions and small carbides) typically exist in the steel. The ductile fracture is proceeded by the nucleation, growth and coalescence of micro-voids, which form at the locations of the impurities. Modern pipeline steels typically have high fracture toughness and are operated at temperatures above the nil-ductility transition (NDT) temperature; therefore, most fracture problems in pipelines belong to the ductile fracture domain. This is the focus of this thesis.

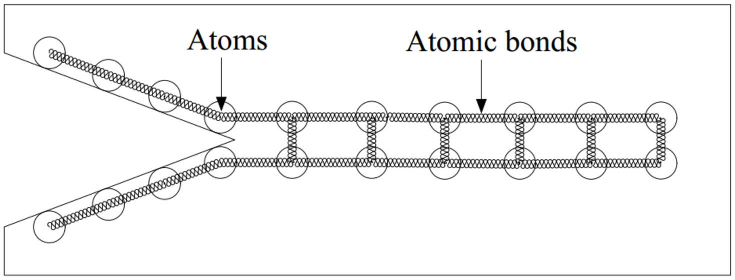

(a) Brittle fracture

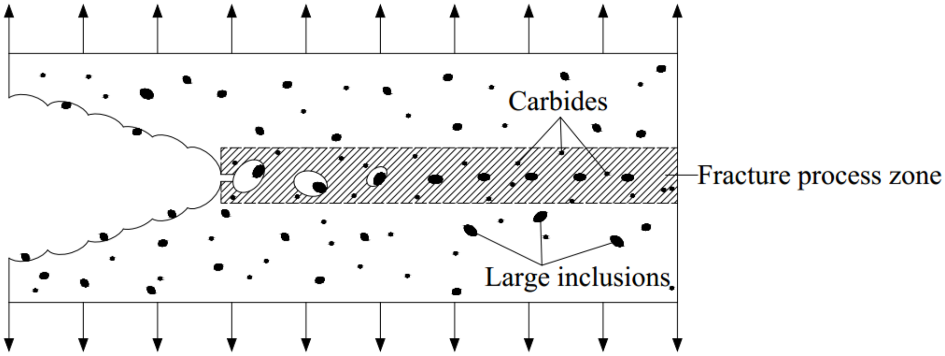

(b) Ductile fracture

Fig. 1.2 Mechanism of brittle and ductile facture

1.2.3 Linear elastic fracture mechanics

The fundamental concept of LEFM is that the stress field near the crack tip can be characterized by a single parameter- the stress intensity factor K_I (where the subscript 'I' denotes the Mode I loading). Consider an arbitrary-shaped two-dimensional (2D) body containing a crack subjected to the Mode I loading (see Fig. 1.3), where 2D means that the shape of the body does not change in the z-direction (perpendicular to the x-y plane).

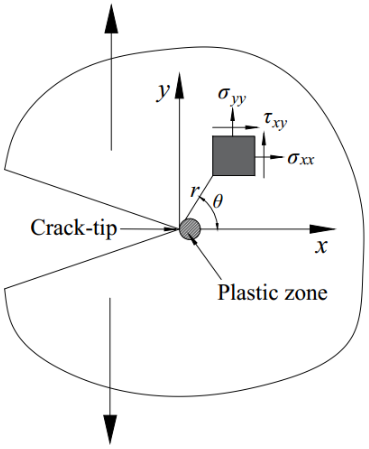

Fig. 1.3 Stress field near the crack tip

If the dimension of the body in the *z*-direction is very large compared with the dimensions in the *x*- and *y*-direction, then it is a plane strain problem. If the dimension of the body in the *z*-direction is very small compared with the dimensions in the *x*- and *y*-direction, then it is a plane stress problem. The stress field at the crack tip can be expressed as [4]:

$$\lim_{r\to 0}\sigma_{ij} = \left(\frac{K_I}{\sqrt{2\pi r}}\right) f_{ij}(\theta) \tag{1.1}$$

where

σ_{ij} is the stress tensor, in which *i* and *j* are the subscripts of tensors;

r and θ are coordinates in the polar coordinate system originated from the crack tip;

f_{ij} is a dimensionless function of θ;

K_I is the stress intensity factor in the unit of force/area×(length)$^{0.5}$.

Based on the stress field solution in Eq. (1.1), the stresses and displacements near the crack tip can be completely determined by the stress intensity factor K_I, which is a function of the external loading and geometry of the cracked body. This is the so-called single parameter characterization. The equation for calculating K_I is given as follows:

$$K_I = Y\sigma\sqrt{\pi a} \tag{1.2}$$

where

σ is the nominal stress in the uncracked section or the far-field stress;

a is the crack length;

Y is the geometry factor, which depends on the configuration and boundary condition of the cracked body. The values of Y for various configurations can be found in fracture mechanics handbooks [4].

According to Eq. (1.1), the stresses increase as r decreases. At $r = 0$, the stresses become infinite, which is the so-called $1/r^{0.5}$ singularity. The singularity is due to the sharp crack tip. For ductile fracture, however, yielding occurs when the stresses exceed the yielding limit, and a plastic zone forms ahead of the crack tip. The size of the plastic zone, r_p, can be approximately calculated as follows [6]:

$$r_p = \begin{cases} \dfrac{1}{3\pi}\left(\dfrac{K_I}{\sigma_{YS}}\right)^2 & \text{(Plane strain)} \\ \dfrac{1}{\pi}\left(\dfrac{K_I}{\sigma_{YS}}\right)^2 & \text{(Plane stress)} \end{cases} \tag{1.3}$$

where

σ_{YS} is the yield strength.

As long as the plastic zone is sufficiently small compared with the relevant local geometry such as the crack length or remaining ligament length, i.e. the SSY condition holds, Eq. (1.1) is applicable within an annulus ring, which is the so-called K-dominated zone and is defined by:

$$r_p \le r < (0.1 - 0.2)a \tag{1.4}$$

Under SSY, the energy release rate G, defined as the rate of decrease in the potential energy with a unit increase in the crack area, can be related to K_I as follows:

$$G = \frac{K_I^2}{E_{2D}} \tag{1.5}$$

where

E_{2D} is the elastic modulus in the 2D analysis and defined as:

$$E_{2D} = \begin{cases} E & \text{(Plane strain)} \\ E' = \dfrac{E}{1 - \nu^2} & \text{(Plane stress)} \end{cases} \tag{1.6}$$

where

E is Young's modulus;

v is Poisson's ratio.

The critical stress intensity factor, K_{IC}, is the value of K_I at which fracture occurs and defined as the fracture toughness. K_{IC} is a material property at a given temperature.

1.2.4 Elastic plastic fracture mechanics

For LEFM to be applicable, the SSY condition must hold. If the plastic zone becomes too large, the K-dominated zone will lose validity, and K_I is no longer suitable to characterize the crack-tip stress fields. Elastic-plastic fracture mechanics (EPFM) is introduced to overcome this limitation. In EPFM, the J-integral proposed by Rice [7] and the crack tip opening displacement (CTOD) proposed by Wells [8] are the two most important concepts.

i) J-integral:

Figure 1.4 shows the uniaxial stress-strain relationship for elastic plastic and nonlinear elastic materials. The difference between them is the unloading paths. If the stress in each material increases monotonically and no unloading occurs, there is no difference between these two stress-strain relationships. It follows the deformation theory of plasticity, which relates the total stress to total strain, and is equivalent to the nonlinear elastic theory under the monotonic loading condition.

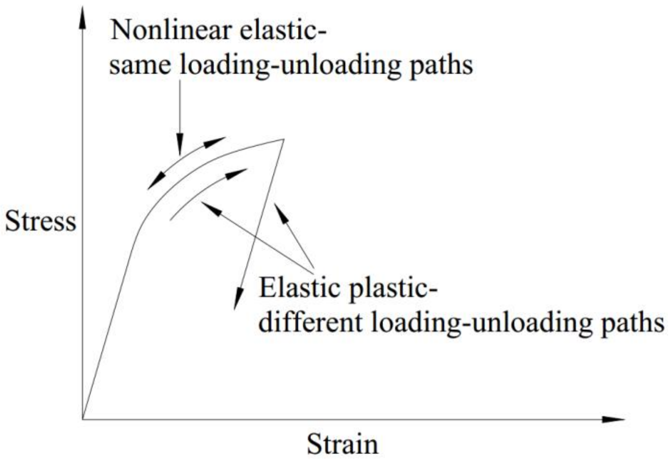
Nonlinear elastic-
same loading-unloading paths
Stress
Elastic plastic-
different loading-unloading paths
Strain

Fig. 1.4 Elastic plastic and nonlinear elastic stress-strain relationships

By applying the small-strain deformation theory of plasticity (i.e. small-strain nonlinear elastic theory) and considering a cracked homogeneous 2D body of linear or nonlinear elastic material subjected to a monotonic loading as shown in Fig. 1.5, the *J*-integral is defined as:

$$J = \int_{\Gamma} \left(w dy - T_i \frac{\partial u_i}{\partial x} ds \right) \tag{1.7}$$

$$w = w(x, y) = w(\varepsilon_{ij}) = \int_0^{\varepsilon_{ij}} \sigma_{ij} d\varepsilon_{ij} \tag{1.8}$$

$$T_i = \sigma_{ij} n_j \tag{1.9}$$

where

Γ is an arbitrary counter-clockwise path surrounding the crack tip;

u_i is the components of the displacement vector;

T_i is the component of the traction vector on the contour Γ;

w is the strain energy density per unit volume;

ds is the infinitesimal arc length along the contour Γ;

ε_{ij} (i, j = 1, 2, or 3) is the strain tensor;

n_j is the component of the unit normal vector to Γ.

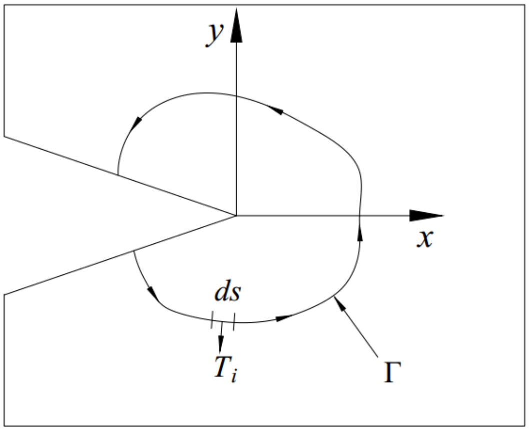

Fig. 1.5 Schematic of *J*-integral

Rice [7] showed that the value of *J*-integral is independent of the integration path Γ around the crack tip. It was further shown that *J* is also equivalent to the energy release rate for the nonlinear elastic cracked body, and reduces to *G* for a linear elastic crack body. Similar to the stress intensity factor, *J*-integral is also an intensity parameter characterizing the stress fields near the crack tip.

Consider a 2D (i.e. plane strain or plane stress) cracked body characterized by the deformation theory of plasticity and a Ramberg-Osgood stress-strain relationship as follow:

$$\frac{\varepsilon}{\varepsilon_0} = \frac{\sigma}{\sigma_0} + \alpha_{R-O}\left(\frac{\sigma}{\sigma_0}\right)^{n_{R-O}} \tag{1.10}$$

where

σ_0 is the reference stress and typically set equal to the yield strength;

$\varepsilon_0 = \sigma_0/E$ is the corresponding reference strain;

$\alpha_{R\text{-}O}$ and $n_{R\text{-}O}$ are parameters of the Ramberg-Osgood stress-strain relationship and $n_{R\text{-}O}$ is commonly known as the strain-hardening exponent.

Hutchinson [9] as well as Rice and Rosengren [10] independently showed that the stress and strain fields near the crack tip can be calculated by J at distances where the elastic strain is negligible compared to the plastic strain as follows:

$$\left(\sigma_{ij}\right)_{HRR} = \sigma_0 \left(\frac{EJ}{\alpha_{R-O}\sigma_0^2 I_n r}\right)^{\frac{1}{n_{R-O}+1}} \tilde{\sigma}_{ij}(n,\theta) \qquad (1.11)$$

$$\left(\varepsilon_{ij}\right)_{HRR} = \frac{\alpha\sigma_0}{E} \left(\frac{EJ}{\alpha_{R-O}\sigma_0^2 I_n r}\right)^{\frac{1}{n_{R-O}+1}} \tilde{\varepsilon}_{ij}(n,\theta) \qquad (1.12)$$

where

I_n is an integration constant that depends only on $n_{R\text{-}O}$;

$\tilde{\sigma}_{ij}$ and $\tilde{\varepsilon}_{ij}$ are the dimensionless functions of $n_{R\text{-}O}$ and θ, and stress state (plane strain or plane stress).

Equations (1.11) and (1.12) are the so-called HRR solutions (singularity). Note that the HRR solutions are only valid at locations where the elastic strain is negligible compared with the plastic strain and where the small strain assumption is still valid. Such locations are represented by an annulus ring, known as the J-dominated zone, surrounding the crack tip. Figure 1.6 shows the K- and J- dominated zones under SSY condition.

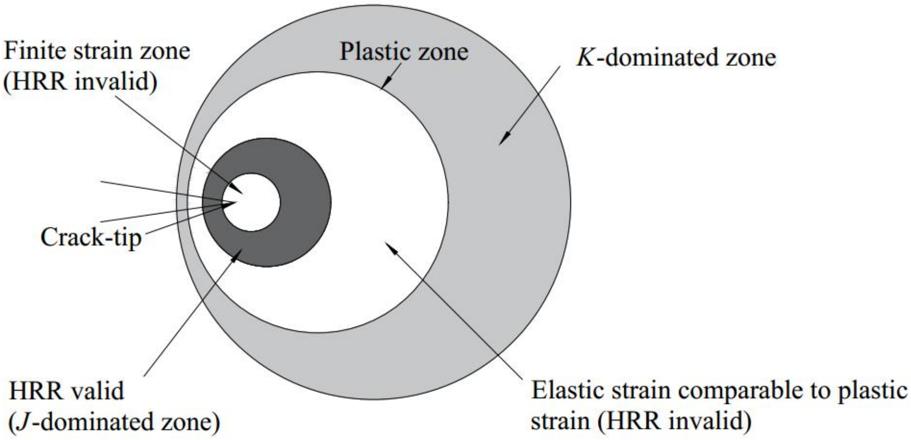
Finite strain zone
(HRR invalid)
Plastic zone
K-dominated zone
Crack-tip
HRR valid
(J-dominated zone)
Elastic strain comparable to plastic
strain (HRR invalid)

Fig. 1.6 Effect of plasticity on the crack-tip stress fields under SSY

It should be also noted that the HRR field becomes invalid under the LSY condition, when the finite strain zone becomes as large as the plastic zone. However, under this condition, the *J*-integral can still be calculated, though it does not uniquely characterize the crack-tip stress and strain fields. In this case, the *J*-integral is a characterizing parameter that quantifies the severity of the crack-tip fields. For ductile material, analogous to K_I and K_{IC}, when the crack driving force *J* reaches the critical toughness value J_{IC}, the stable crack growth initiates.

ii) CTOD:

In EPFM, a parameter alternative to the *J*-integral for characterizing the stress field near the crack tip is the crack tip opening displacement (CTOD), also often denoted as δ. Stable fracture occurs when CTOD reaches a critical value δ_{IC}. Two most commonly used definitions for CTOD are the displacement at the original crack tip and the 45-degree intercept from the current (blunted) crack tip (see Figs. 1.7(a) and (b), respectively). It is found that for materials with high toughness, the initial sharp crack tip is blunted before subsequent ductile tearing. If a semicircle (blunted) crack tip is assumed, these two definitions are essentially equivalent.

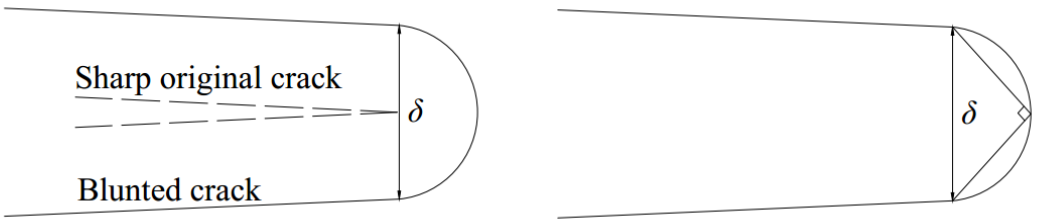

(a) Displacement at the original crack tip (b) Intersection of a 90-degree vertex

Fig. 1.7 Schematic of CTOD definitions

CTOD can be related to K_I in LEFM and J in EPFM as follows:

$$\delta = \begin{cases} \dfrac{(1-\nu^2)K_I^2}{2E\sigma_0} & \text{(Plane strain, LEFM)} \\ \dfrac{K_I^2}{E\sigma_0} & \text{(Plane stress, LEFM)} \\ \dfrac{J}{m\sigma_0} & \text{(EPFM)} \end{cases} \tag{1.13}$$

where

m is a dimensionless constraint parameter that is approximately 1 for plane stress condition and 2 for plane strain condition [11]. In the EPFM, typical range for m values is between 1.5 and 2 and m is strongly dependent on the strain hardening exponent.

1.2.5 Fracture toughness resistance curve

The relationship between the fracture toughness and crack extension (denoted by ‘Δa’) under stable crack growth is defined as the fracture toughness resistance curve (the so-called *R*-curve). Materials with high toughness typically do not fail suddenly at a particular *J* or CTOD. The fracture toughness increases with the crack growth. The fracture toughness resistance curve is a key input to the FFS assessment of modern high-toughness steel pipelines. Figure 1.8 shows a typical *J*-*R* curve for a ductile material. At initial stages of the deformation, the *J*-*R* curve rises rapidly due to the small amount of crack blunting. Once J_I reaches J_{IC}, crack growth initiates. Afterwards, the crack grows stably with the increase of the load. The load-carrying capacity of the structure increases with the rise of the *J-R* curve.

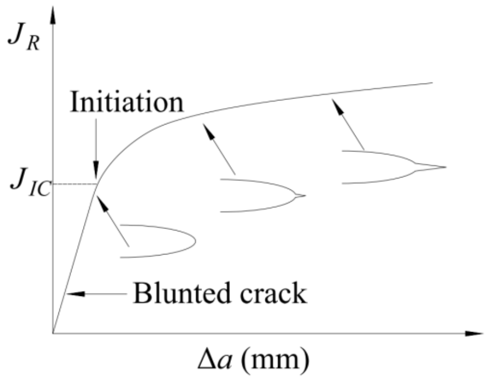

Fig. 1.8 Schematic *J-R* curve for a ductile material

In practice, the *R*-curve tests are conducted using small-scale laboratory specimens, such as single edge notched bending (SE(B)), compact tension (C(T)), single edge notched tension (SE(T)) specimens. In order to experimentally evaluate the *R*-curve for these specimens, the load versus load line displacement (*P*-LLD) curve or the load versus crack mouth opening displacement (*P*-CMOD) curve is needed. Figures 1.9(a) to (c) illustrate the plane-sided SE(B), C(T), and SE(T) specimens as well as LLD and CMOD (also denoted as '*V*'). Note that B, B_N, S, W, H and a denote the specimen thickness, net thickness, span, width, daylight distance between grips and crack length, respectively. Side-grooving is a common practice in fracture toughness tests to promote a straight crack front during the stable crack growth [12] (see Fig. 1.9(d)).

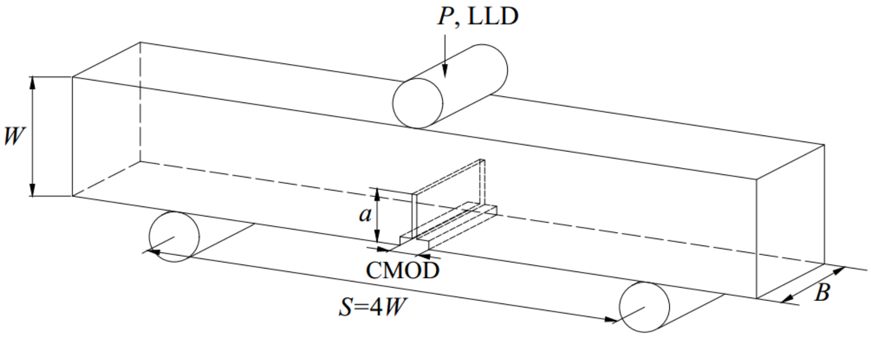

(a) Plain-sided SE(B) specimen

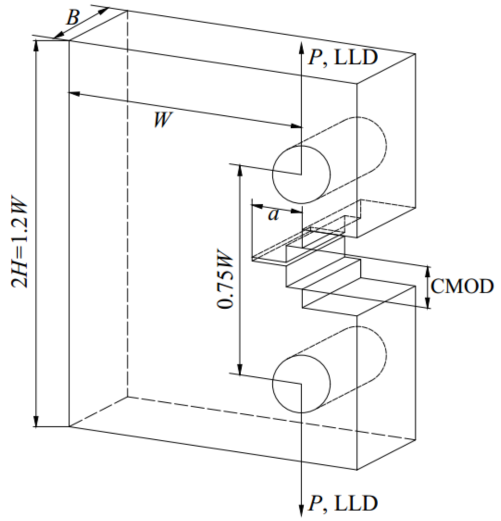
B
P, LLD
W
2H=1.2W
a
0.75W
CMOD
P, LLD

(b) Plain-sided C(T) specimen

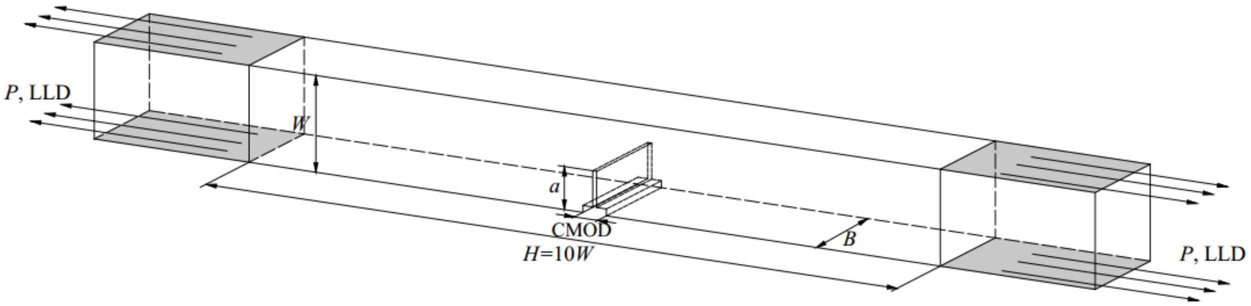
P, LLD
W
a
CMOD
H=10W
B
P, LLD

(c) Plain-sided clamped SE(T) specimen

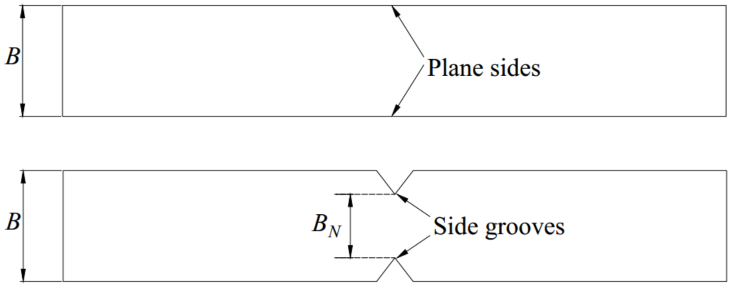
B
Plane sides
B
B_N
Side grooves

(d) Schematic of side grooves

Fig. 1.9 Schematic of small-scale specimens

1.2.6 Resistance curve test methods

The single-specimen technique is commonly used to experimentally determine the resistance curve from a single small-scale lab specimen, e.g. SE(B) or C(T) specimen [12]. The single-specimen technique can be further classified into three different methods. The first one is the elastic unloading compliance (UC) method, which has been adopted as a standard practice and widely used to measure the resistance curve. The second one is the direct current potential drop (DCPD) method. However, for both methods, either repeated loading-unloading procedures or complicated testing equipment are involved in the test. The third one is the normalization (NM) method, which reduces the complexity involved in the measurements during the test and is suitable to generate resistance curves under high temperatures, high loading rates or aggressive testing environments when it is not possible to measure crack extension directly. The application of the NM method to the SE(T) specimen is studied in this thesis.

1.2.7 Constraint effects

The crack tip constraint is defined as a measure of the resistance to plastic deformation [13] (see Fig. 1.10). The specimen geometric configuration (i.e. crack depth ratio a/W, thickness to width ratio B/W and specimen width W) and loading configuration (i.e. bending vs. tension), as well as material mismatch (i.e. strength mismatch and work hardening mismatch) can significantly affect the R-curve due to the so-called ‘constraint effect’. Conventional fracture toughness testing specimens, such as deeply-cracked SE(B) and C(T) specimen under predominantly bending deformation are designed to guarantee high levels of crack-tip constraint and therefore lead to low toughness values.

Given that planar defects on oil and gas pipelines are typically shallow and subjected to low constraint levels, the use of the SE(T) specimen to determine R-curve has gained much attention since the crack-tip stress and strain fields of SE(T) specimen are more relevant to those of the full-scale pipe containing surface cracks under internal pressure and longitudinal tension [14]. Therefore, conducting fracture toughness testing on SE(T) specimens can result in a more accurate assessment for the pipeline structure in terms of ductile crack initiation and growth compared to SE(B) or C(T) specimens. British Standard Institution (BSI) [15] have standardized the use of the clamped SE(T) specimen to conduct fracture resistance testing.

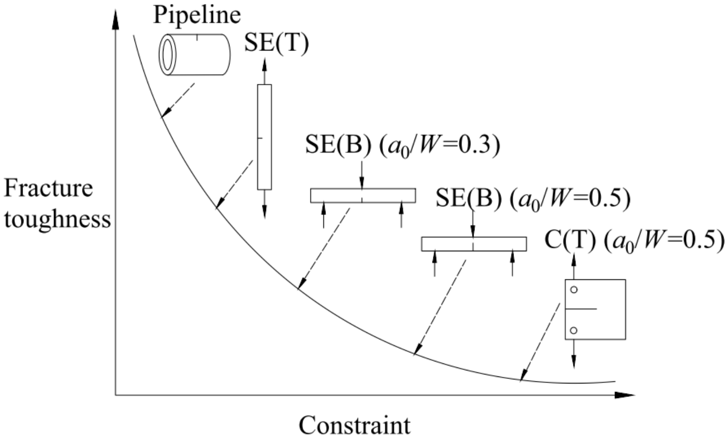

Fig. 1.10 A schematic illustration of constraint effect on fracture toughness

1.3 Research objectives and significance

The goals of the research reported in this thesis include numerically simulating ductile crack growth for clamped SE(T) specimens based on the Gurson-Tvergaard-Needleman (GTN) constitutive model, validating the NM method for SE(T) specimens with various geometric configurations in terms of developing *J*-*R* curves, and improving the conventional NM method based on the *J*-CMOD relation. The research outcome will facilitate the evaluation of *J*-*R* curves using an improved *k* factor-based NM method. The specific objectives of the study include:

1). Present a comprehensive review on the mechanism and modelling approaches to ductile fracture, particularly on the GTN constitutive relation.

2). Calibrate the micromechanical parameters for X80-grade pipeline steel using experimental results from SE(B) and SE(T) specimens based on FEA.

3). Investigate the ability of using the computational cell methodology incorporating the GTN model to simulate ductile crack growth.

4). Describe and compare the stress field and constraint effects for SE(T) specimens based on FEA involving stationary and growing cracks.

5). Validate the applicability of NM method to SE(T) specimens with various geometric configurations (i.e. a_0/W, B/W, plane-sided (PS)/side-grooved (SG)).

6). Propose the so-called k factor-based NM method based on the inherent J-CMOD relation of each fracture specimen to simplify the conventional NM method.

1.4 Thesis format and outline

This thesis has a monograph format and organizes chapters around a central topic: ‘Investigation of ductile crack growth and normalization method for SE(T) specimen using finite element analyses’, under the regulations by Graduate and Postdoctoral Studies at University of Western Ontario.

This thesis is structured as follows:

Chapter 1: Introduce the entire thesis where a brief review of fundamentals of fracture mechanics is presented.

Chapter 2: Summarise a comprehensive review of mechanism of ductile crack growth. Different approaches of modelling ductile crack growth are also presented.

Chapter 3: Describe the calibration process of micromechanical parameters and numerically simulate the FE models for standard SE(T) specimens with various geometric configurations. The stress fields and constraint parameters of the GTN models are examined, and compared with the stationary-crack FEA.

Chapter 4: Validate the applicability of NM method for SE(T) specimens. In addition, the so-called k factor-based NM method is proposed to simplify and improve the conventional NM method.

Chapter 5: Summary, conclusions and recommendations for future research.

Chapter 2 Literature Review: Mechanism and modelling of ductile fracture

2.1 Approaches to analyze ductile fracture

2.1.1 Global approach

One of the engineering approaches for crack-like defect assessment of energy pipelines is based on the fracture toughness input (i.e. J-integral fracture parameter by Rice [7]). This elastic-plastic (non-linear) fracture mechanics approach is categorized as 'global approach [16]' (also termed as 'global failure criterion'). The global approach applies the crack growth resistance curves (i.e. J-R curve) tested from small laboratory specimens to the actual surface defects in pipelines and has been extensively studied in the past. However, it has been shown that the fracture toughness is dependent on the specimen geometry, specimen size, crack depth and loading mode. This is known as the 'constraint effect'.

The reason for the 'constraint effect' lies in that, the stress state near the crack-tip region deviates from the HRR singularity solutions [4] as plastic deformation increases. This led to the development of two-parameter approaches (e.g. K-T approach [17], J-Q approach [18, 19], J-A_2 approach [20, 21], J-h approach [22], J-T_Z approach [23-25]). Note that the J-integral also has the limitation to be applied to weld joints or heat affected zones (HAZ) due to the complex geometry, residual stress, and plastic mismatching of material in those regions. This limitation led to the proposal of three-parameter approaches (i.e. J-Q-M approach [26], J-T_g-T_m approach [27]). Moreover, the J-integral method can only deal with pre-existing cracks and is not able to model crack initiation or extension [16]. The above-mentioned limitations associated with the global approach prompted the development of a more physical-based approach, i.e. the local approach, to describe ductile fracture.

2.1.2 Local approach

The local approach [28] takes into account the physical microstructural process during ductile fracture. This approach has been developed extensively during the past four decades.

It has the advantages of being able to simulate fracture tests that are difficult to carry out, and most importantly, capturing the failure initiation and subsequent crack growth [29].

Various local approach-based models can be classified into uncoupled and coupled models [30]. The uncoupled model assumes that the local effect (i.e. damage due to micro-voids nucleation, growth and coalescence in material matrix) is not significant and does not take into account the effect of void growth on material behavior (i.e. softening). The onset of coalescence is post-processed using node release technique based on certain critical fracture criterion (e.g. critical void growth ratio $(R/R_0)_C$ in [31], critical cohesive energy $(\Gamma_0)_C$ in [32, 33] and critical void damage variable $(V_D)_C$ in [34, 35]). Typical uncoupled models include the void growth models proposed by Rice et al. [31], McClintock et al. [36], Thomason [37], Tai et al. [34, 35], and cohesive zone models developed by Scheider et al. [32] and Cornec et al. [33].

The coupled model, on the other hand, considers a non-negligible micromechanical effect during fracture initiation and damage process. The void volume fraction is incorporated into the constitutive model in the local approach, and the crack extension is automatically captured by element extinction at the crack tip. Two typical coupled models are the Rousselier [38] and Gurson models [39, 40]. The Rousselier model simulates the micro-void evolution by introducing a state variable into the constitutive relationships, while the Gurson model proposes a yield potential based on cell studies with a concentric spherical void.

The categorization of approaches to analyze ductile fracture is schematically shown in Fig. 2.1. Note that the GTN model, complete Gurson model (CGM) and traction-separation model are three improved versions of the original Gurson model. In this thesis, the GTN model is used to describe the progressive void growth and subsequent macroscopic material softening within computational cells. The Gurson constitutive model for dilatant plasticity and the computational cell methodology will be described in Sections 2.3 and 2.4, respectively.

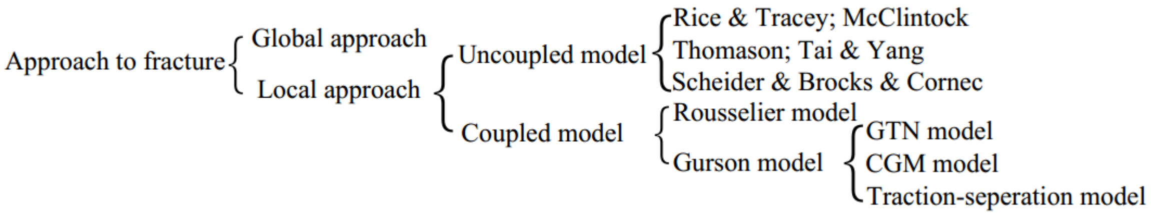
Approach to fracture
Global approach
Local approach
Uncoupled model
Rice & Tracey; McClintock
Thomason; Tai & Yang
Scheider & Brocks & Cornec
Coupled model
Rousselier model
Gurson model
GTN model
CGM model
Traction-seperation model

Fig. 2.1 Engineering approaches and models for ductile fracture

2.2 Physical damage mechanism of ductile material

Date back to late 1940's evolved the early understanding of the physical damage mechanism of ductile materials on microstructural level. In 1948, Tipper [41] suggested that micro-void initiation occurs by fracture of non-metallic inclusions and by de-cohesion of the inclusion-matrix interface, which was subsequently verified by Puttick [42] and Rogers [43] in their tensile bar experiments. Gurland et al. [44] suggested that ductile fracture is proceeded by voids formation at inclusions, growth and internal striction. Goods et al. [45] later found that the nucleation strain increases with particle size, particle volume fraction, particle shape and temperature effect. It was also suggested that the nucleation strain can be predicted quantitatively if a critical stress is assumed when the interface breaks. Hahn et al. [46] studied the effect of grain size and fracture toughness of alloy sheets, and concluded that the linking-up of voids is accomplished by the rupture of the intervening ligaments.

All the above-mentioned studies showed the evidence that voids/pores exist in all metallic materials, at any stages of fracture. For very pure single crystal materials (such as quartz and gemstones), micro-void formation is observed at dislocation cell walls [47]. For most practical materials, two idealized populations of different sized inclusions exist and micro-voids nucleate at these locations, including large inclusions (e.g. MnS and Al_2O_3) and small inclusions (e.g. iron carbides) (see Fig. 1.2(b)). A large number of experimental results have shown that the macroscopic ductile fracture process is related to the nucleation, growth and coalescence of micro-voids [36, 48]. This process is briefly described as follows:

The existence of inclusions weakens the bonding strength with surrounding matrix material and thus, make de-bonding much easier due to the non-synchronized increase of stress and transformation. In this way, nucleation starts from fracture of the inclusions and/or de-cohesion (also termed as ‘de-bonding’) within the steel matrix (see Figs. 2.2(a) and 2.2(b)), and subsequently, forms micro-voids. Note that micro-voids may also pre-exist in materials. As the applied stress and strain level increases, these micro-voids consistently grow larger (see Fig. 2.2(c)). At the final stage, micro-voids coalesce due to internal necking (large primary voids coalesce at high stress triaxiality), or micro-void sheeting (coalescence of secondary voids along inter-void ligaments while primary voids remain small at low stress triaxiality) (see Figs. 2.2(d) and 2.2(e), respectively), and result in ductile fracture in the fracture process zone (FPZ).

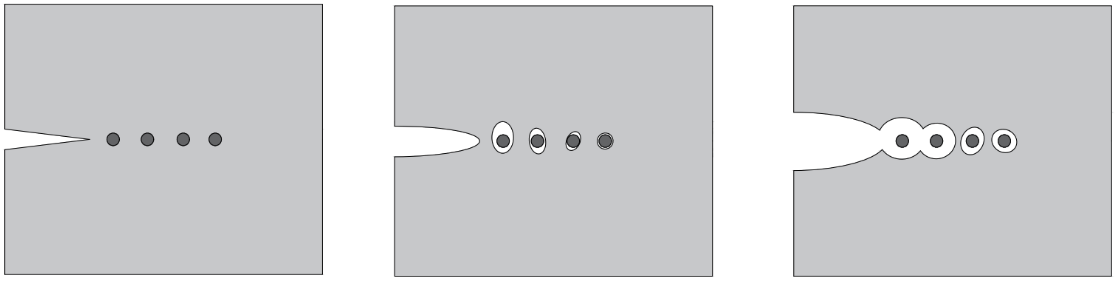

(a) Initial state **(b) Void nucleation** **(c)Void growth**

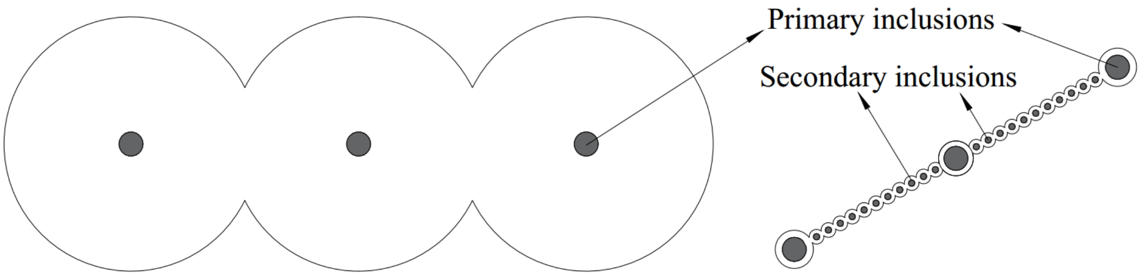

(d) Internal necking **(e) Void sheeting**

Fig. 2.2 Schematic of the micro-mechanisms of ductile fracture

2.3 GTN model for dilatant plasticity

2.3.1 Yield condition and flow rule

Based on a rigid plastic material behavior and upper bound solution for spherically symmetric deformations of a single spherical void, Gurson [39, 40] in 1979 proposed the following yield condition for material with a single spherical void:

$$\Phi\left(\sigma_e, \sigma_m, \sigma_f, f\right) = \left(\frac{\sigma_e}{\sigma_f}\right)^2 + 2f\cosh\left(\frac{3\sigma_m}{2\sigma_f}\right) - 1 - f^2 = 0 \tag{2.1}$$

$$\sigma_e = \sqrt{\frac{1}{2}[(\sigma_{11} - \sigma_{22})^2 + (\sigma_{22} - \sigma_{33})^2 + (\sigma_{33} - \sigma_{11})^2 + 6(\sigma_{12}^2 + \sigma_{23}^2 + \sigma_{31}^2)^2]} \tag{2.2}$$

$$\sigma_m = \frac{1}{3}(\sigma_{11} + \sigma_{22} + \sigma_{33}) \tag{2.3}$$

where

$\sigma_{11}, \sigma_{22}, \sigma_{33}, \sigma_{12}, \sigma_{23}, \sigma_{31}$ are the stress components of stress tensor σ_{ij}, in which i, j = 1, 2, 3;

σ_e is the effective von Mises stress;

σ_m is the mean stress (i.e. ‘hydrostatic stress’);

σ_f is the flow stress of the matrix material as a function of the equivalent plastic strain;

f is the current void volume fraction (VVF) in the material, and is defined as V_{void}/V_{matrix}, in which V_{void} is the void volume and V_{matrix} is the volume of the matrix material cell. In Eq. (2.1), if $f = 0$, the material is fully dense, and the Gurson yield condition reduces to the classic von Mises yield condition. If $f = 1$, the material is completely voided and has no stress-carrying capacity.

The most significant difference between the Gurson model and other conventional plastic models (i.e. the von Mises plasticity theory) lies in that the hydrostatic stress and void volume fraction are included in the Gurson yield condition. However, note that the material in the Gurson model is idealized to be simply rigid-plastic and the yield function is the approximate solution resulting from the upper bound theorem of plasticity.

In 1981, the Gurson model was modified by Tvergaard [49] (the so-called ‘GT model’) by taking into account the void interaction effects for periodic arrays of cylindrical and spherical voids. Three q-parameters were introduced into the Gurson model:

$$\Phi\left(\sigma_e, \sigma_m, \sigma_f, f\right) = \left(\frac{\sigma_e}{\sigma_f}\right)^2 + 2q_1 f \cosh\left(\frac{3q_2\sigma_m}{2\sigma_f}\right) - 1 - q_3 f^2 = 0 \tag{2.4}$$

where

the q-parameters are coefficients related to the void volume fraction and pressure terms. $q_1 = 1.5$, $q_2 = 1.5$ and $q_3 = q_1^2$ were proposed to match the numerical studies of ‘ordered’ voided materials in plane strain tensile fields well with experimental results [49]. Note that the original Gurson model can be recovered by setting $q_1 = q_2 = q_3 = 1$.

Figure 2.3 shows the yield surfaces for different levels of porosity in the σ_e/σ_f-$|\sigma_m|/\sigma_f$ plane of the GT model. Note that when $f = q_3^{-0.5}$, the yield surface shrinks into a point and the stress-carrying capacity of the material vanishes. The straight line shows the case when $f = 0$, and the yield surface turns into that for a von Mises solid, i.e. yielding is independent of the hydrostatic stress.

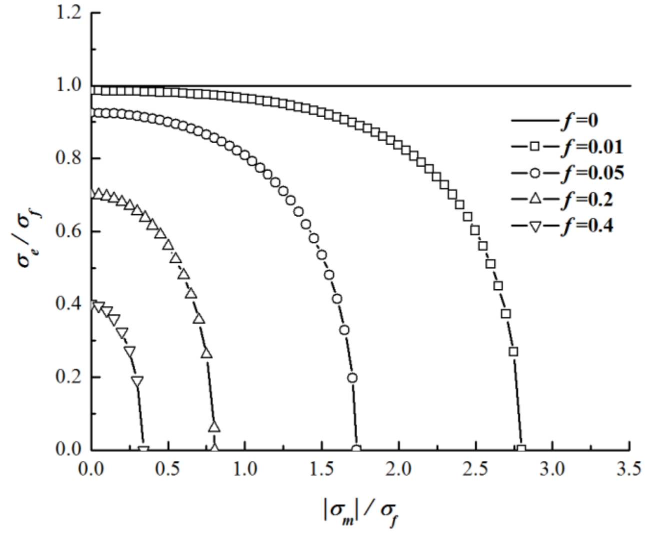

Fig. 2.3 Yield surface dependence on the hydrostatic tension and porosity

The Gurson model itself cannot predict the void coalescence or capture the sudden loss of load-carrying capacity at the onset of micro-void coalescence [50]. Tvergaard and Needleman [51] took into account the void growth rate acceleration when a critical void volume fraction f_C is exceeded and proposed the 'Gurson-Tvergaard-Needleman model' (termed as 'GTN model' henceforth in this thesis). The corresponding yield condition and modified void volume fraction are given by:

$$\Phi\left(\sigma_e, \sigma_m, \sigma_f, f^*\right) = \left(\frac{\sigma_e}{\sigma_f}\right)^2 + 2q_1 f^* \cosh\left(\frac{3q_2\sigma_m}{2\sigma_f}\right) - 1 - q_3 f^{*2} = 0 \tag{2.5}$$

in which

$$f^* = \begin{cases} f & (f \leq f_C) \\ f_C + \delta_a(f - f_C) & (f_C < f < f_F) \\ f_u^* & (f \geq f_C) \end{cases} \tag{2.6}$$

$$\delta_a = \frac{f_u^* - f_C}{f_F - f_C} \tag{2.7}$$

$$f_u^* = \frac{q_1 + \sqrt{q_1^2 - q_3}}{q_3} = \frac{1}{q_1} \tag{2.8}$$

where

f^* is the modified void volume fraction;

f_u^* is the ultimate value of the damage parameter f^* and has no physical meaning. Note that the product $f_u^* q_1$ is not necessarily 1 in practical applications to keep numerical stability [52];

δ_a is the accelerating factor.

The flow rule in the GTN model is derived from the plastic potential, which is the same as the yield condition Φ according to the associated flow rule [3]. The evolution of the equivalent plastic strain, which controls matrix hardening is described by setting the plastic work rate equal to the matrix plastic work rate.

2.3.2 Void nucleation

The change of void volume fraction is partly due to the growth of existing voids and to a less extent, due to the nucleation of new voids:

$$\dot{f} = \dot{f}_{nucl} + \dot{f}_{gr} \tag{2.9}$$

where

$\dot{f}_{nucl}$ represents the change of void volume fraction due to the nucleation of new voids;

$\dot{f}_{gr}$ represents the change of void volume fraction due to the growth of existing voids.

The nucleation of larger inclusions commonly occurs at a relatively low stress state at the beginning stage of the plastic deformation [26], well below the peak stress state that develops in front of the crack tip [53, 54]. Therefore, it is a common practice to assign an initial void volume fraction f_0 to replace large particles without significantly impacting the prediction of material toughness.

As for the evolution of f due to the nucleation of secondary small voids, it is a common practice to relate it to an increment of strain and an increment of stress [52], described by [55]:

$$\dot{f}_{nucl} = A_{N1}\dot{\varepsilon}_{eq}^{p} + A_{N2}(\dot{\sigma}_f + \dot{\sigma}_m) \tag{2.10}$$

where

A_{N1} and A_{N2} are the nucleation intensities due to equivalent plastic strain increment and stress increment, respectively, both of which are dependent on deformation and hydrostatic stress history [56];

$\dot{\varepsilon}_{eq}^{p}$ represents the equivalent plastic strain increment;

$\dot{\sigma}_f$ represents the flow stress increment;

$\dot{\sigma}_m$ represents the hydrostatic stress increment.

Three nucleation criteria can be further categorized based on Eq. (2.10):

i) Plastic strain-controlled nucleation criterion:

$$A_{N1} = \frac{f_{N\varepsilon}}{s_N\sqrt{2\pi}} \exp\left[-\frac{1}{2}\left(\frac{\varepsilon_{eq}^p - \varepsilon_N}{s_N}\right)^2\right] \tag{2.11}$$

while

$A_{N2} = 0$ in Eq. (2.10);

$f_{N\varepsilon}$ is the void volume fraction of nucleated voids. It is determined so that the total void volume nucleated is consistent with the volume fraction of particles.

Plastic strain-controlled nucleation criterion makes an idealization that there is a mean equivalent plastic strain for nucleation (i.e. ε_N, also termed as mean void nucleation strain), and the nucleation process follows a normal distribution about ε_N. s_N is the corresponding standard deviation of the normal distribution.

ii) Stress-controlled nucleation criterion:

$$A_{N2} = \frac{f_{N\sigma}}{s_N\sigma_{YS}\sqrt{2\pi}} \exp\left[-\frac{1}{2}\left(\frac{\sigma_f + \sigma_m - \sigma_N}{s_N\sigma_{YS}}\right)^2\right] \tag{2.12}$$

while

$A_{N1} = 0$ in Eq. (2.10);

$f_{N\sigma}$ is the void volume fraction of nucleated voids. It is determined so that the total void volume nucleated is consistent with the volume fraction of particles;

σ_{YS} is the 0.2%-offset yield strength of the material.

Stress-controlled nucleation criterion assumes that the nucleation criterion only depends on the maximum stress transmitted across the particle-matrix interface. The nucleation stress distributes in a normal fashion about σ_N.

iii) Mixed nucleation criterion:

$A_{N1} \neq 0$ and $A_{N2} \neq 0$ in the mixed nucleation criterion. The nucleation is controlled by a combination of the strain- and stress-controlled nucleation criteria, i.e. $A_{N1} \neq 0$ and $A_{N2} \neq 0$ in Eq. (2.10). In practice, inclusions and particles with different sizes and shapes exist non-uniformly in the material and the actual nucleation process is dependent on the intrinsic properties of the material. The stress is small at the beginning stage of nucleation and micro-voids nucleate at larger inclusions, following the stress-controlled nucleation criterion. At the intermediate or final stage of nucleation, micro-voids nucleate at the particles with smaller sizes, following the plastic strain-controlled criterion. Thus, the mixed nucleation criterion is more representative of general cases.

2.3.3 Void growth

In practical modeling of the void growth, the increase in f is treated as one entire large void growth as illustrated in Fig. 2.4. At the i th loading increment (see Fig. 2.4(a)), the void volume fraction is f_0. At the next (i+1) th loading increment, the void volume fraction is $f_0 + f_{gr} + f_{nucl}$ (see Fig. 2.4(b)) and is equivalent to a homogenized f (see Fig. 2.4(c)).

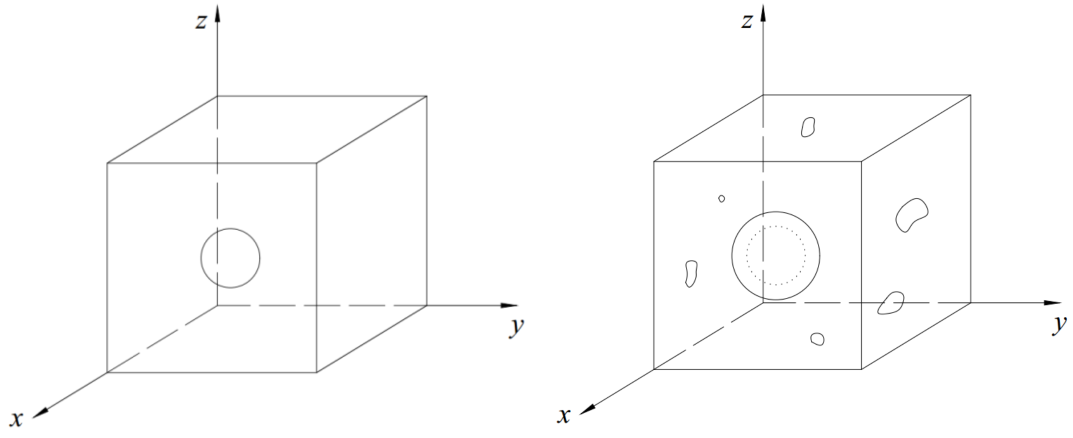

(a) *i* th loading increment **(b) (*i*+1) th loading increment**

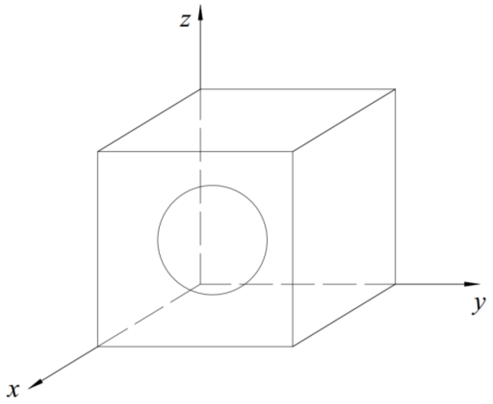

(c) Equivalent (*i*+1) th loading increment

Fig. 2.4 Homogenization treatment of void growth

The evolution of *f* due to the void growth is described by the law of conservation of mass and plastic incompressibility of the matrix material, expressed as:

$$\dot{f}_{gr} = (1 - f)\left(\dot{\varepsilon}_{11}^{pl} + \dot{\varepsilon}_{22}^{pl} + \dot{\varepsilon}_{33}^{pl}\right) \tag{2.13}$$

where

$\dot{\varepsilon}_{11}^{pl} + \dot{\varepsilon}_{22}^{pl} + \dot{\varepsilon}_{33}^{pl}$ is the rate of the change of plastic hydrostatic strain;

$\dot{\varepsilon}_{11}^{pl}$, $\dot{\varepsilon}_{22}^{pl}$, $\dot{\varepsilon}_{33}^{pl}$ are the rate of the change of three components of plastic strain tensors.

2.3.4 Void coalescence

As the plastic strain increases with loading, a second population of much smaller inclusions, such as iron carbides assist the final stage of coalescence through localization of plastic flow between the voids. Note that they do not nucleate until large plastic strains present and therefore do not strongly affect the peak stress capacity of the material. The void coalescence is a relatively rapid process with large void volume fraction increases at the end of the localization of plastic flow between micro-voids. The original Gurson model does not intrinsically include a coalescence criterion to model the joining between micro-voids after extensive damage. Currently there are three coalescence criteria: the critical void volume fraction, Thomason's plastic limit load, and traction-separation model criteria. They are briefly described in the following:

The critical void volume fraction criterion was proposed by Tvergaard and Needleman [51] (see Eqs. (2.6), (2.7) and (2.8)). It considers the acceleration of void volume growth rate and rapid load-carrying capacity drop once a critical value f_C is reached (see Fig. 2.5(a)). At this point, coalescence occurs. When f reaches the void volume fraction at failure f_F (also denoted as f_E, see Fig. 2.5(b)), the failure at the material point occurs. Figure 2.6 depicts the relation between f^* and f. In ABAQUS, f_C and f_F are user-defined parameters.

Figures. 2.7(a) and 2.7(b) respectively show the comparison results of void volume fraction (VVF) increase verses crack mouth opening displacement (CMOD) and the load-carrying capacity verses CMOD for two materials with different f_C values conducted in a 2D plain strain FEA of SE(B) specimen with a_0/W = 0.5 using ABAQUS. The details about FEA will be introduced in Chapter 3. Here, Material #1 has a property of: f_0 = 0.0001, f_C = 0.02 and f_F = 0.1, while Material #2 has a property of: f_0 = 0.0001, f_C = f_F = 0.1. As can be observed, the critical value f_C marks the onset of a significant drop of the load-carrying capacity.

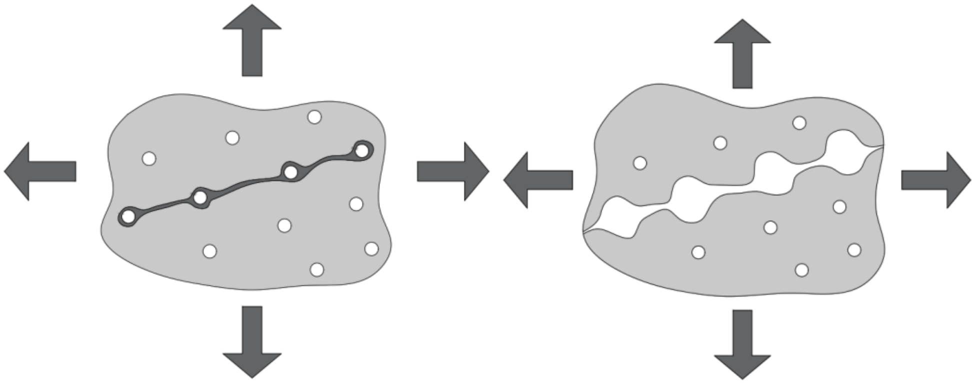

(a) $f = f_C$ **(b) $f = f_F$**

Fig. 2.5 Schematic illustration of void coalescence

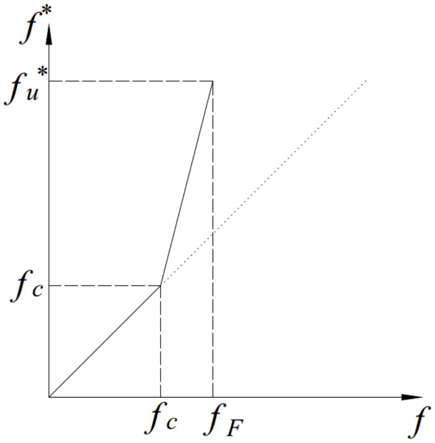

Fig. 2.6 Relation between f^* and f

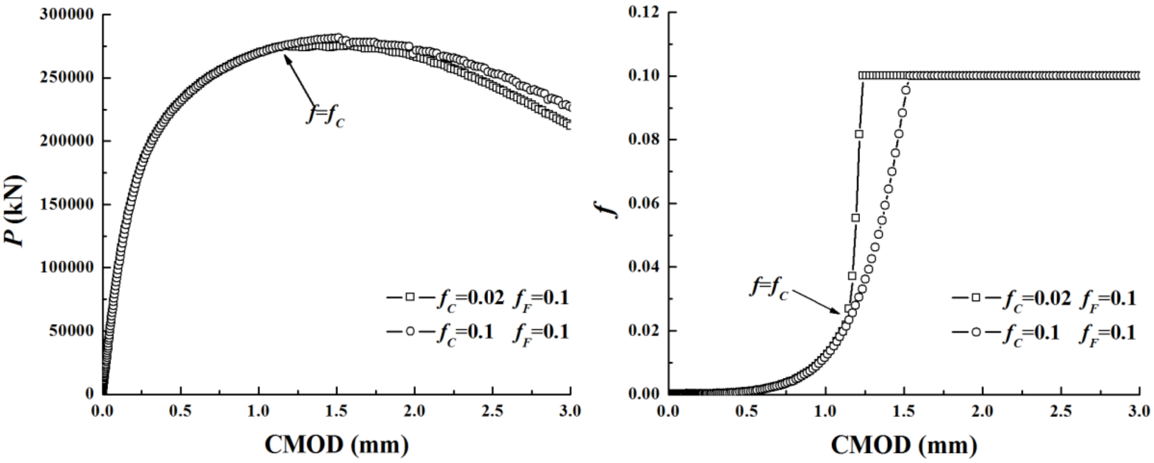

(a) *P*-CMOD curves **(b) *f*-CMOD curves**

Fig. 2.7 Schematic illustration of Eqs. (2.6), (2.7) and (2.8) (from 2D FEA)

According to the plastic limit load criterion proposed by Thomason [37], the coalescence between micro-voids results from the plastic limit load (microscopic internal necking) of the matrix between them. At the beginning of deformation, micro-voids are small and the stress follows a homogenous deformation state during nucleation and growth. As VVF increases and the plastic deformation develops, the stress needed for localized deformation decreases and a bifurcation is reached at this point [50]. The localized deformation of micro-voids is very different from the homogenous deformation of micro-voids and both need to be considered during coalescence. The plastic limit load criterion at a specific loading level is given by:

$$\begin{cases} \dfrac{\sigma_1}{\sigma_f} < \left[\alpha_{coal}\left(\dfrac{1}{r_{pll}} - 1\right)^2 + \dfrac{\beta_{coal}}{\sqrt{r_{pll}}}\right]\left(1 - \pi {r_{pll}}^2\right) \quad \text{(No coalescence)} \\ \dfrac{\sigma_1}{\sigma_f} = \left[\alpha_{coal}\left(\dfrac{1}{r_{pll}} - 1\right)^2 + \dfrac{\beta_{coal}}{\sqrt{r_{pll}}}\right]\left(1 - \pi {r_{pll}}^2\right) \quad \text{(Coalescence)} \end{cases} \tag{2.14}$$

$$r_{pll} = \frac{2\sqrt[3]{\left(\dfrac{3f}{4\pi}\right) e^{\varepsilon_1+\varepsilon_2+\varepsilon_3}}}{\sqrt{e^{\varepsilon_2+\varepsilon_3}}} \tag{2.15}$$

where

σ_1 is the maximum principle stress;

r_{pll} is the void space ratio;

ε_1 is the maximum principle strain, ε_2 and ε_3 are the other two principle strains;

$\alpha_{coal} = 0.1$ and $\beta_{coal} = 0.12$ are the fitting coefficients for non-hardening materials; $\alpha_{coal}(n_{R\text{-}O}) = 0.12 + 1.68(n_{R\text{-}O})$ and $\beta_{coal} = 0.12$ for hardening materials in Thomason's model. For cases where void shape, hardening and initial void volume fraction are varied, $\alpha_{coal}(n_{R\text{-}O}) = 0.1 + 0.217\, n_{R\text{-}O} + 4.83\, {n_{R\text{-}O}}^2$ $(0 \le n \le 0.3)$ and $\beta_{coal} = 0.124$ improved by Pardoen et al. [57], where $n_{R\text{-}O}$ is the hardening exponent in Ramberg-Osgood fit.

Zhang et al. [50] took into account these two competing modes of deformation and proposed the CGM based on the GT model. In CGM, the value of f_C is the material response to coalescence (the so-called field quantity), which is automatically determined, rather than a material constant. It was found that only for small f_0 as a first approximation, can f_C be approximated as a constant. The CGM has been implemented in ABAQUS using a user material subroutine UMAT developed by Zhang et al. [58, 59]. The model has been shown to be accurate for any level of stress triaxiality, as well as for non-hardening and hardening materials. Numerous studies have adopted this coalescence model, including [26, 60-62].

The linear traction-separation model was proposed by Ruggieri et al. [53] and Gullerud et al. [63], and has been implemented in WARP3D, an open source code for 3D nonlinear finite element analysis of solids. This model implements a failure criterion of f in the GT model: when the value of f reaches f_F, the cell element starts to be extinct and the remaining fraction of the internal nodal force reduces to zero in a linear fashion. The linear traction-separation model is an extension of GT model, and typically does not include the critical void volume fraction f_C (see [5, 53, 64-66]).

2.4 Computational cell methodology

The computational cell methodology (CCM) was originally proposed by Xia and Shih [67, 68] in a 2D configuration, and later extended to the 3D configuration by Ruggieri et al. [53] and Gao et al. [65]. Figure 2.8(a) simplifies the void-containing FPZ in Fig. 1.2(b) by replacing the FPZ with one layer of computational cells.

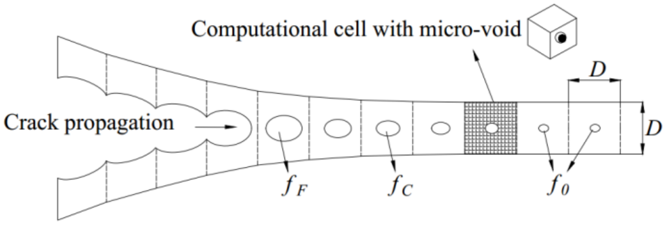

(a) Simplified computational cell model

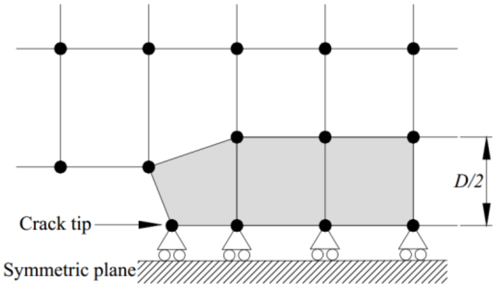

(b) Cell element on one side of the FPZ within FE framework

Fig. 2.8 Modelling of ductile crack growth using CCM

CCM contains a realistic void nucleation-growth-coalescence mechanism, as well as a microstructural length scale D which is physically coupled to the height of the FPZ. Here, D roughly represents the mean spacing between the voids nucleated from large inclusions [53, 68]. The FPZ layer consists of two layers of cubical cell elements on each side with a linear dimension of $D/2$ and thus, each computational cell is sub-divided into four computational cell elements (see Fig. 2.8(b)). Each cell element contains an initial (smeared) void volume fraction f_0, which equals the initial void volume divided by the entire cell volume. f_0 is related to the metallurgical features of the material. Within the thin layers that are symmetrically located about the crack plane, ductile crack extends through void growth and coalescence, that is, as the initial void volume ratio f_0 grows to a critical void volume ratio f_C, and till the extinction void volume fraction at failure f_F, the surface traction exerted by the FPZ on its surroundings increases first and finally reduces to zero, which characterizes the crack propagation along the crack surface. Elsewhere, the background material obeys the conventional J_2 flow theory of plasticity with no damage by micro-voids and does not affect the macroscopic toughness appreciably [53]. In this way, the growth and coalescence of voids and the interaction between FPZ and the background metal is modelled using CCM.

Numerous studies have applied CCM to model ductile fracture and predict resistance in structures with crack-like defect. Faleskog et al. [69], Gao et al. [65] and Ruggieri et al. [53] studied the calibration process of the GT model parameters based on CCM. Qian [64] studied the out-of-plane length scale of the computational cells using FEM code WARP3D. Within CCM framework, Gullerud et al. [63] investigated computational load step size, procedures to remove cells with high porosity and the porosity for cell deletion. Ruggieri et al. [70, 71] and Chen et al. [62] extended the applicability of CCM from laboratory specimens to pipe sections. Bolinder [72] numerically simulated the ductile crack growth in residual stress fields. Based on these previous studies, CCM are applied in this thesis.

2.5 Micromechanical parameters

2.5.1 Overview

The micromechanical parameters CCM include nine GTN parameters and two length scale parameters as summarized in Fig. 2.9.

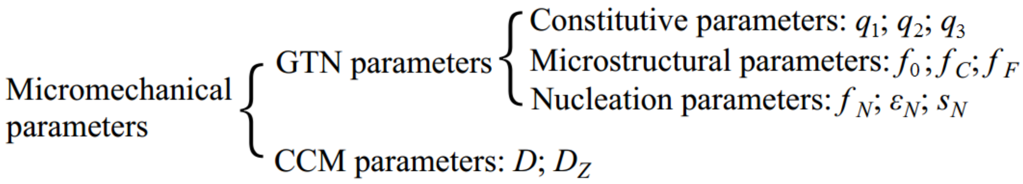
Micromechanical parameters
GTN parameters
Constitutive parameters: q_1; q_2; q_3
Microstructural parameters: f_0; f_C; f_F
Nucleation parameters: f_N; ε_N; s_N
CCM parameters: D; D_Z

Fig. 2.9 Micromechanical parameters

Among these eleven parameters, the in-plane length scale D and the initial void volume fraction f_0 are two key parameters that affect ductile fracture behavior significantly. Ruggieri et al. [53] suggested to select D first and then determine a suitable value for f_0 since each change of D consumes much more effort than changing f_0. In their study, it was confirmed that the less costly, plane strain analysis of SE(B) specimens could predict adequately the in-plane constraint effect in terms of R-curve before conducting extensive 3D FEA. However, the non-uniqueness problem has been a limitation of the CCM, which has been reported in many pervious studies [30, 73]. Qian [64] found that the calibrated f_0 increases with the in-plane length scale D. Zhang et al. [50] fit f_C from tensile tests and found an infinite number of pairs of (f_0, f_C) that gave identical predictions. They attributed this to the failure of Gurson model to automatically predict void coalescence. Oh et al. [74] found two sets of parameters that could well present σ-ε relation for a smooth tensile bar. This problem was discussed by Kiran et al. [30] and Benseddiq et al. [73]. Li et al. [75] pointed out that the non-uniqueness problem could be a fundamental feature of all damage theories involving tunable internal damage parameters. However, up to now, the limitation of non-uniqueness has not been well addressed due to the number of parameters and the great complexity involved during calibration.

2.5.2 *q*-parameters

The *q*-parameters are categorised as ‘constitutive parameters’ and depend on the yield strength and strain hardening properties of the material. Tvergaard et al. [76, 77] first suggested $q_1 = 1.5$, $q_2 = 1$ and $q_3 = 2.25$ for a moderately strain-hardening material based on micromechanical studies on periodically distributed voids. These values have become the most common option for subsequent studies (see Table A.1 in APPENDIX A).

Koplik et al. [78] compared the stress-strain numerically obtained by the cell model study and that obtained by void growth response with the Gurson model. $q_1 = 1.25$ and $q_2 = 1$ were found to achieve better agreement.

Perrin et al. [79] suggested that q_1 can be expressed as a function of VVF and that $q_1 = 1.47$ for VVF = 0. Note that this value is close to $q_1 = 1.5$ as suggested by Tvergaard.

Faleskog et al. [69] conducted extensive 3D FEA of discrete cell models containing a spherical void, covering a wide range of material hardening and strength properties. They improved the values of *q*-parameters by introducing an optimal table as well as optimal graphs for common structural steels. Subsequent studies such as [44, 80] have adopted this recommendation. Benseddiq et al. [73] further concluded that $q = q_1 \times q_2$ is approximately constant.

2.5.3 In-plane length scale *D*

It is well known that the in-plane length scale *D* (the dimension in the crack advancement direction) of the computational cell affects the numerical results using local approach [38, 73, 81, 82], which is the so-called element size dependent problem. The reason for this problem is related to the microstructural length scale (e.g. the average spacing of inclusions or voids for ductile fracture) of the material, which couples the physical length with computational model [54].

Roy et al. [83] adopted the intercept method [80] and defined the mean center-to-center particle spacing λ_s as:

$$\lambda_s = D = \frac{1}{2} d \sqrt{\frac{3}{2}} \sqrt{\frac{\pi}{f_v}} \tag{2.16}$$

in which

$$d = \sqrt{\frac{3}{2}} l_m \tag{2.17}$$

$$f_v = N_v \cdot d \tag{2.18}$$

where

d is the mean particle diameter;

l_m is the mean linear intercept;

f_v is the volume fraction of particle;

N_v is the number of carbides per unit length.

A rough estimate of fracture process zone size was made by Devaux et al. [81]:

$$D \approx \frac{2}{\sqrt[3]{N_v}} \tag{2.19}$$

where

N_v is the number of inclusions per unit volume.

Another approximate estimate was made from J_{IC} measurement, which is valid only for small-scale yielding (SSY) [81] or elastic solids (e.g. fatigue or brittle rupture) [16]:

$$J_{IC} = \chi \ln \left(\frac{R}{R_0} \right)_C D\sigma_0 \tag{2.20}$$

where

J_{IC} is the J integral value at the beginning stage of material crack growth resistance development;

χ is a numerical constant which depends on the mesh configuration of the crack tip. For square meshing and reduced Gauss integration, $\chi = 4$;

$(R/R_0)_C$ is the critical void growth ratio in the uncoupled model [31], and R is the radius of the cavity.

Shih [84] concluded that the calibrated D should be comparable to the experimentally measured value for CTOD at the initiation of ductile tearing, and proposed the following equation to determine CTOD at crack initiation:

$$D \approx \delta_{IC} \approx d_n \frac{J_{IC}}{\sigma_Y} \tag{2.21}$$

where

δ_{IC} is the critical CTOD value corresponding to J_{IC};

d_n is a non-dimensional constant ranging from 0.3 to 0.6.

Gao et al. [65] subsequently measured the CTOD at fracture initiation to be around 0.3 mm. Thus, $D = 0.3$ mm was adopted in his study.

Østby et al. [85] compared the stress fields ahead of the crack tip from initially square-shaped elements and elements with an aspect ratio (the ratio of element dimension parallel to the crack surface and element dimension perpendicular to the crack surface) of 2 in 2D FEA. The former case presented strong oscillations in the stress field due to the additional constraint and fast void growth rate, and resulted in significant numerical problems. On the other hand, the latter case showed a much smoother result and thus was recommended for constructing 2D FE models. This recommendation has been adopted in numerous studies [17, 60, 61, 86, 87].

2.5.4 Initial VVF f_0

In 1969, Franklin proposed the following equation for estimating f_0 [88]:

$$f_v = 0.054\left(S(\text{wt.}\%) - \frac{0.001}{\text{Mn}(\text{wt.}\%)}\right) \tag{2.22}$$

$$f_0 = f_v \frac{\sqrt{d_x d_y}}{d_z} \tag{2.23}$$

where

f_v is the volume fraction of manganese sulfide inclusions (MnS);

S(wt.%) and Mn(wt.%) represent the mass fraction of sulphur and manganese in the manganese sulfide inclusions, respectively;

d_x, d_y, d_z are average dimensions of the inclusion in tension direction, and in two perpendicular directions. For a spherical inclusion, it is assumed that $f_0 = f_V$.

Another method for estimating f_0 is the so-called 'quantitative microscopic optical technique' based on direct observation. This method has been adopted by Sun et al. [89], Penuelas et al. [26] and Nonn et al. [90]. The size, shape, and distance of both inclusions and developing voids were quantitatively evaluated using a fully automatic image processing technique. They found that f_0 lies in the range of 0.00015 to 0.00057.

The most common way to determine f_0 is by calibration with experimental results. Han et al. [91] conducted a sensitivity analysis of the effect of f_0 on CMOD-Δa curve for SE(B) specimen made of X65-grade steel and determined f_0 = 0.00015. Ruggieri et al. [70] calibrated f_0 based on the J - R curve tested from an X70-grade steel at room temperature using standard, deeply-cracked C(T) specimen. Qian [64], Zhang et al. [50] and Bolinder [72] focused on matching the numerical load-displacement records with the experimental ones and respectively adopted 0.00035, 0.0008, and 0.0065 for f_0.

2.5.5 Critical VVF f_C

The critical VVF f_C signifies the onset of coalescence and governs the accelerated void volume growth. f_C was found to be weakly dependant on stress triaxiality and matrix strain hardening and strongly dependant on f_0 by Koplik et al. [78]. In their study, it was assumed that f_C depends on f_0 only, which led to f_C = 0.3 and 0.055 for f_0 = 0.0013 and 0.0104, respectively. These values are consistent with those determined by Becker et al. [92], that f_C = 0.12, 0.06 and 0.04 for f_0 = 0.07, 0.026 and 0.004, respectively. Note that these f_C values are smaller than 0.15 as suggested by Tvergaard et al. [51].

According to Zhang et al. [93], f_C is not a constant parameter, but decreases with increasing stress triaxiality and should be determined by fitting. This was later supported by Steglich et al. [54], who found that f_C decreases with increasing triaxiality based on numerical study. It was also supported by the experimental studies conducted by Guillemer et al. [94], in which f_C was evolved as a function of h, the stress triaxiality state:

$$f_C = 0.255 - 0.145h \tag{2.24}$$

A logarithm relation between f_C and f_0 was obtained by Benseddiq et al. [73]:

$$f_C = 0.0186 \ln f_0 + 0.1508 \tag{2.25}$$

In their study, they found for small values of f_0, f_C varied little between 0.02 and 0.04. However, it was shown that f_C could not be treated as a constant for large f_0 value (i.e. $f_0 \geq$ 1%).

A unique combination of f_C and f_F values that best match the experimental load-displacement history was obtained by Kiran et al. [30]. 36 possible combinations (i.e. $f_C \in$ [0.02, 0.45] and $f_F \in$ [0.1, 0.5]) with fixed nucleation parameters were conducted and the best prediction was f_C = 0.03 and f_F = 0.5. In most recent studies, Dybwad et al. [95] and Han et al. [91] employed f_C = 0.13 to numerically simulate the ductile tearing process of X65-grade steel.

2.5.6 VVF at failure f_F

The VVF value at failure governs the final failure of the material. Tvergaard et al. [51] first suggested that f_F is not much larger than 0.2, and can be set at 0.25. Subsequently, Gao et al. [65] conducted numerical simulations of cell models and suggested that the value of f_F is only weakly dependent on constraint or matrix strain hardening, but is strongly dependent on f_0. A large value of f_F from 0.15 to 0.2 was suggested.

Zhang et al. [50] suggested using the following equation to estimate f_F:

$$f_F = 0.15 + 2f_0 \tag{2.26}$$

Equation (2.26) implies that f_F can be taken as 0.15 for a low f_0 value as a first approximation. Other empirical equations from 2D analysis based on CGM were obtained by Xu et al. [60] as:

$$f_F = 0.2 + 2f_0 \tag{2.27}$$

and by Li et al. [61] as:

$$f_F = 0.2 + f_0 \tag{2.28}$$

Benseddiq et al. [73] rearranged Eq. (2.6) and (2.7) as follows:

$$f_F = f_C + \frac{1/q_1 - f_C}{\delta_a} \tag{2.29}$$

They demonstrated that f_F could be calculated if the values of q_1, f_C and δ_a are known. If the value of f_C is small, a first approximation of f_F could be given as:

$$f_F = \frac{1}{\delta_a q_1} \tag{2.30}$$

δ_a was suggested to be a small value between 1 and 2.

Kiran et al. [30] found that f_F is the most sensitive one to the mesh size among all micromechanical parameters. A power-law relation between f_F and $D/2$ was proposed:

$$f_F = 0.041(D/2)^{-0.88} \tag{2.31}$$

Bolinder et al. [72] concluded as long as f_C and f_F are within the range of [0.15, 0.2], they would not present a significant impact on *J-R* curve.

2.5.7 Nucleation strain ε_N

In plastic strain-controlled nucleation criterion, the nucleation strain ε_N controls the plastic strain level at which the secondary voids nucleate. In general, ε_N varies between 0.3 and 0.9 in previous studies (see Table A.1 in APPENDIX A). A small value of ε_N initiates the fracture at an early deformation level, whereas a large value of ε_N postpones the fracture to a large deformation level [64].

Kiran et al. [30] demonstrated the effect of ε_N based on an analysis of uniaxial tensile loading on a unit cube (i.e. 8-node brick element with reduced integration) carried out in ABAQUS. It was concluded that the behavior of the cube before the onset of ε_N is equivalent to that of a J_2 plasticity model. The authors further illustrated the non-uniqueness problem of (ε_N , f_N) parameter pair: early nucleation (i.e. low ε_N value) and small number of voids growth (i.e. low f_N value) has the same effect with late nucleation (i.e. high ε_N value) and large number of voids growth (i.e. high f_N value).

Tensile tests were carried out and ε_N was measured experimentally using scanning electron microscopy (SEM) by Le Roy et al. [83], Kwon et al. [96] and Qiu et al. [97]. Observation of high deformation value to nucleate a significant number of micro-voids at the second phase particles was made. The areal density of voids N_A was measured at different plastic strains and were denoted as N_A - ε^{pl}. The mean void nucleation strain was determined when rapid increase of areal density was observed.

The elastic-plastic response of a single cell under uniaxial strain was analysed by Ruggieri et al. [53]. It was found that at a plastic strain of $\varepsilon^{pl} = 0.3\varepsilon_N - 0.4\varepsilon_N$, the void grows rapidly and the macroscopic stress falls sharply. Thus, ε_N is determined as a relatively large value (i.e. $\varepsilon_N = 0.75$) to make the acceleration process well beyond the plastic strain where the peak stress develops.

2.5.8 Void volume fraction of nucleated voids f_N

The parameter f_N controls the amplitude of the accelerated growth rate. Generally, f_N can be evaluated by microscopic examination of the undamaged material [73]. Ruggieri et al. [53] suggested using a pair of (s_N , f_N) with large values to produce an accelerated and smooth reduction of the stress-carrying capacity and void acceleration process.

Another way to determine f_N is calibration with experiments. Ishikawa et al. [98] conducted tensile test and calibrated f_N using load-displacement record. When $f_N = 0.005$, a sudden load drop that led to ductile fracture was captured in the GT model. It was also found that the load drop occurred earlier with an increasing f_N value.

Cuesta et al. [82] suggested that ε_N and f_N govern the shape of the load-displacement curve at the pure plastic stage of a punch test. Given an almost linear behavior, the curve was adjusted to a straight line:

$$P = m_1 \Delta l + m_2 \tag{2.32}$$

where

$$m_1 = g_1(\varepsilon_N, f_N) \tag{2.33}$$

$$m_2 = g_2(\varepsilon_N, f_N) \tag{2.34}$$

in which

$g_1(\varepsilon_N , f_N)$ and $g_2(\varepsilon_N , f_N)$ are postulated as quadratic models of the form:

$$g(\varepsilon_N, f_N) = l_0 + l_1\varepsilon_N + l_2 f_N + l_{11}\varepsilon_N^2 + l_{22} f_N^2 + l_{12}\varepsilon_N f_N \tag{2.35}$$

where

Δl is the punch displacement;

m_1 and m_2 are the line parameters;

g_1 and g_2 are the quadratic functions;

l_0, l_1, l_2, l_{11}, l_{22}, l_{12} are the fitting coefficients.

In their study, a desirability study and the Pareto front method were used to address the multi-objective problem in order to obtain ε_N and f_N. The desirability study involved a desirability function which was a previous weighting of individual objectives, while the Pareto front method represented the entirety of the optimum solutions for each of those objectives. Results showed that the error of the Pareto Front method was small and thus $\varepsilon_N = 0.1979$, $f_N = 0.0292$.

2.5.9 Standard deviation of nucleation strain s_N

The parameter s_N controls the rate of nucleation. The nucleation function A_1/f_N of plastic-strain controlled nucleation criterion is shown in Fig. 2.10. For fixed values of ε_N and f_N, a larger value of s_N enlarges the nucleation of new voids to a wider range of plastic strain, whereas a smaller value of s_N narrows the nucleation of new voids to a narrower range of plastic strain. A small value (i.e. $s_N = 0.01$) was suggested for homogeneous material by Cuesta et al. [82], whereas Ruggieri et al. [53] selected a larger value of $s_N = 0.01$ for A533B steel and A516-70 steel to achieve smooth stress reduction in both high and low constraint cell analysis.

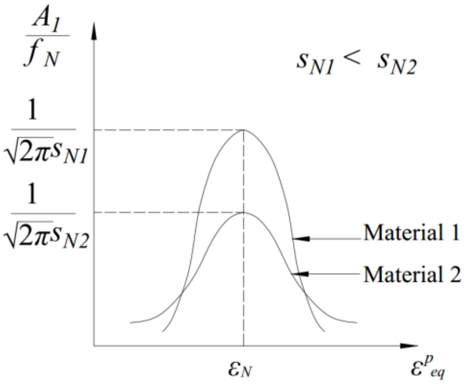

Fig. 2.10 Nucleation function A_1/f_N

2.5.10 Out-of-plane length scale D_Z

The out-of-plane mesh (the dimension along the crack front) configuration was found to affect the predicted crack-front profile strongly because the varying stress and strain fields over the crack-front initiate varying void growth rates. Ruggieri et al. [53] assigned various numbers of elements in the thickness direction with the thinnest layers defined at the side groove. Layers of nine were adopted with satisfaction. However, a coarse mesh with seven uniform thickness layers was found insufficient to match the experimental result at the side grooves.

A systematic study of out-of-plane length scale of the computational cell was conducted by Qian [64]. It was found that fracture resistance and crack extension are highly dependent on the element thickness in the out-of-plane direction. Conclusions were drawn that for PS specimen, D_Z near the free surface need to be smaller than $2D$, whereas for SG specimen, D_Z near the side grooves need to be smaller than D to achieve the convergence of *J-R* curve and crack-front profile.

The micromechanical parameters in literature are reviewed and tabulated in Table A.1 in APPENDIX A.

2.6 Application of the Gurson model

The application of the Gurson type constitutive model is summarised as follows:

i). Constraint effect:

Fracture toughness is usually not a material constant but is geometry, loading mode and stress-state dependant [91]. A high constraint level in the crack-tip region corresponds to high stress triaxiality and thus leads to low fracture toughness, as discussed at the beginning of this chapter. Numerous studies [85-87, 91, 98-101] have employed the Gurson type constitutive model to investigate the crack-tip constraint effect. For example, Han et al. [91] proposed a quantitative relation between stress triaxiality and CTOD value for X65-grade steel. Betegón et al. [99] investigated the crack-tip constraint effect by examining the *J-R* curve and equivalent plastic strain contour.

ii) Material mismatch:

The microstructural properties of crack-like defects located at weld joint or HAZ are altered by the heat during welding or cutting operations. The change of microstructural properties then introduces material mismatch and impacts the local fracture resistance behaviour. The Gurson type model has been applied to investigate material mismatch in previous studies [26, 85, 102-104]. For example, Rakin et al. [103] investigated the effect of strength mismatch and effect of width of welded joints on the load-displacement history of SE(B) specimen. Fan et al. [105] developed *J-R* curve and triaxiality contour for SE(B) specimen made of bi-materials with various geometry and material constraints. Østby et al. [85] studied the effect of hardening mismatch and strength mismatch by examining the *J-R* curve of SE(B) and SE(T) specimens, crack tip opening stress, and crack growth direction. Nègre et al. [102] studied the ductile tearing process of laser welded Al sheets based on GTN model.

iii). Ductile fracture prediction:

The ability of Gurson model to simulate the fracture behavior of laboratory fracture specimens and full-scale pipe sections has been well studied in the past [5, 66, 71, 100, 101, 106]. For example, Kiran et al. [30] predicted the ductility of tension bars, plates with reduced section and plates with holes in terms of load-displacement curve and fracture initiation location. Benseddiq et al. [73] simulated the ductile tearing process of tensile notched round specimens and C(T) specimens. Ruggieri et al. [53] conducted 3D FE modelling of stable crack extension of SE(B) and CT specimens. Gao et al. [65] predicted the fracture behavior of SE(B) and SE(T) specimen. Peñuelas et al. [26] studies the fracture behavior of SE(B) specimens fabricated from welded joints. Sarzosa et al. [100, 101] modelled circumferentially surface cracked pipes made of X70-grade pipeline steel subjected to remote bending. Dotta et al. [5] described the crack growth process of pipeline specimens with longitudinal crack-like defect made of X60-grade steel in a 2D configuration. Ruggieri et al. [71] predicted the crack extension of longitudinal crack-like defects on a full-scale pipeline section in a 3D configuration. The experimentally measured burst pressure for the tested cracked pipes matched well with the FEA results. Hippert et al. [106] predicted the burst pressure of a thin-walled gas pipeline containing longitudinal cracks with varying crack depth to thickness ratios.

v). Dynamic fracture analysis:

The Gurson model has also been applied to dynamic fracture analysis. Cuesta et al. [82] simulated small punch tests due to the lack of enough material for conducting conventional fracture tests. In the studies by Scheider et al. [107] and Nonn et al. [90], dynamic drop weight tear tests were simulated to calibrate micromechanical parameters, then followed by the simulation of dynamic fracture propagation in pipe sections. The effect of crack meandering on dynamic ductile fracture was numerically studied for a pre-cracked specimen subjected to impulsive tensile loading at one end by Tvergaard et al. [108, 109] and Mathur et al. [110]. Furthermore, Needleman et al. [111] studied the mesh sensitivity of dynamic fracture initiation time for cases where large-scale or small-scale voids dominate in the material.

Other than the above-mentioned applications, the Gurson type models have been applied to investigate the plastically anisotropy and kinematic hardening of materials [33]. In the region of low constraint, shear-lip or mixed-mode (slant) fracture may develop [53] and the Gurson model was proved to be not adequate describe this region. The GTN model was modified by Nahshon et al. [112] and Xue et al. [113] to predict damage growth under shear-dominant loading conditions. In conclusion, the Gurson type and its subsequently modified versions have been widely applied to investigate ductile fracture mechanism and behavior. In addition, based on the computational cell methodology, the constitutive model is implemented in cell elements and enables conducting extensive 2D/3D FE. Several limitations of the Gurson type models still need to be addressed, including the non-uniqueness of micromechanical parameters and the transferability validation of parameters between small-scale specimens and full-scale structures.

Chapter 3 Numerical modelling of ductile crack growth

3.1 Previous test results

In this chapter, numerical analyses are carried out on the fracture toughness specimens previously tested by Wang et al. [114]. In their study, six clamped SE(T) specimens and four SE(B) specimens made of X80-grade pipeline steel were tested. For clarity, the specimens are numbered as shown in Table 3.1, where ‘PS’ denotes plane-sided specimens, ‘SG’ denotes side-grooved specimens, and ‘a_0’ denotes the initial crack length of the specimen. Note that the testing results of two SE(B) specimens (SG175-01 and SG175-02) were not reported in [114], but are included in the table. The crack planes of all specimens are out-surface-notched and circumferentially-oriented (i.e. crack extending in the through-wall thickness direction, see Fig. 3.1(a)).

Table 3.1 Specimen number

Specimen ID	a_0/W	PS/SG
SE(T)-PS05-01	0.5	PS
SE(T)-PS05-02	0.5	PS
SE(T)-SG05-01	0.5	SG
SE(T)-SG05-02	0.5	SG
SE(T)-SG25-01	0.25	SG
SE(T)-SG25-02	0.25	SG
SE(B)-SG175-01	0.175	SG
SE(B)-SG175-02	0.175	SG
SE(B)-SG25-01	0.25	SG
SE(B)-SG25-01	0.25	SG

All the specimens in Table 3.1 have $B = W = 20$ mm (see Figs. 3.1(b) and (c)). The SE(T) specimens have a daylight-to-width ratio of $H/W = 10$ (see Fig. 3.1(b)). The two shallow-cracked SE(T) specimens ($a_0/W = 0.25$) are side-grooved, with the side groove depth on each side equal to 7.5%B. For those four deeply-cracked SE(T) ($a_0/W = 0.5$) specimens, two are side-grooved and two are plane-sided. The SE(B) specimens have a span-to-width of $S/W = 4$ (see Fig. 3.1(c)). All four SE(B) specimens are shallow-cracked ($a_0/W = 0.25$ and 0.175) and side-grooved with the depth of the side groove on each side equal to 10%B. The integral knife edge is adopted to assist the measurement of the crack mouth opening displacement (CMOD) using a clip-on gauge. The initial fatigue pre-crack is introduced by using a three-point bend apparatus for all specimens. Side grooves are then fabricated after fatigue pre-cracking to promote uniform crack growth over the thickness direction, if needed.

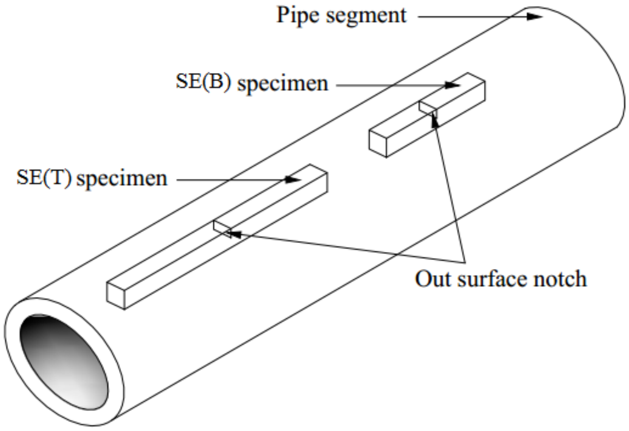
Pipe segment
SE(B) specimen
SE(T) specimen
Out surface notch

(a) Orientation of SE(T) and SE(B) specimens

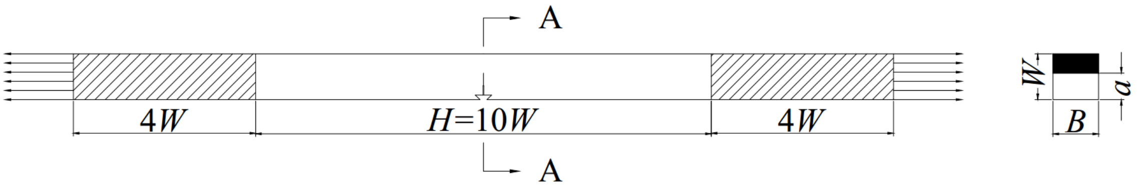
A
4W
H=10W
4W
A
W
a
B

(b) Clamped SE(T) specimen (*H*/*W* = 10)

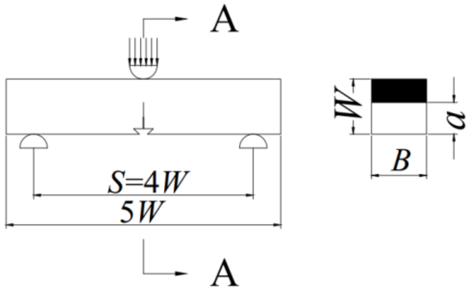
A
S=4W
5W
A
W
a
B

(c) Three-point bend SE(B) specimen (*S*/*W* = 4)

Fig. 3.1 Geometric information of fracture specimens

The experiments were conducted using an INSTRON 8804 servo-hydraulic testing system at room temperature. For the SE(T) specimens, the two ends of the specimen were clamped by the hydraulic grips. For the SE(B) specimens, the three-point bend load was applied through upper and lower rollers. During the tests, the system output load-line displacement (LLD), CMOD, and load P simultaneously. After the tests, the specimens were broken up to expose the crack plane for measuring the crack length. The physical initial crack length a_0 and final crack length a_f were measured using the 9-point average technique in accordance with the recommendation in ASTM E1820-17 [12]. More details about the testing procedures and results can be found in [114].

3.2 Material property

The values of Young's modulus E, 0.2%-offset yield strength σ_{YS} and ultimate strength σ_{TS} of the pipe steel used to fabricate the SE(T) and SE(B) specimens are 207 GPa, 520 MPa and 710 MPa, respectively. The density and Poisson's ratio are 7800kg/m^3 and 0.3, respectively. The stress-strain relationship of the X80-grade steel is determined using two tensile coupon tests in accordance with ASTM E8/E8M [115]. The tensile coupons are extracted in the pipe's longitudinal direction such that the obtained stress-strain relationship is representative of those of SE(T) and SE(B) specimens. The engineering stress-strain curves obtained from the two coupons are shown in Fig. 3.2(a), and the corresponding true stress-logarithmic strain curves are shown in Fig. 3.2(b).

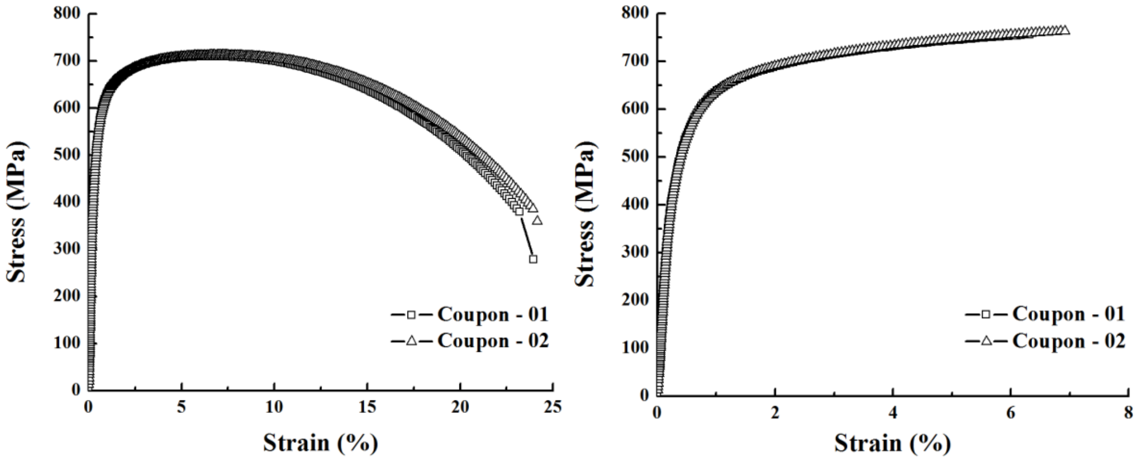

(a) Engineering stress-strain curves **(b) True stress-strain curves**

Fig. 3.2 Stress-strain curves

In addition to the above-mentioned material properties, damage parameters are also required for the material of GTN plastic flow law in FEA. A review of the micromechanical parameters has been presented in Table A.1 and the detailed calibration process is discussed in Section 3.4.

3.3 Finite element model and numerical procedure

3.3.1 Finite element model

The commercial finite element software ABAQUS 6.13 [116] is used to simulate the ductile crack extension for both SE(B) and SE(T) specimens. These FE models are established for the purpose of calibrating micromechanical parameters as well as investigating the crack-tip stress fields during the ductile crack growth. According to [65, 93], the 2D plane strain analysis of shallow-cracked SE(B) specimens gives a good estimate of the thickness average feature of the fracture response, in terms of the load-displacement history and the *J*-*R* curve. Thus, in this study the SE(B) specimens are analyzed by 2D FEA, while the SE(T) specimens are modelled using 3D elements to capture the crack plane profile. In this section, the 2D SE(B) FE model is first described, followed by 3D SE(T) FE models.

i). 2D FE model of SE(B) specimen:

For 2D SE(B) specimens in the plain strain condition, only half of the specimen is modelled due to the symmetry in the *y*-axis direction. A typical FE model (a_0/W = 0.25, B/W = 1, S/W = 4) is shown in Fig. 3.3(a), containing a row of 100 computational cells along the initial remaining ligament b_0 within the FPZ. Note that only the elements in this row are assigned with the GTN material property. The base metal (i.e. the region outside the FPZ) remains undamaged by void growth and the elastic-plastic constitutive law follows the J_2 flow theory with conventional von Mises plasticity.

The initially blunted crack tip (see Fig. 3.3(b)) accommodates the initiation of stable crack growth with blunted notch radius which equals to half of in-plane length scale $D/2$. This arrangement is proved to simulate the blunting process of the crack tip well as suggested by Østby et al. [85], Han et al. [91] and Sarzosa et al. [66].

The dimension of the computational cell element equals 0.15 mm × 0.15 mm. This dimension is found to be able to provide adequate resolution of the stress-strain fields near the crack tip and hold true for the resistance prediction after sensitivity analysis. The elements with this uniform dimension extends to 4.5 mm away from the symmetrical plane, with convergence validated. The element type is CPE4R. A half-symmetric model for 2D plane strain analysis shown in the figure has 4579 nodes and 4469 elements approximately. Note that the 2D SE(B) specimens with $a_0/W = 0.175$ have a similar mesh configuration.

Two contact rollers are defined to simulate the rollers supporting and loading the specimen. A smooth ramping amplitude of loading is applied through the upper roller, while the lower roller remains fixed. The load is displacement-controlled to ensure a smooth force-displacement increment. In all analyses, the ABAQUS/Explicit solver, in which the GTN failure criteria is implemented. The crack growth procedure is automatically captured by the element extinction by choosing the output 'STATUS' option.

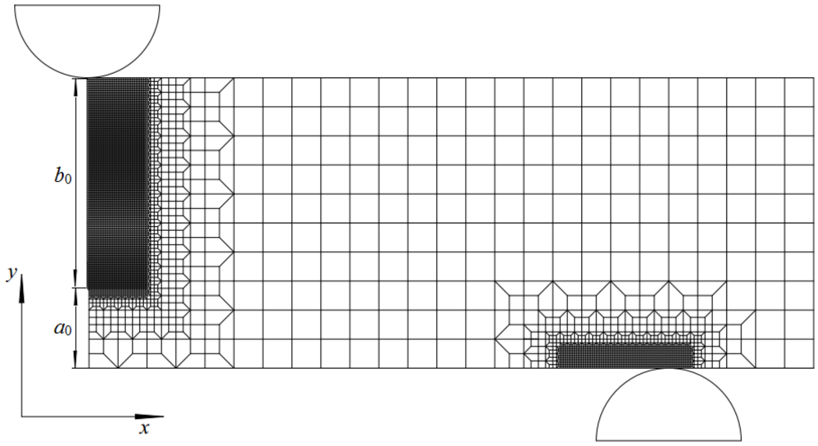

(a) Half of SE(B) specimen

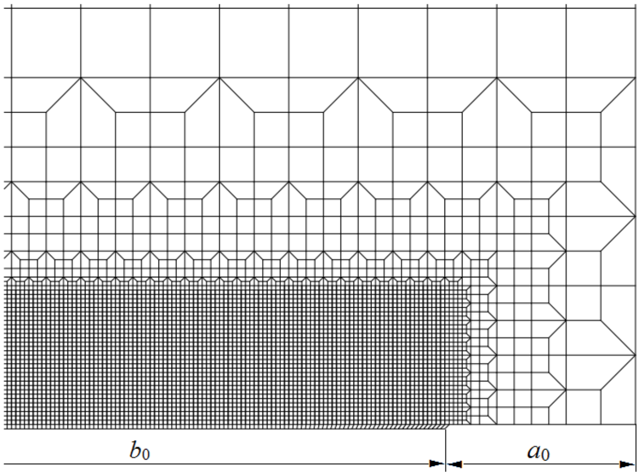

(b) Close-up view of the region near crack tip

Fig. 3.3 2D plane strain FE model of SE(B) specimen (a_0/W = 0.25)

ii). 3D FE model of SE(T) specimen:

Figure 3.4 shows the 3D FE model of a representative SE(T) specimen, SE(T)-SG25-01/02. Only a quarter of the specimen is established due to the symmetry in the *x*-axis and *z*-axis directions (see Fig. 3.4(a)). Appropriate constraint conditions are assigned to the symmetry planes accordingly. The PS specimen has no thickness reduction, whereas for SG specimen, the side groove is modelled as a sharp V-notch with a side groove angle equal to 45° and a root radius of *D*/2. Here, *D* = 300 mm is the in-plane length scale, same as that used in 2D FEA.

As for the meshing arrangement in the thickness direction, the model for the PS specimen is divided into 20 layers, with a bias ratio of 4. Note that the thickest layer is defined at the mid-thickness plane and the thinnest layer is defined at the free surface. For the SG specimen, 4 uniform layers of elements are constructed in the groove region, and 20-layer arrangement are assigned in the inner region with a bias ratio of 4, which is same as the PS specimen. The thinner elements are for capturing the details of crack growth near the root of the side groove or free surface. Note that these arrangements are consistent with the recommendations for the out-of-plane length scale given by Qian [64].

A structured transitional meshing pattern is assigned to the transitional part between the coarse mesh away from the crack tip and the fine mesh near the crack tip. The meshing refinement is identical throughout the thickness direction using the sweeping technique. The 8-node solid elements with the reduced integration (i.e. C3D8R elements) are used in the analysis. Note that specimens with different initial crack length or thickness have a similar meshing configuration as described here. A quarter model for the 3D analysis shown in the figure has 95049 nodes and 87636 elements. Similar to the 2D plane strain analysis, a smooth loading step is applied to the model through a remote clamping load, which is displacement-controlled. The non-linear large deformation analysis is chosen due to the large plastic ductile fracture behavior using the ABAQUS/Explicit solver.

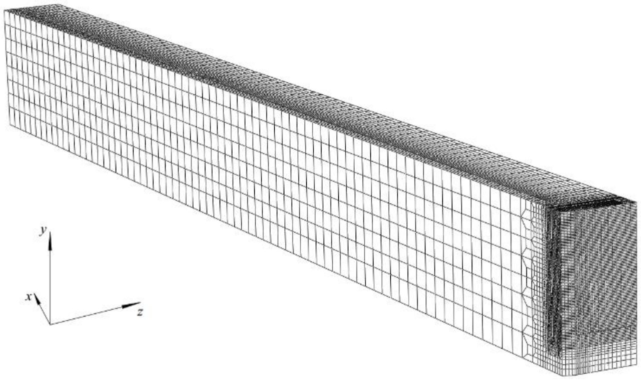

(a) A quarter of the SE(T) specimen

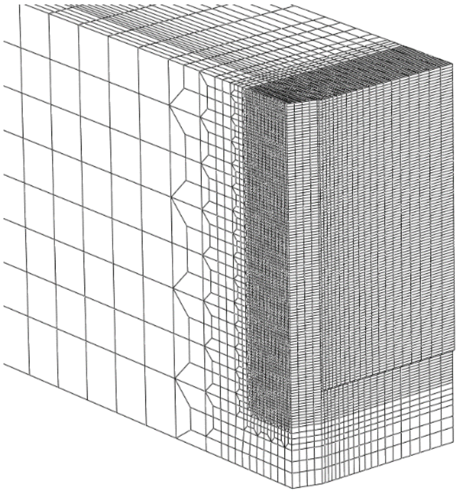

(b) Close-up view of the side groove and crack tip

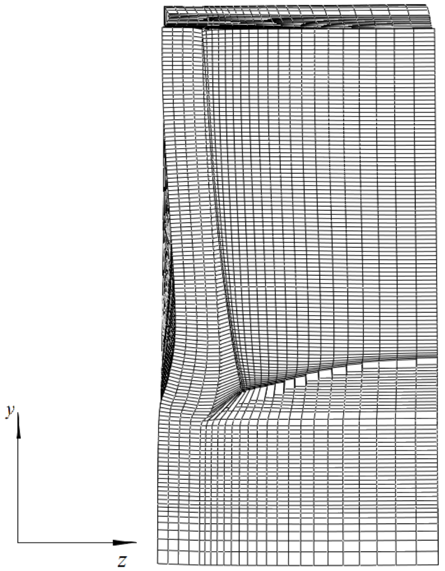

(c) Deformed mid-plane of the SE(T) specimen

Fig. 3.4 3D FE model of SE(T) specimen (SG, $a_0/W = 0.35$, $B/W = 1$)

3.3.2 Evolution of *P*, CMOD, CTOD, Δ*a*, and *J*-integral

In FEA, the load *P* is output by summing up all reaction forces to a reference point on the remote surface of the SE(T) specimen. This reference point applies rigid constraint to the clamping surfaces by the constraint option in ABAQUS. For SE(B) specimen, the load *P* is output by extracting the reaction force at the roller.

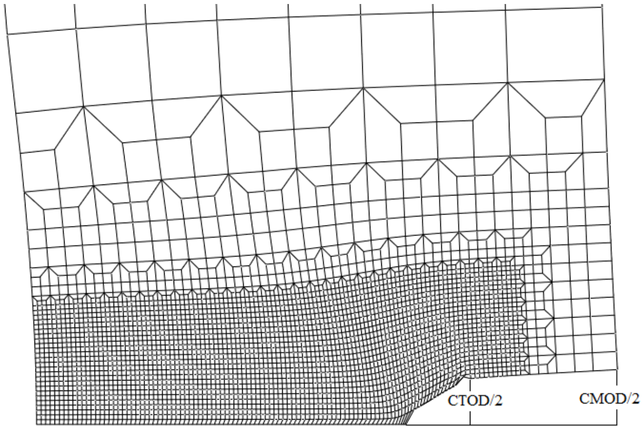

Fig. 3.5 Determination of CMOD and CTOD

The determination of CMOD and CTOD are shown in Fig. 3.5. It is a common practice to extract the CTOD value from a fixed node in front of the initial crack tip [60, 61, 81] and then multiply the value by 2.

Stable crack extension Δa is taken as the addition of the crack advance due to ductile tearing and crack blunting, approximated by one half of the measured CTOD, as recommended in [26, 86, 87, 105]:

$$\Delta a = \Delta a_d + \Delta a_b = \Delta a_d + \frac{1}{2}\delta \tag{3.1}$$

where

Δa_d is the crack extension due to ductile tearing;

Δa_b is the crack advance due to blunting correction.

The crack extension due to ductile tearing is calculated by multiplying the original element length by the number of damaged elements [60, 61] and the element is assumed to fail when VVF reaches f_F.

Since ABAQUS/Explicit solver does not allow the *J*-integral calculation in a domain integral procedure [105], the η_{pl}-method (elastic unloading compliance (UC) method) is used instead to develop *J-R* curves. The detailed procedure of the η_{pl}-method for the SE(B) specimen is described in ASTM E1820-17 [12], in which the corresponding equations (i.e. equations for the calculation of *K*, *C* and η_{pl}) for SE(B) specimen can be found. While the equations for SE(T) specimen are summarized in APPENDIX B.

3.4 Calibration of micromechanical parameters

3.4.1 Calibration using 2D model of SE(B) specimen

The two-step scheme [65, 93] suggests that the 2D plane strain analysis of shallow- cracked SE(B) specimens gives a good estimate of the thickness average feature of the response, in terms of the load-displacement history and *J*-*R* curve. Thus, in order to calibrate the micromechanical parameters of the computational cell elements, two SE(B) specimens with $a_0/W = 0.175$ (i.e. SE(B)-SG175-01 and SE(B)-SG175-02) are considered in a 2D plane strain configuration to save calculation time and calibrate damage parameters.

In the analysis, the *q*-parameters are chosen as the most commonly used values (i.e. $q_1 = 1.5$; $q_2 = 1$; $q_3 = 2.25$). Since $D/2$ and f_0 strongly impact the resistance curve behavior as discussed in Chapter 2, a 3×3 analysis matrix (i.e. $D/2 = 0.1$; 0.15; 0.2 and $f_0 = 0.00015$; 0.00075; 0.0015) is selected to find the best combination to match the experimental results. f_F is determined from the empirical equation (see Eq. (2.26)) by Zhang et al. [50]. Since f_C does not impact the fracture behavior strongly as long as it is within the range of [0.1,0.2], it is fixed at 0.13 according to [91]. For simplicity, the nucleation parameters are not considered in the current study.

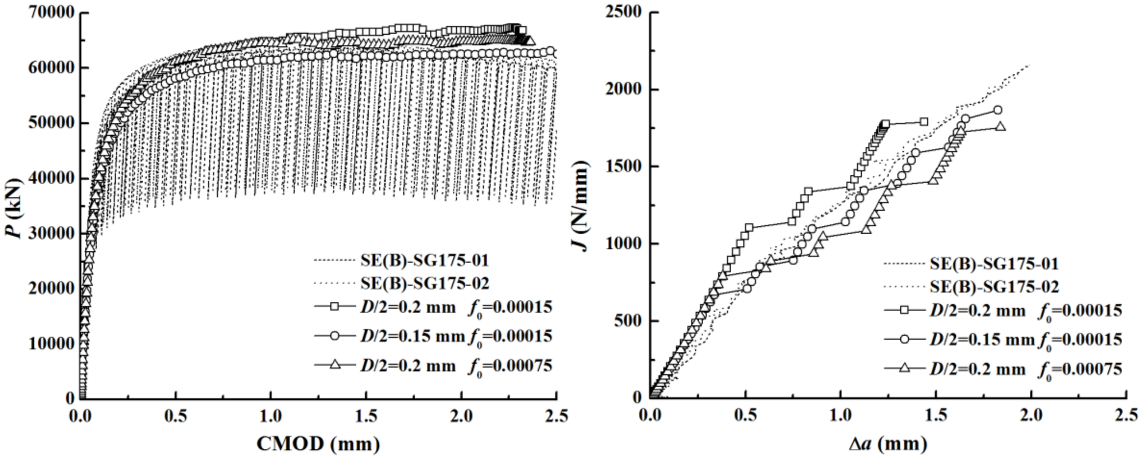

(a) *P*-CMOD curves **(b) *J*-*R* curves**

Fig. 3.6 *P*-CMOD curves and *J*-*R* curves for 2D SE(B) specimens with $a_0/W = 0.175$

Figure 3.6 shows the *P*-CMOD curves and *J-R* curves for the SE(B) specimens and FE models used for the calibration. For the purpose of clearly showing the figure, only three FEA results are plotted. As is observed in Fig. 3.6(a), the load-displacement history resulting from different models with different $D/2$ values are almost identical, which indicates that $D/2 = 0.20$ mm is adequate to capture the global behavior of the specimen. For models with different f_0 values, the load-displacement history is identical in the initial part, and slightly deviate afterwards, which indicates that a higher initial void volume ratio yields a lower load-carrying capacity.

It is shown in Fig. 3.6(b) that a larger $D/2$ value corresponds to a higher *J-R* curve. The figure also shows that the *J-R* curve scales almost proportionally with $D/2$, given that all the other parameters are fixed, which is consistent with the result reported in [53]. This can be explained by that a thicker layer requires more work to reach critical conditions. The smaller mesh size predicts earlier failure initiation and accelerated subsequent failure [74]. On the other hand, the resistance curves also indicate a significant role of f_0, which is consistent with the argument by Xia et al. [117], that an order of magnitude change in f_0 has a significant effect on the computed *J-R* curve. It is the cell strength which is governed by the initial porosity f_0 that plays the dominant role in characterizing the fracture toughness [53]. It is worth noting that the *J-R* curves present a 'step-like' behavior. This is because in 2D analysis, an individual element extinction at a step extends the crack length by one element size in a discreet manner, which is consistent with the results given in [50, 118].

Based on the calibration results, $D/2 = 0.15$ mm and $f_0 = 0.00015$ gives the best match. In such way, the micromechanical parameters are chosen as listed in Table 3.2, and will be further validated using other test specimens in the following section.

Table 3.2 Calibrated micromechanical parameters

$D/2$	q_1	q_2	q_3	f_0	f_C	f_F	Nucleation
0.15 mm	1.5	1	2.25	0.00015	0.13	0.1503	Not applied

3.4.2 Validation of calibrated micromechanical parameters

In this section, the calibrated micromechanical parameters (see Table 3.2) based on 2D FEA of SE(B) specimens with a_0/W = 0.175 are validated using the other two SE(B) specimens and six SE(T) specimens.

Figure 3.7 shows that both *P*-CMOD curves and *J*-*R* curves predicted from 2D plane strain FEA match reasonably well with those obtained from experiments for SE(B) specimens with a_0/W = 0.25.

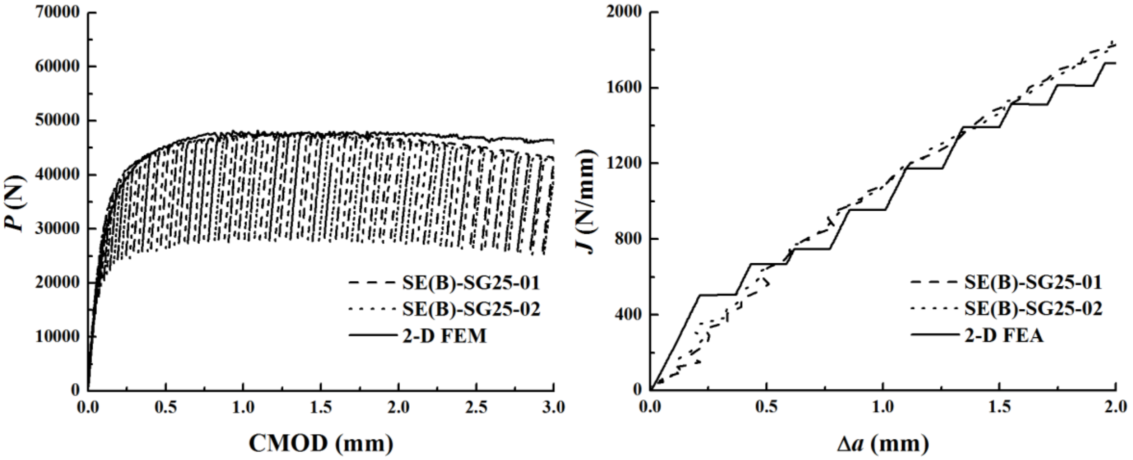

(a) *P*-CMOD curves for a_0/W = 0.25 **(b) *J*-*R* curves for a_0/W = 0.25**

Fig. 3.7 *P*-CMOD curves and *J*-*R* curves for 2D SE(B) specimens with a_0/W = 0.25

Figure 3.8 shows the *P*-CMOD and *J*-*R* curves for 3D SE(T) specimens. As can be seen in Fig. 3.8(a), the *P*-CMOD curves obtained from FE models are in good agreement with those obtained from experiments, especially for the PS specimens with a_0/W = 0.5. Some discrepancies exist in SG specimens with a_0/W = 0.5 and SG specimens with a_0/W = 0.25, but generally less than 10%. This is partly due to the anisotropic property of the material and the curvature of the initial crack front, neither of which is considered in the current FE models [62].

As for the *J*-*R* curve, good agreement is achieved in all cases. It is worth pointing out that given a certain CMOD value, slightly higher *P*-CMOD curves yet almost identical *J*-*R* curves are developed (see Figs. 3.8(b) and (c)). The reason can be explained as: in current FEA, a same CMOD value results in a slightly larger crack extension than that in real case, which leads to an almost identical resistance curve. In addition, different Δa correspond to different unloading compliance C, which affects the area under the P-CMOD curve. Many attempts have been made to achieve higher synchronized accuracy, however, current results are shown to be the best.

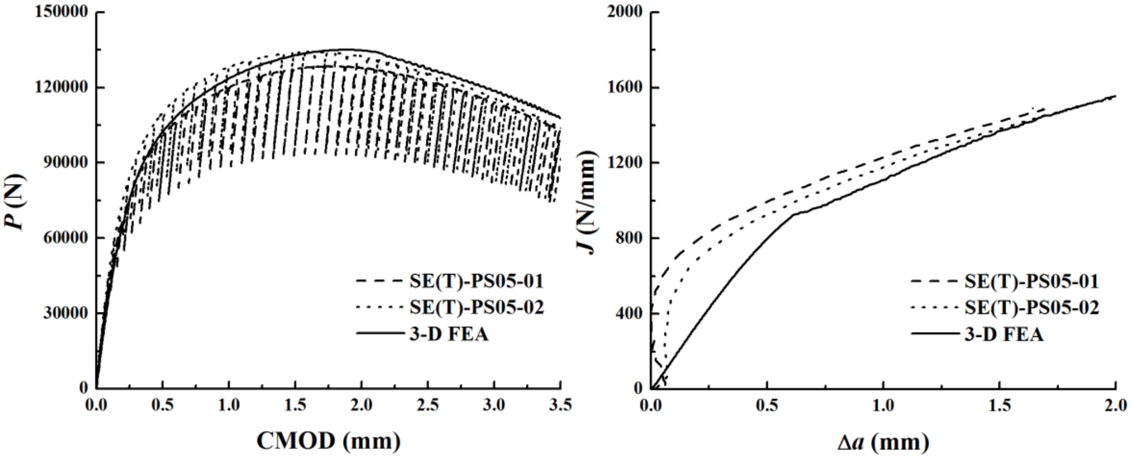

(a) PS specimens with a_0/W = 0.5

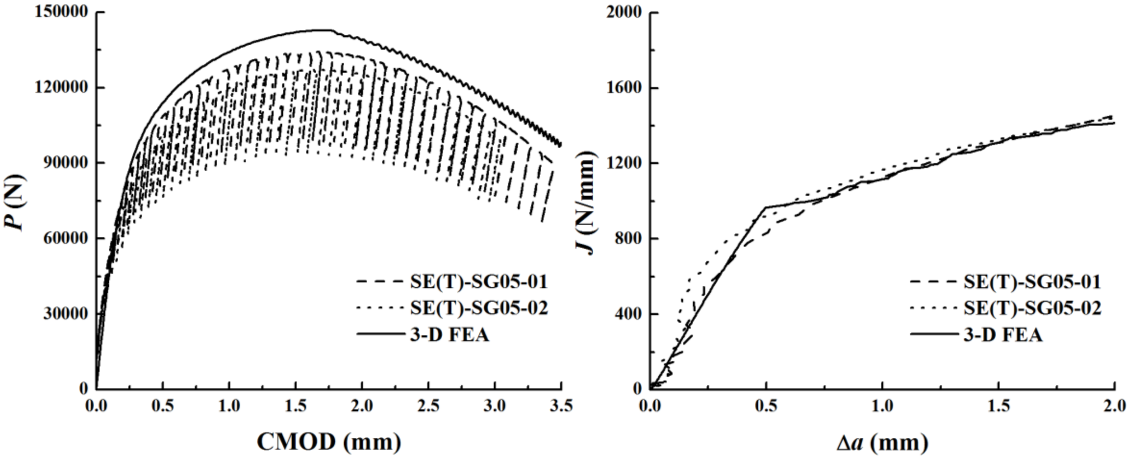

(b) SG specimens with a_0/W = 0.5

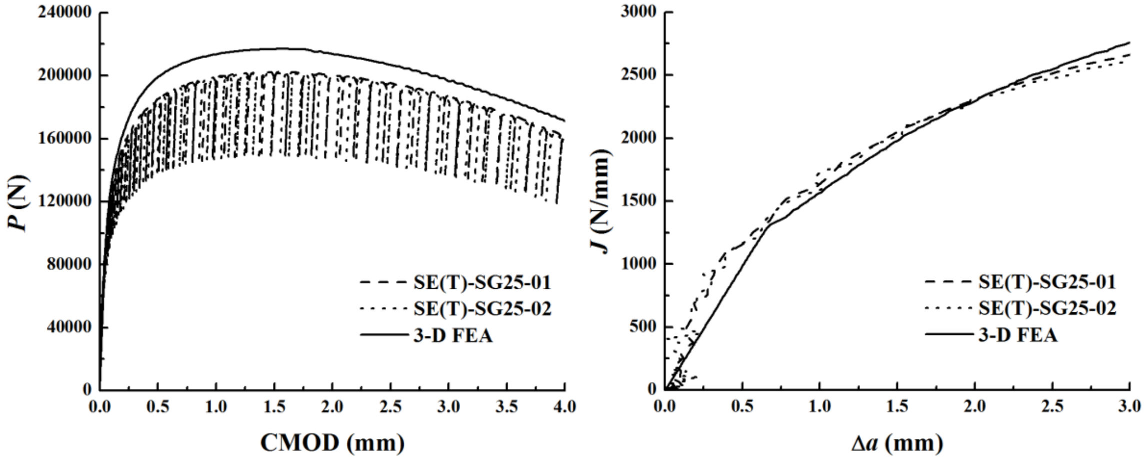

(c) SG specimens with $a_0/W = 0.25$

Fig. 3.8 *P*-CMOD curves and *J*-*R* curves for 3D SE(T) specimens

Figure 3.9 shows the comparison of the post-test measured and predicted crack front profiles. Note that the numerical models use perfectly flat initial crack fronts. The predicted crack extension at each location on the crack front in the thickness direction are then added to the initial crack front to construct the final crack front. It is clearly demonstrated that the 3D FE models are capable of simulating the tunneling effect in PS specimens (see Fig. 3.9(b)) and the reverse tunneling effect in SG specimens (see Figs. 3.9(a) and (c)). The results for SG specimens with $a_0/W = 0.5$ predicted by FE model (see Fig. 3.9(c)) is in excellent agreement with experimental results. However, for those SG specimens with $a_0/W = 0.25$ and PS specimens with $a_0/W = 0.5$, the FE models generally give a good prediction of the crack front, except for the region near free surface or side groove, as shown in Figs. 3.9(a) and (b). This is due to the limitation of the GTN model underestimating the void growth at low stress triaxiality (e.g. $h \leq 0.3$, where h is the stress triaxiality, which will be introduced in Section 3.7) [53, 72]. In general, the 9-point average technique measured crack length match quite well with the experimental results for all cases.

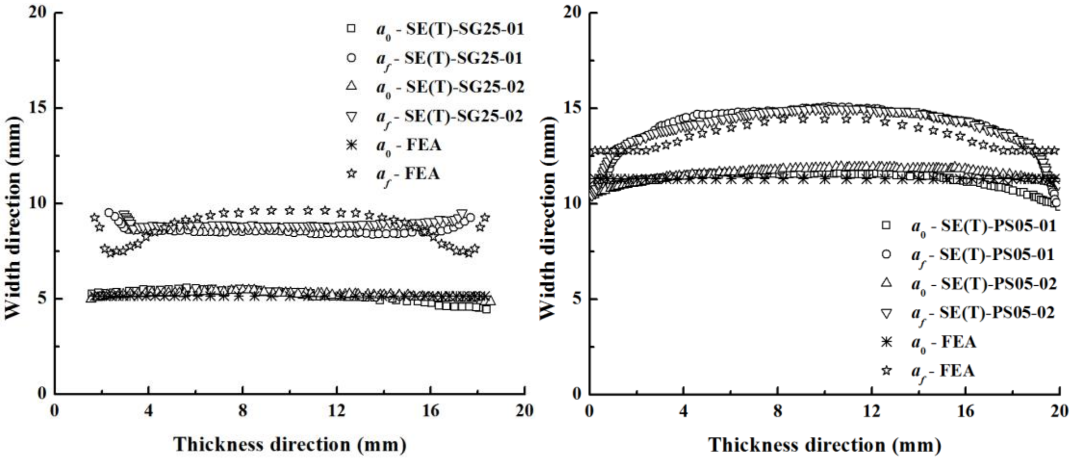

(a) SG specimens with $a_0/W = 0.25$ **(b) PS specimens with $a_0/W = 0.5$**

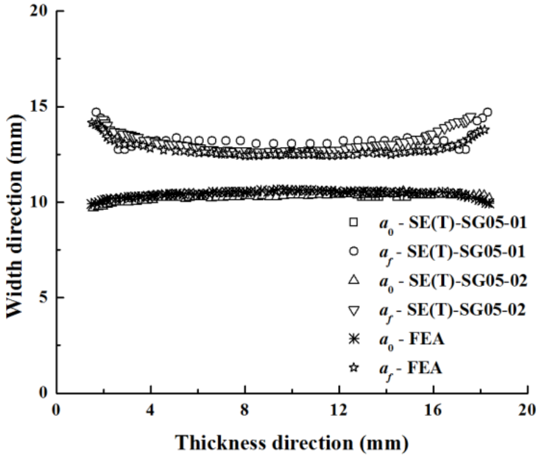

(c) SG specimens with $a_0/W = 0.5$

Fig. 3.9 Comparison of post-test measured and predicted crack front profiles

3.5 Numerical results and initiation toughness J_{IC}

In this section, a total of 21 SE(T) specimens with various geometry configurations (i.e. a_0/W = 0.2, 0.25, 0.3, 0.35, 0.4,0.45 and 0.5 per BSI standard [15], SG for B/W = 1 and PS for B/W = 0.5 and 1), are modelled based on the calibration results in Table 3.2, for the purpose of examining the varying stress-strain fields and constraint parameters over the crack front in a growing crack analysis (see Section 3.6 and 3.7), as well as validating and improving the NM method (see Chapter 4). Note that all SE(T) specimens established in this section have similar geometric configurations as discussed in Section 3.3.1.

Figure 3.10 displays all *P*-CMOD and *J*-*R* curves for 21 SE(T) FE models. As shown in Figs. 3.10(a), (c) and (e), the load-carrying capacity decreases dramatically as the initial crack length increases from 4 mm to 10 mm. Take the PS SE(T) models with B/W = 1 as an example, the maximum load-carrying capacity is about 235 kN for a_0/W = 0.2, whereas reduces to 140 kN for a_0/W = 0.5. On the other hand, it is clearly shown that the specimens with a deeper initial crack yields a lower *J*-*R* curve after crack initiation. This is explained by the in-plane constraint effect that shallow-cracked specimen has lower constraint near the crack tip, which leads to higher fracture toughness. Note that due to the CTOD/2 blunting correction applied to each specimen, the initial portion of the *J*-*R* curves are almost identical as shown in Figs. 3.10(b), (d) and (f).

Numerous studies have been focusing on characterizing the initiation fracture toughness J_{IC} in the past. J_{IC} is the *J*-integral value that marks the beginning stage of material crack growth resistance development. The procedure to determine J_{IC} is standardized in ASTM E1820-17 ANNEXES A8 and A9 [12]. The key point is to construct a 0.2 mm-offset line in accordance with the following equation on the *J*-*R* regression plot:

$$J = 2\sigma_Y \Delta a \tag{3.2}$$

$$\sigma_Y = \frac{\sigma_{YS} + \sigma_{TS}}{2} \tag{3.3}$$

where

σ_Y is the effective yield strength and defined as the average of the ultimate tensile strength σ_{TS} and 0.2%-offset yield strength σ_{YS}.

The intersection of the regression line and the offset line is denoted as J_Q. And J_Q is further qualified as J_{IC}, a size-independent value of fracture toughness if additional requirements in A9.1, A9.9 and A9.10 are all satisfied.

In current study, the initiation fracture toughness J_{IC} can be characterized as the toughness value at the time when the first computational cell element fails due to the void growth and is deleted. The J_{IC} values for all specimens are shown in Fig. 3.11. For comparison, the fracture toughness at crack extension Δa = 1 mm (denoted as J_{1mm}) and Δa = 1.5 mm (denoted as $J_{\text{1.5mm}}$) are also plotted in the figure.

Figure 3.11 shows that J_{IC}, J_{1mm} and $J_{\text{1.5mm}}$ are more or less dependent on initial crack length, and decrease approximately linearly with the increase of a_0/W. The fitted straight-line and corresponding coefficient of determination R^2 are also indicated in the figure. Relatively speaking, J_{1mm} and $J_{\text{1.5mm}}$ are strongly dependent on the constraint, which is consistent with the results in [60, 119]. In contrast, J_{IC} is weakly dependent on a_0/W, which is consistent with the experimental results by Nyhus et al. [120], that the fracture toughness of SE(T) specimen is not sensitive to the initial crack depth. The weak dependence of J_{IC} on initial crack depth can be further explained by the discussion by Xu et al. [60]. In their study, 2D plain strain FEA of SE(T) specimens shows that for small SE(T) specimens (i.e. W = 10 mm), the corresponding Q constraint parameter (see the definition of Q in Section 3.7) are highly negative and do not change significantly with different a_0/W. Thus, the crack-tip constraint is quite low and similar, and therefore the crack depth has a minor effect on the fracture resistance. However, for larger specimens (i.e. W = 30 mm and W = 50 mm), CTOD decreases considerably with the considerable increase of Q. Since the SE(T) specimens modelled in current study are medium-sized (i.e. W = 20 mm), the J_{IC} value does have an non-negligible dependent on crack size, yet very weak.

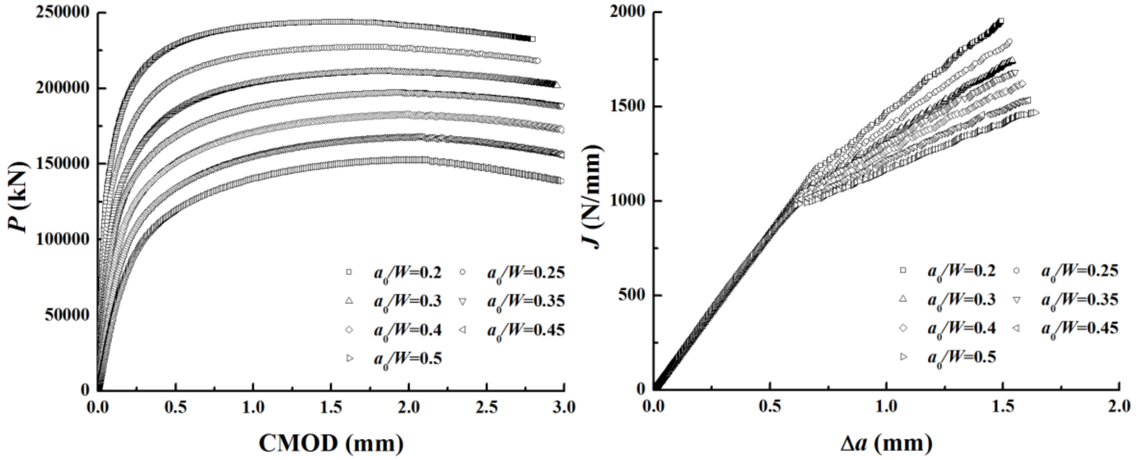

(a) *P*-CMOD curves for PS *B*/*W* = 1 **(b) *J*-*R* curves for PS *B*/*W* = 1**

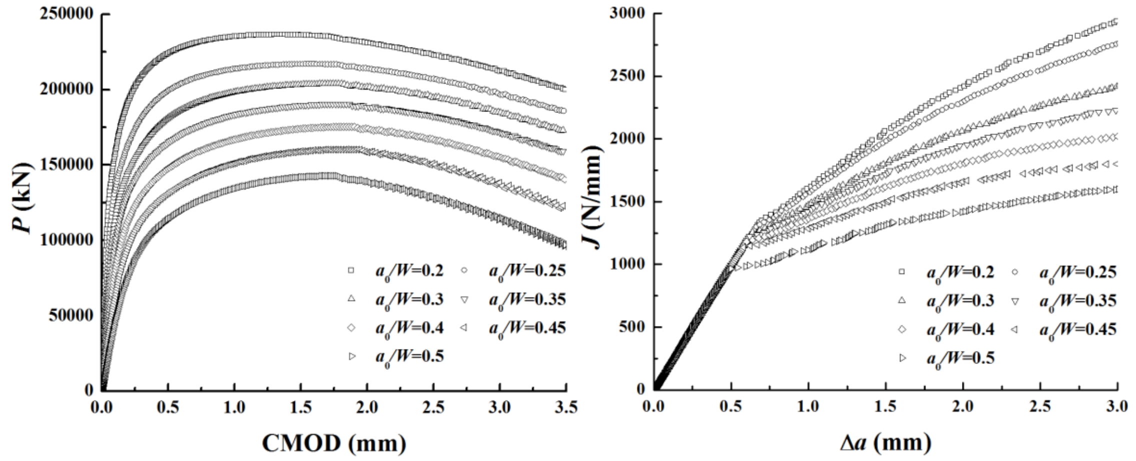

(c) *P*-CMOD curves for SG *B*/*W* = 1 **(d) *J*-*R* curves for SG *B*/*W* = 1**

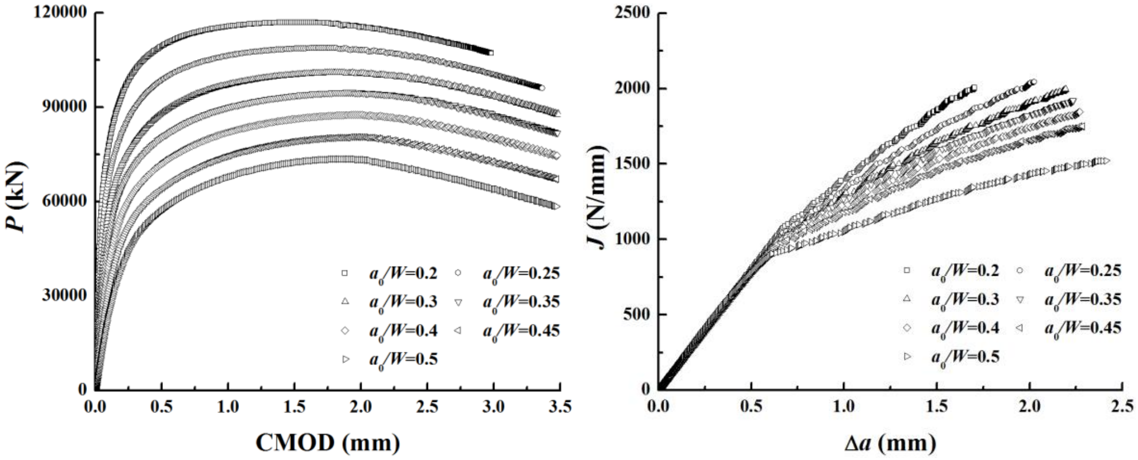

(e) *P*-CMOD curves for PS *B*/*W* = 0.5 **(f) *J*-*R* curves for PS *B*/*W* = 0.5**

Fig. 3.10 *P*-CMOD and *J*-*R* curves for FE models

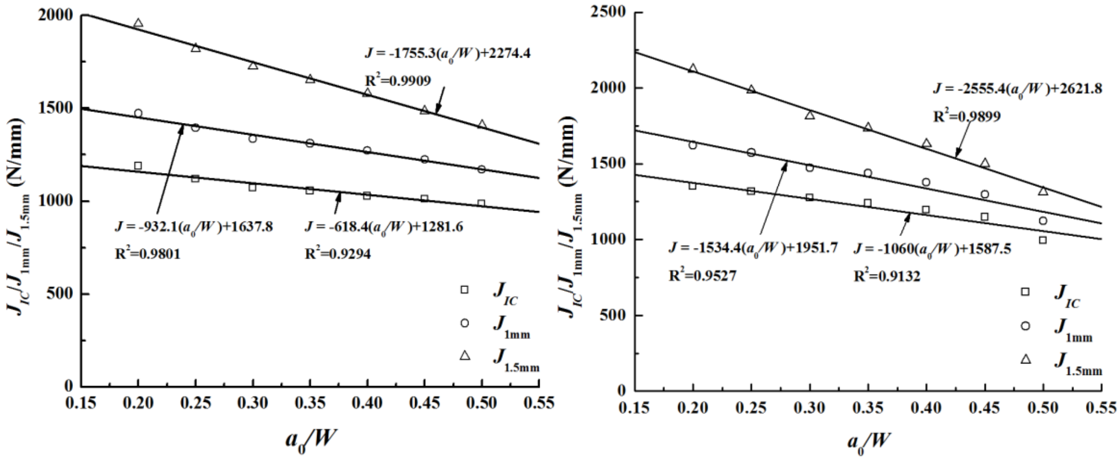

(a) PS models with B/W = 1 **(b) SG models with B/W = 1**

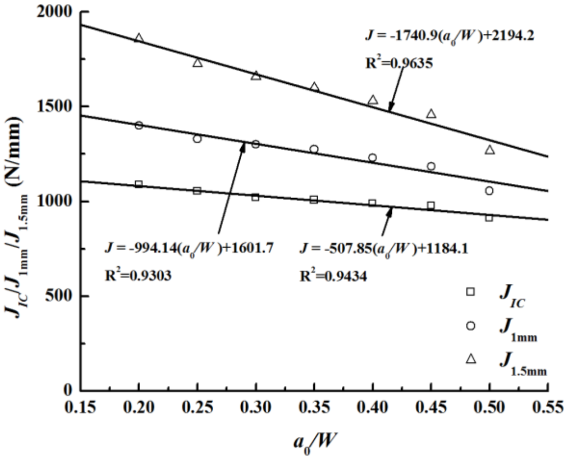

(c) PS models with B/W = 0.5

Fig. 3.11 Variation of fracture toughness (J_{IC} /J_{1mm}/ $J_{1.5mm}$) with a_0/W

3.6 Crack-tip stress fields

3.6.1 Overview

Under evolving stress states, the micro-voids in the steel matrix constantly nucleate, grow and coalescence, and finally lead to ductile fracture. All these three stages are strongly influenced by the state of stress near the crack tip. On the other hand, the constraint effect arises as the loss of the stress triaxiality in the crack front region increases due to LSY. The constraint effect can be interpreted as the ability of deforming plastically under increasing loading level, which is strongly related to the micro-structural features of the material.

In this section, the crack-tip stress fields of the GTN-based FE models described in the previous sections are examined. The investigation is focused on the distributions of the opening stress, $\sigma_{\theta\theta}$, ahead of the crack tip at different crack front locations. Previously, similar work has been conducted by Wang et al. [121], in which stationary-crack analyses were considered, and by Xu et al. [60], in which growing-crack analyses based on the complete Gurson model were considered. However, as far as the author is aware, there is no literature focusing on the comparison of stationary-crack analysis and growing-crack analysis in terms of crack-tip stress fields. To this end, the same FE models are run as stationary models by simply depriving the GTN property of the computational cell elements.

3.6.2 Opening stress distribution

The nodal stress component $\sigma_{\theta\theta}$ along the crack plane (i.e. $\theta = 0°$) is output to examine the stress field. Here the opening stress $\sigma_{\theta\theta}$ is normalized by a reference stress σ_0, which can be taken as the 0.2%-offset yield strength of the material. Figures 3.12 and 3.13 show the distributions of the normalized opening stress $\sigma_{\theta\theta}/\sigma_0$ at the mid-plane ahead of the crack tip at different loading levels (characterized by $J/(b_0\sigma_0)$, note that the initial remaining ligament b_0 is used in both stationary-crack and growing-crack analysis) as a function of the normalized distance from the crack tip (characterized by $r\sigma_0/J$) for PS models with $B/W = 1$, $a_0/W = 0.2$, 0.35 and 0.5, in stationary-crack and growing-crack analysis, respectively. The values of $\sigma_{\theta\theta}/\sigma_0$ obtained by the HRR solutions are also shown in the figures.

From Figs. 3.12 and 3.13, it can be observed that the distribution of $\sigma_{\theta\theta}/\sigma_0$ at the mid-plane ahead of the crack tip is dependent on a_0/W ratio and loading level. For deeply-cracked specimen (i.e. $a_0/W = 0.5$), the distribution of $\sigma_{\theta\theta}/\sigma_0$ is approximately linear for $r\sigma_0/J > 1$ when $J/(b_0\sigma_0) > 0.174$. This is due to the strong bending effect caused by the eccentricity between the applied load and centroid of the remaining ligament, on the crack-tip field. As a_0/W decreases from 0.5 to 0.2, the bending effect on $\sigma_{\theta\theta}/\sigma_0$ becomes less pronounced, suggesting that the deeply-cracked SE(T) specimen behaves similarly as bend-type specimens [122].

As for growing-crack analysis, the instantaneous crack extension is indicated in Figs. 3.13(a), (b) and (c). Note that the crack extension includes blunting and actual crack extension. Since at lower loading levels (i.e. $J/b\sigma_0$ = 0.060 and 0.113), the crack initiation has not yet started, the distribution of $\sigma_{\theta\theta}/\sigma_0$ in the stationary-crack and growing-crack analysis are almost identical. At the loading level of $J/b\sigma_0$ = 0.174, crack initiation has started, which resulted in that $\sigma_{\theta\theta}/\sigma_0$ in growing-crack analysis distributes slightly lower than that in stationary-crack analysis.

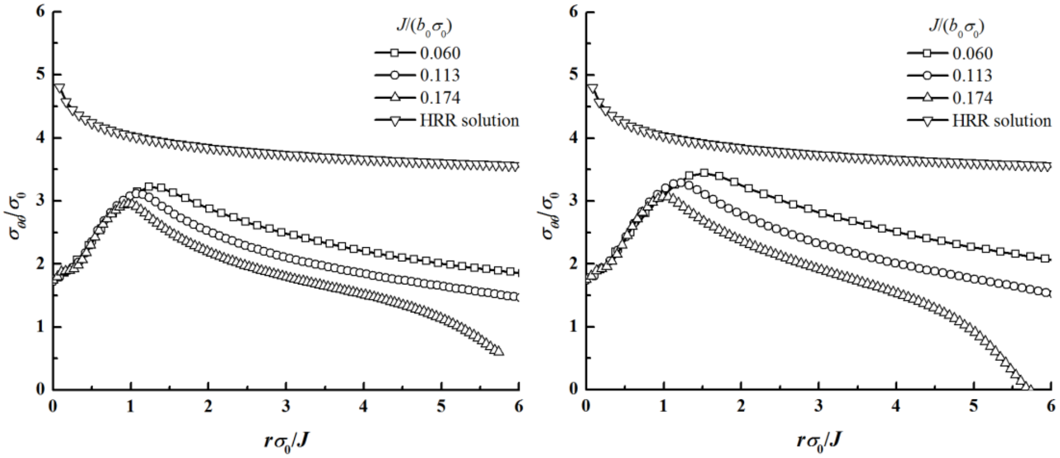

(a) a_0/W = 0.2 **(b) a_0/W = 0.35**

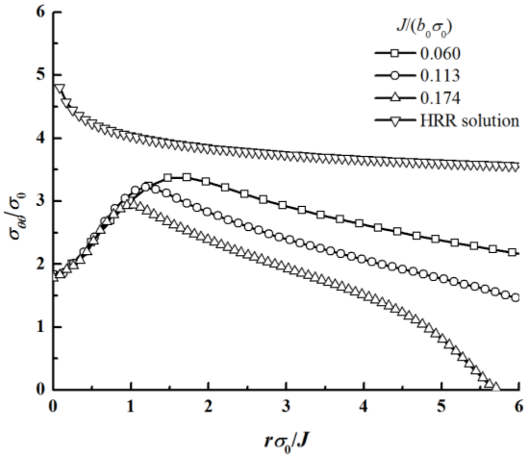

(c) a_0/W = 0.5

Fig. 3.12 Distribution of $\sigma_{\theta\theta}/\sigma_0$ versus distance from initial crack tip at the mid-plane in stationary-crack analysis (PS, B/W = 1, a_0/W = 0.2, 0.35 and 0.5)

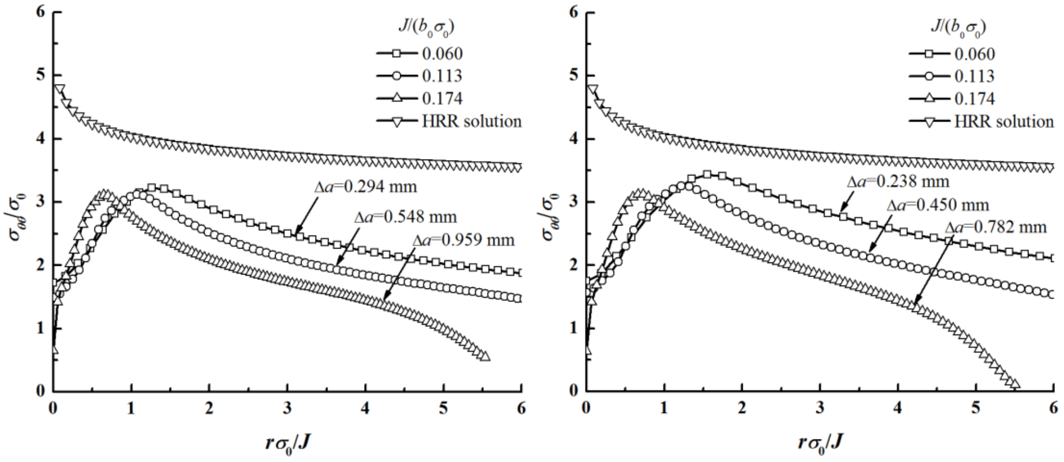

(a) a_0/W = 0.2 **(b) a_0/W = 0.35**

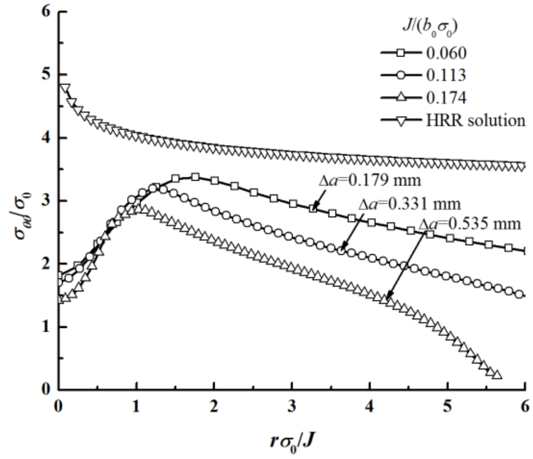

(c) a_0/W = 0.5

Fig. 3.13 Distribution of $\sigma_{\theta\theta}/\sigma_0$ versus distance from instantaneous crack tip at the mid-plane in growing-crack analysis (PS, B/W = 1, a_0/W = 0.2, 0.35 and 0.5)

Figure 3.14 shows the distributions of $\sigma_{\theta\theta}/\sigma_0$ ahead of the crack tip for the PS SE(T) model with $B/W = 1$ and $a_0/W = 0.2$ at five different crack front locations in the thickness direction (characterized by $2z/B$, with $z = 0$ representing mid-plane and $z = B/2$ representing free surface) at different loading levels in stationary-crack analysis. It is indicated that $\sigma_{\theta\theta}/\sigma_0$ decreases from the mid-plane to free surface at a certain given loading level. Due to the increase in the size of the crack-tip plastic zone and presence of the diffuse necking near the free surface, $\sigma_{\theta\theta}/\sigma_0$ at $2z/B = 1$ is markedly lower than those at $2z/B = 0$, 0.398, 0.675 and 0.867 [121]. At a given through-thickness location that is not too close to the free surface (e.g. $0 \leq 2z/B \leq 0.867$) and a given normalized crack-tip distance (e.g. $1 \leq r\sigma_0/J \leq 5$), $\sigma_{\theta\theta}/\sigma_0$ decreases with the increase of the applied load. At regions close to the free surface, $\sigma_{\theta\theta}/\sigma_0$ distributes uniformly along most part of the remaining ligament. Figure 3.14 suggests that there is little difference between the $\sigma_{\theta\theta}/\sigma_0$ distributions corresponding to the stationary-crack and growing-crack analyses.

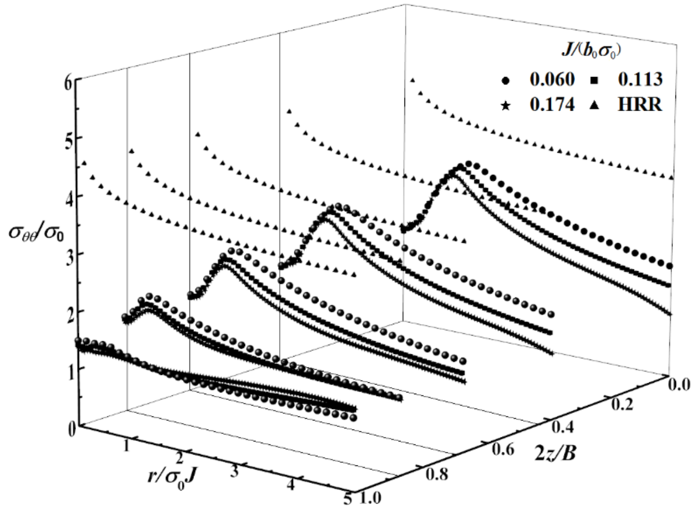

(a) Stationary-crack analysis

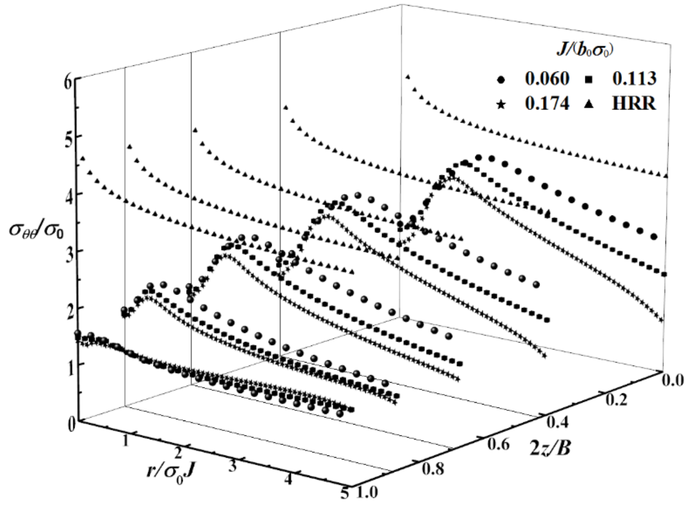

(b) Growing-crack analysis

Fig. 3.14 Distribution of $\sigma_{\theta\theta}/\sigma_0$ in the crack plane (PS, $a_0/W = 0.2$, $B/W = 1$)

Figure 3.15 shows the distribution of $\sigma_{\theta\theta}/\sigma_0$ at $r\sigma_0/J = 2$ for PS models with $a_0/W = 0.2$, 0.35 and 0.5, at different loading levels in stationary-crack and growing-crack analysis. It is indicated that $\sigma_{\theta\theta}/\sigma_0$ at the mid-plane is the maximum value along the crack front and gradually decreases from mid-plane to free surface. Also, the distribution of $\sigma_{\theta\theta}/\sigma_0$ is dependent on a_0/W ratio. With a smaller a_0/W ratio, the opening stress is lower than that of a larger a_0/W ratio throughout the entire thickness direction. In addition, as the loading level increases, $\sigma_{\theta\theta}/\sigma_0$ becomes smaller. Figure 3.15 suggests that the distribution of $\sigma_{\theta\theta}/\sigma_0$ along the crack front for the station-crack analysis is similar to that for the growing-crack analysis.

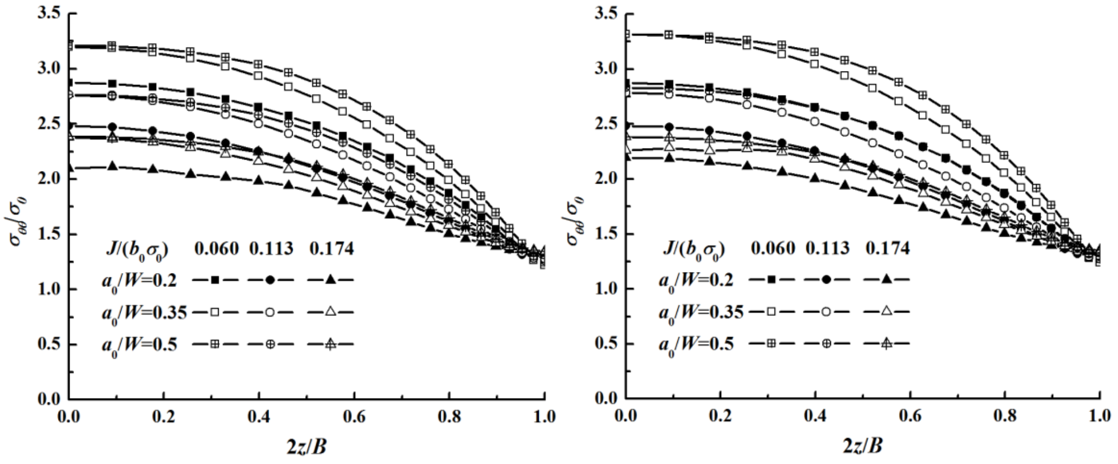

(a) Stationary-crack analysis **(b) Growing-crack analysis**

Fig. 3.15 Distribution of $\sigma_{\theta\theta}/\sigma_0$ at $r\sigma_0/J = 2$ along the crack front for PS specimens

3.7 Crack-tip constraint parameters

3.7.1 Overview

As introduced in Chapter 1, the fracture toughness transferability issue is highly related to the constraint effect, and can be addressed by investigating the crack-tip stress field and the crack-tip constraint level characterized by constraint parameters. Therefore, detailed examinations of the crack-tip constraint parameters using the stationary-crack and GTN-based growing-crack FE models are presented in this section. The constraint parameters considered are Q [18, 19], A_2 [20, 21], h [22], and T_Z [23-25].

The Q parameter is defined as the normalized difference between the crack-tip stress field and HRR solution:

$$\sigma_{ij} = \left(\sigma_{ij}\right)_{HRR} + Q\sigma_0\delta_{ij} \quad \text{at} \ \ r > \frac{J}{\sigma_0} \quad |\theta| < \frac{\pi}{2} \tag{3.4}$$

where

δ_{ij} is the Kronecker delta.

For stationary-crack analysis, the Q parameter is evaluated from the crack opening stress at $\theta = 0°$ and a specific distance from the crack tip (i.e. $r = 2J/\sigma_0$), while for the growing crack analysis, the Q parameter is evaluated from the crack opening stress at $\theta = 0°$ and a specific distance from the instantaneous crack tip (i.e. also $r = 2J/\sigma_0$). This also applies to A_2, h and T_z parameters.

The A_2 parameter is evaluated as the value of smaller root of the following quadratic equation with respect to A_2:

$$\frac{\sigma_{ij}}{\sigma_0} = A_1\left[\left(\frac{r}{l}\right)^{s_1}\tilde{\sigma}_{ij}^{(1)}(\theta,n) + A_2\left(\frac{r}{l}\right)^{s_2}\tilde{\sigma}_{ij}^{(2)}(\theta,n) + A_2^2\left(\frac{r}{l}\right)^{s_3}\tilde{\sigma}_{ij}^{(3)}(\theta,n)\right] \tag{3.5}$$

$$A_1 = \left(\frac{J}{\alpha\varepsilon_0\sigma_0 I_n l}\right)^{-s_1} \tag{3.6}$$

$$s_1 = -\frac{1}{n+1} \tag{3.7}$$

where

A_1 is the amplitude factor from the HRR stress field;

l is a characteristic length parameter which can be simply set as 1 mm;

The angular functions ${\tilde{\sigma}_{ij}}^{(k)}$ (k = 1, 2 and 3) and the stress power exponents s_1, s_2 and s_3 are functions of the hardening exponent $n_{R\text{-}O}$. The values of ${\tilde{\sigma}_{ij}}^{(k)}$, s_1, s_2 and s_3 corresponding to the plane strain and plane stress conditions are tabulated in [123]. Since the plane strain condition prevail through the thickness direction of the fracture specimens, in current study, the above-mentioned values correspond to the plane strain condition.

The parameter h is the stress triaxiality defined as the ratio of hydrostatic stress to von Mises stress:

$$h = \frac{\sigma_m}{\sigma_e} \tag{3.8}$$

The parameter T_Z is defined as the ratio of the out-of-plane normal stress to sum of the in-plane normal stresses:

$$T_Z = \frac{\sigma_{zz}}{\sigma_{xx} + \sigma_{yy}} \tag{3.9}$$

3.7.2 Constraint distribution ahead of the crack tip

Figures 3.16 to 3.19 show the distributions of Q, A_2, h and T_Z at $0 < r/(J/\sigma_0) < 5$ at the mid-plane of PS model with a_0/W = 0.2, 0.35 and 0.5, B/W = 1 at different loading levels, for stationary-crack and growing-crack analysis. Figures 3.16, 3.18 and 3.19 indicate that Q, h and T_Z parameters decreases markedly as the loading level and/or r increases. Figure 3.17 shows that A_2 parameter is almost independent of the loading level and r. These observations are consistent with the results reported in previous studies [124]. Note that the distributions of Q, A_2, h and T_Z at $0 < r/(J/\sigma_0) < 5$ at the mid-plane of SG specimens are almost identical to those of PS specimens, hence are not shown for brevity.

Figures 3.16, 3.18 and 3.19 also indicate that for the loading level of $J/(b\sigma_0) < 0.113$, the constraint parameters Q, h and T_z in stationary-crack and growing-crack analysis distribute almost identically along the mid-plane. Under the loading level of $J/(b\sigma_0) > 0.113$, the distributions of the constraint parameters start to present some deviations, especially for shallow-cracked specimens.

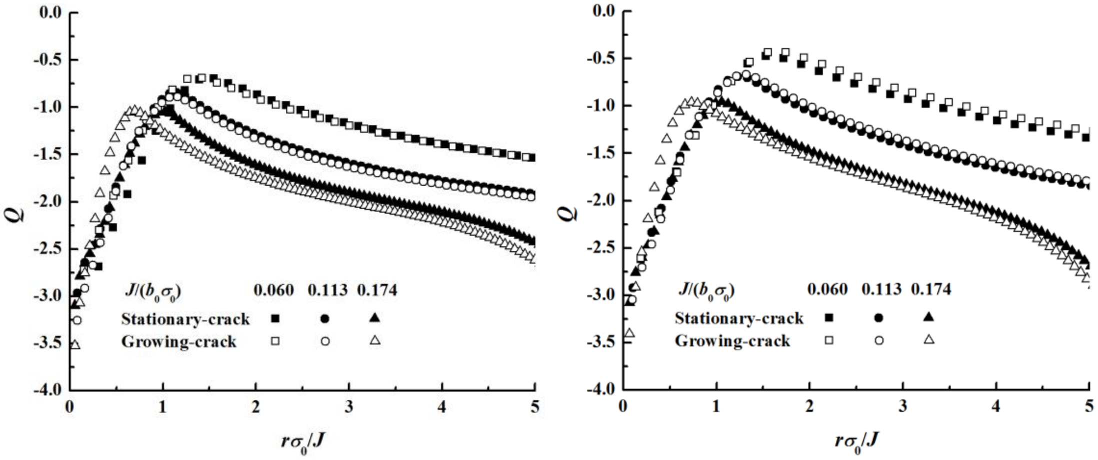

(a) a_0/W = 0.2 **(b) a_0/W = 0.35**

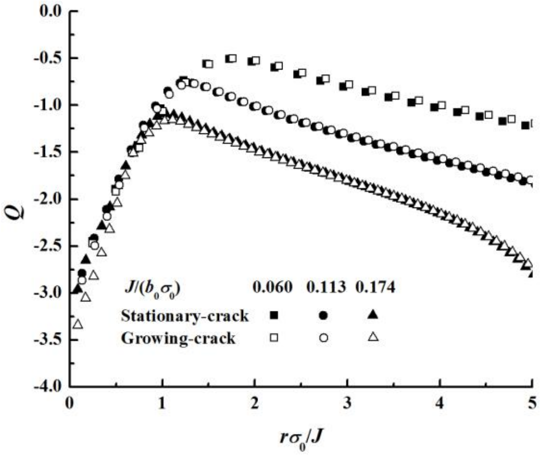

(c) a_0/W = 0.5

Fig. 3.16 Distribution of Q in the mid-plane for PS model (a_0/W = 0.2, 0.35 and 0.5, B/W = 1) at different loading levels (stationary-crack and growing-crack analyses)

Another observation from Figs. 3.16 to 3.19 is that, as the initial crack length a_0/W ratio increases from 0.2 to 0.5, the decrease in constraint parameters with the increasing loading level becomes more pronounced, which means that the distribution of the constraint parameters by the loading level is influenced by the initial crack length, for both stationary-crack and growing-crack analysis.

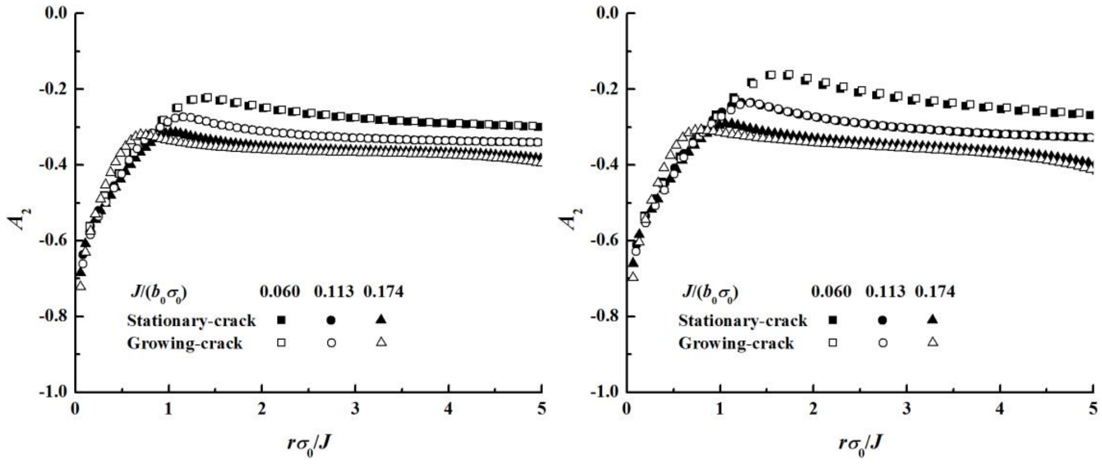

(a) $a_0/W = 0.2$ **(b) $a_0/W = 0.35$**

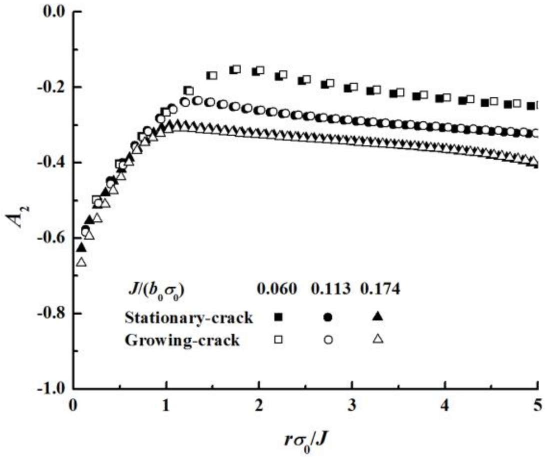

(c) $a_0/W = 0.5$

Fig. 3.17 Distribution of A_2 in the mid-plane for PS model (a_0/W = 0.2, 0.35 and 0.5, B/W = 1) at different loading levels (stationary-crack and growing-crack analyses)

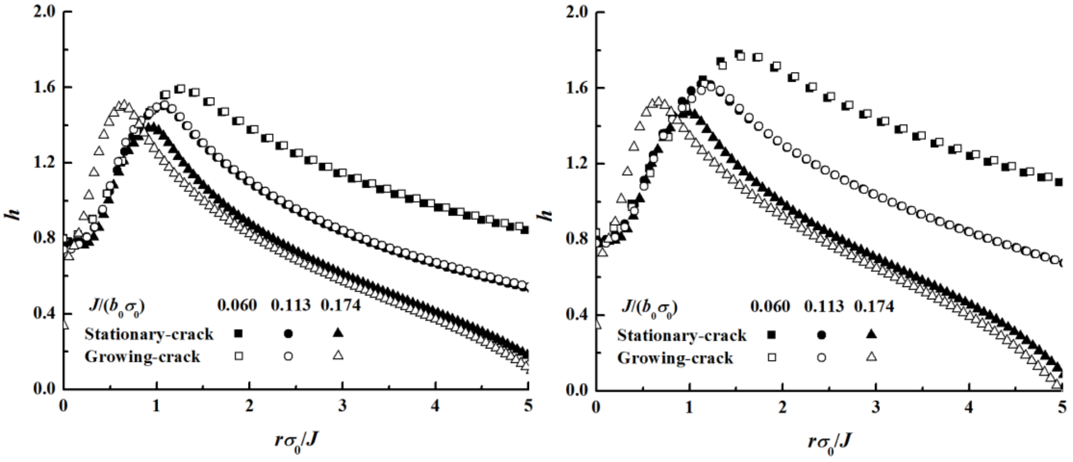

(a) $a_0/W = 0.2$ (b) $a_0/W = 0.35$

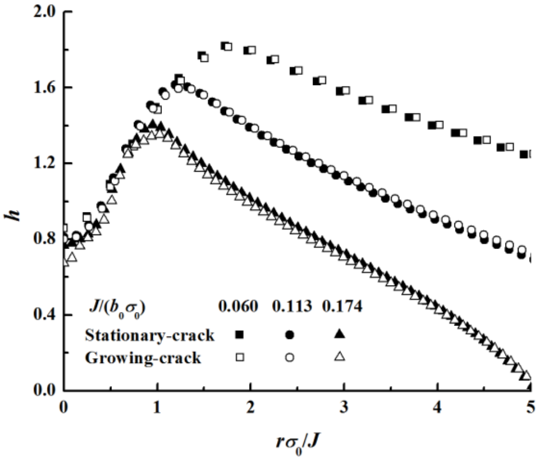

(c) $a_0/W = 0.5$

Fig. 3.18 Distribution of h in the mid-plane for PS model (a_0/W = 0.2, 0.35 and 0.5, B/W = 1) at different loading levels (stationary-crack and growing-crack analyses)

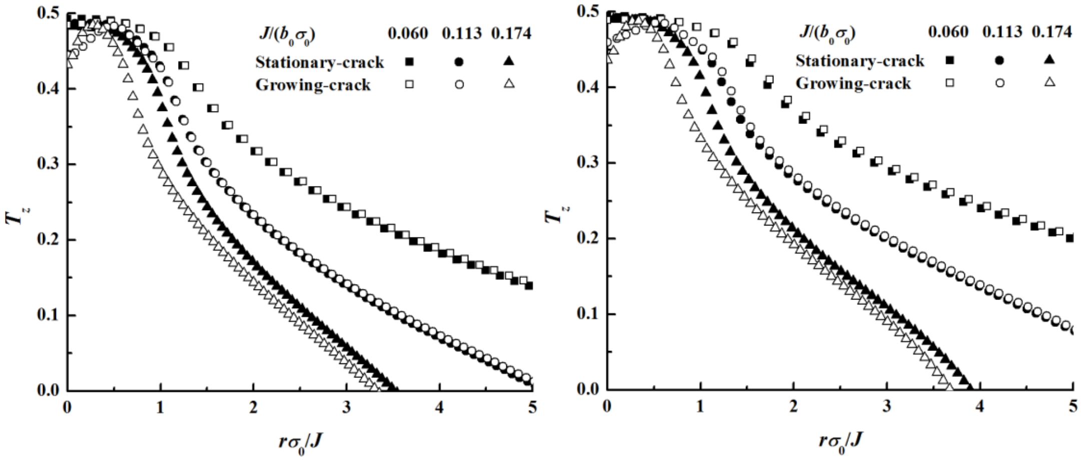

(a) a_0/W = 0.2 **(b) a_0/W = 0.35**

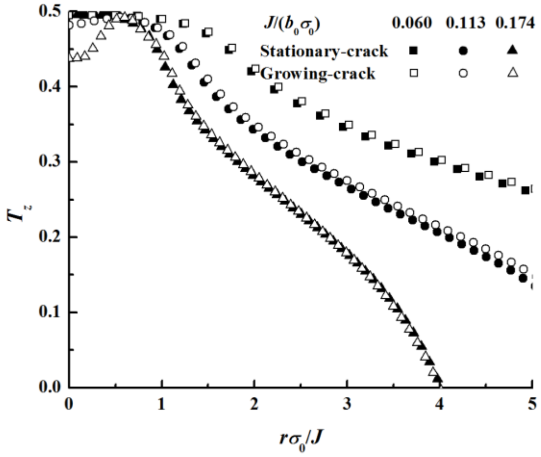

(c) a_0/W = 0.5

Fig. 3.19 Distribution of T_z in the mid-plane for PS model (a_0/W = 0.2, 0.35 and 0.5, B/W = 1) at different loading levels (stationary-crack and growing-crack analyses)

3.7.3 Through-thickness constraint distribution

i). Q parameter:

Figure 3.20 shows the through-thickness distribution of Q at different loading levels for PS specimens with a_0/W = 0.2, 0.35 and 0.5 and B/W = 1, where Q is evaluated at a normalized distance of $r/(J/\sigma_0) = 2$ away from the crack tip. Note that in stationary-crack analysis, the crack tip is the original one, whereas in growing-crack analysis, the crack tip is the instantaneous one. It is shown that as loading level increases, the constraint parameters at a given crack front location decreases markedly. At a certain loading level, as a_0/W increases, the corresponding Q parameter at the same given crack front location increases, which can be interpreted by the in-plane constraint effect.

The above-mentioned constraint effect is more clearly shown in Fig. 3.21, in which the Q parameter at the mid-plane of PS models with a_0/W = 0.2-0.5 and B/W = 1 are plotted against a_0/W.

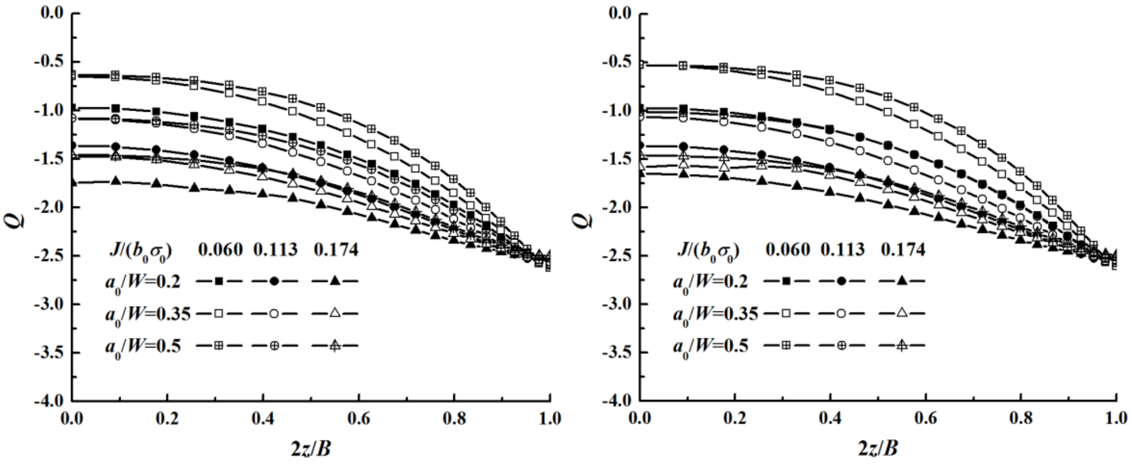

(a) Stationary-crack analysis **(b) Growing-crack analysis**

Fig. 3.20 Through-thickness distribution of *Q* for PS models

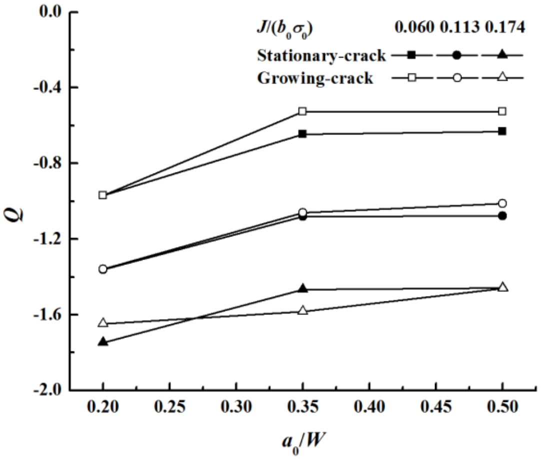

Fig. 3.21 Variation of *Q* parameter at mid-plane with a_0/W (PS, *B*/*W* = 1)

ii). A_2 parameter:

Figure 3.22 shows the through-thickness distribution of A_2 at different loading levels for the PS specimens with $a_0/W = 0.2$, 0.35 and 0.5; $B/W = 1$, where A_2 is evaluated at $r/(J/\sigma_0) = 2$. The figure indicates that A_2 is almost independent of the loading level and r. The figure also shows that for a given loading level, A_2 does not change much with a_0/W ratio. This may be due to that the currently considered loading levels are all high (i.e. $1.1 < P/P_Y < 1.3$). Figure 3.23 shows that the value of A_2 slightly increases with the increase of a_0/W, which is consistent with the results reported in [124].

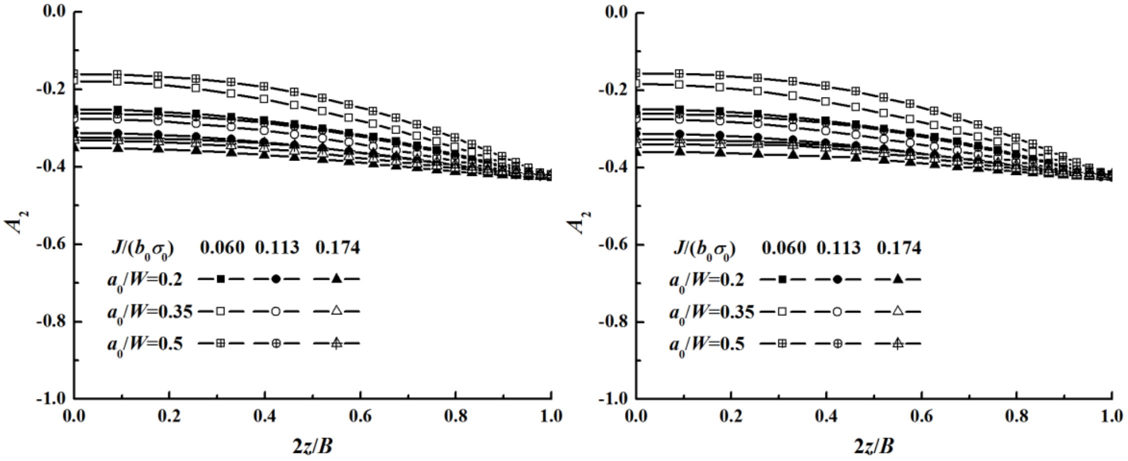

(a) Stationary-crack analysis **(b) Growing-crack analysis**

Fig. 3.22 Through-thickness distribution of A_2 for PS models

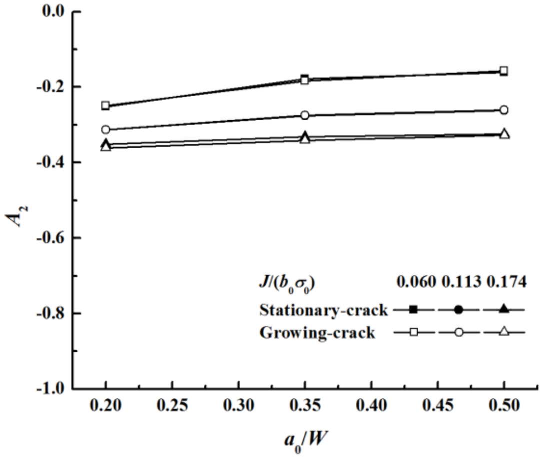

Fig. 3.23 Variation of A_2 parameter at mid-plane with a_0/W (PS, $B/W = 1$)

iii). *h* parameter:

Figure 3.24 shows the through-thickness distribution of *h* at different loading levels for PS specimens with $a_0/W = 0.2$, 0.35 and 0.5 and $B/W = 1$, where *h* is evaluated at a normalized distance of $r/(J/\sigma_0) = 2$ away from the crack tip. Similar to the *Q* parameter, *h* decreases markedly as loading level increases. Figure 3.25 indicates that the growing-crack analysis at lower loading levels (i.e. $J/b\sigma_0 = 0.060$ and 0.113) presents slightly stronger in-plane constraint effect.

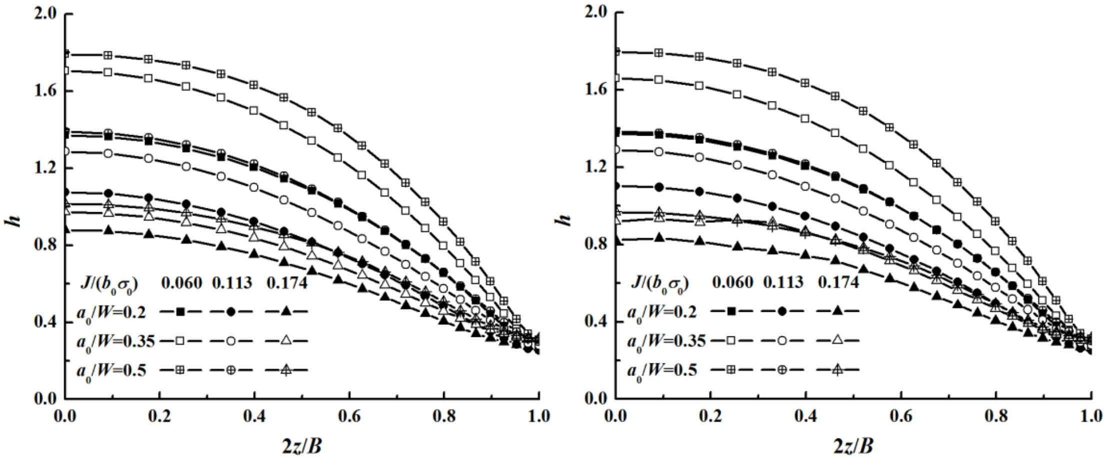

(a) Stationary-crack analysis **(b) Growing-crack analysis**

Fig. 3.24 Through-thickness distribution of *h* for PS models

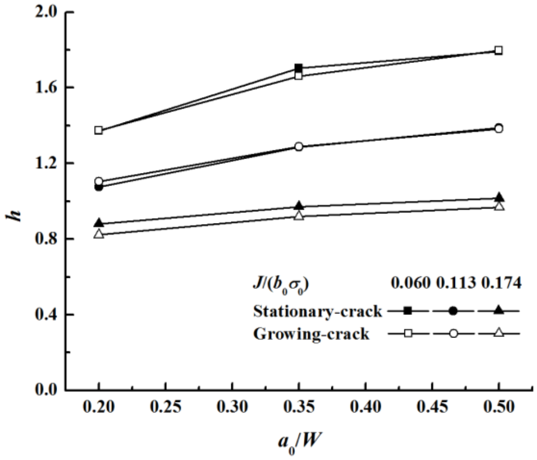

Fig. 3.25 Variation of *h* parameter at mid-plane with a_0/W (PS, $B/W = 1$)

iv). T_Z parameter:

Figure 3.26 shows the through-thickness distribution of T_z at different loading levels for PS specimens with a_0/W = 0.2, 0.35 and 0.5 and B/W = 1, where T_z is evaluated at a normalized distance of $r/(J/\sigma_0) = 2$ away from the crack tip. It is shown that T_Z decreases markedly as loading level increases, especially for shallow-cracked specimens. As shown in Fig. 3.27, under higher loading level (i.e. $J/b\sigma_0 = 0.174$), a visible deviation of T_z at the mid-plane in stationary-crack and growing-crack analysis is captured, especially for shallow-cracked specimen with a_0/W = 0.2.

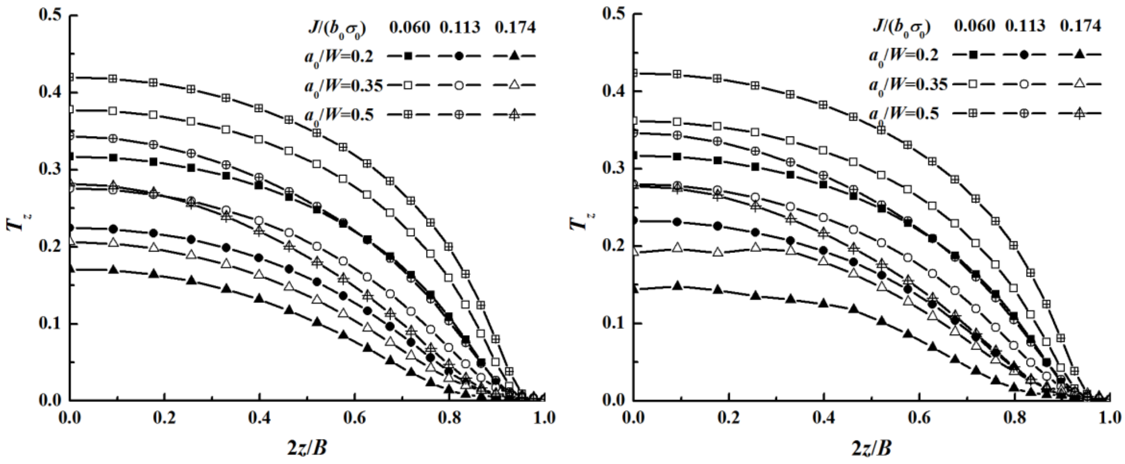

(a) Stationary-crack analysis **(b) Growing-crack analysis**

Fig. 3.26 Through-thickness distribution of T_z for PS models

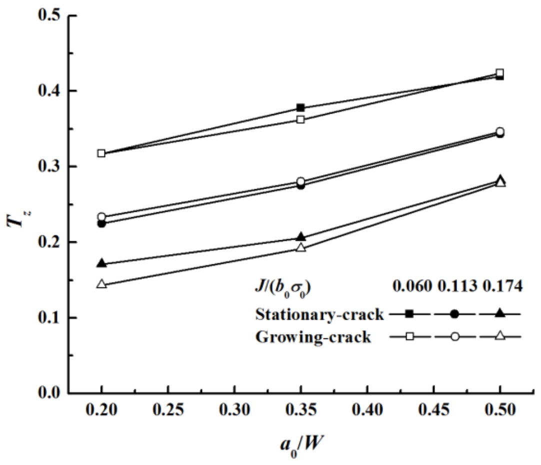

Fig. 3.27 Variation of T_z parameter at mid-plane with a_0/W (PS, B/W = 1)

3.7.4 Relation between constraint parameters

The relations between constraint parameters are examined in this section. The parameters are all evaluated at the mid-plane from the crack tip at three different loading levels. The FE models considered have an initial crack length of a_0/W = 0.2 and B/W = 1 in both stationary-crack and growing-crack analyses. Figure 3.28 to 3.31 depict the relations between Q-h, Q-T_Z, A_2-h and A_2-T_Z, respectively.

Figure 3.28 indicates that Q and h parameters are well correlated for SE(T) models in both stationary-crack and growing-crack analyses in terms of characterizing the crack-tip constraint. As can be observed in the figure, for each curve, as the distance from the crack tip $r/(J/\sigma_0)$ increases from 0 to a certain value, an inflection point forms. Take the case of the stationary-crack model at a loading level of $J/(b\sigma_0)$ = 0.060 as an example, as the distance from the crack tip increases, the Q and h parameters are correlated almost linearly. When $r/(J/\sigma_0)$ reaches 1.02, an inflection point forms and another linear correlation presents. In this study, the distance at the inflection point is named as 'inflection point distance'. Another observation is that the 'inflection point distance' decreases as loading level increases. In addition, it is observed that the 'inflection point distance' in growing-crack analysis is markedly smaller than that in stationary-crack analysis for the high loading level of $J/(b\sigma_0)$ = 0.174. Note that the above-mentioned observations also apply to FE models with other a_0/W ratios.

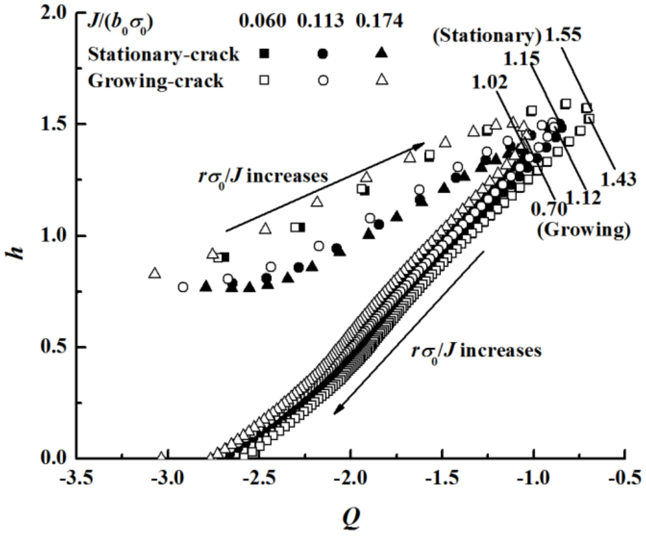

Fig. 3.28 Relation between *Q*-*h*

Figure 3.29 shows the relation between Q and T_Z parameters. Similar to the Q-h relation, the inflection points characterized by certain distances $r/(J/\sigma_0)$ from the crack tip are captured at different loading levels in both stationary-crack and growing-crack analyses. The T_Z parameter is essentially independent of the Q parameter near the crack-tip region. As the inflection point distance reaches a certain value, T_Z becomes correlated to Q, and this correlation first becomes stronger and then weaker as the distance $r/(J/\sigma_0)$ increases.

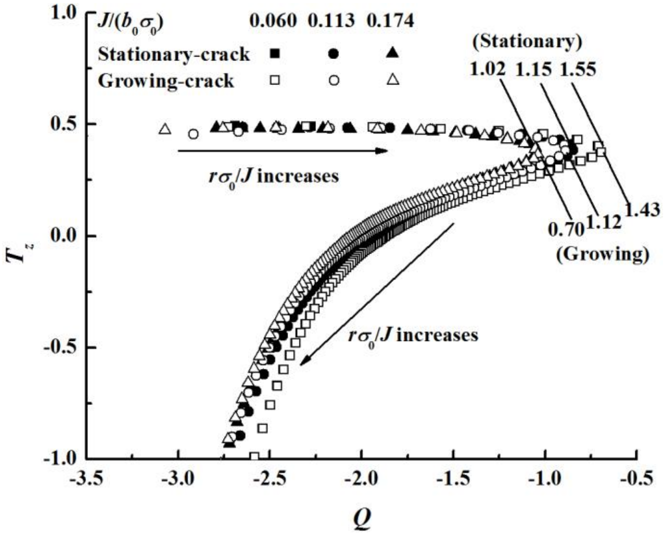

Fig. 3.29 Relation between Q-T_Z

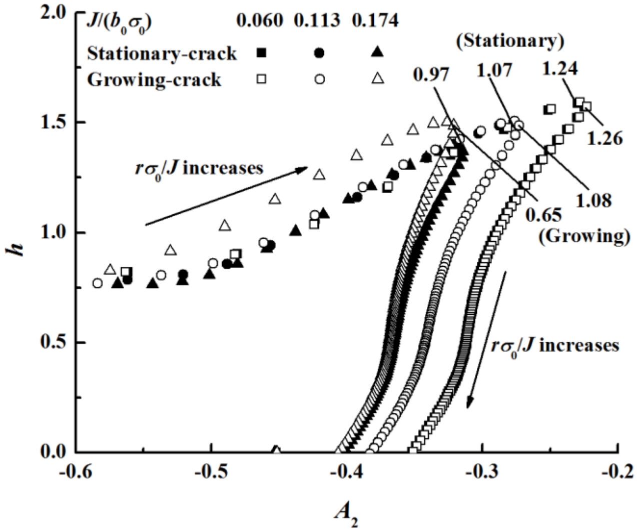

Fig. 3.30 Relation between A_2-h

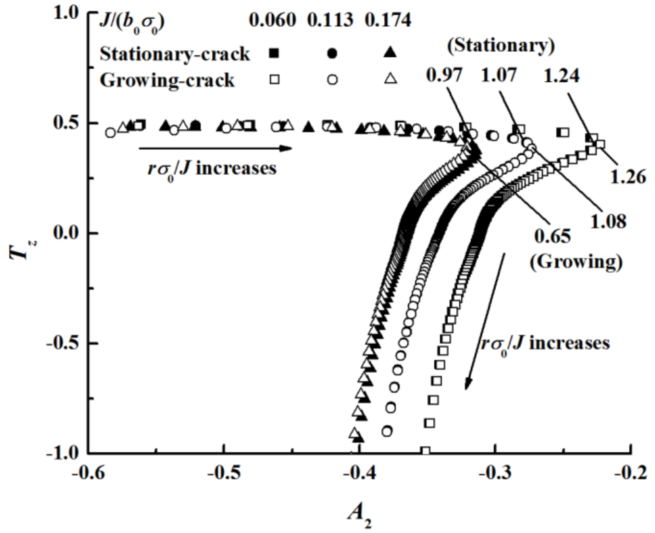

Fig. 3.31 Relation between A_2-T_Z

Figures 3.30 and 3.31 show the relations between A_2-h as well as A_2-T_Z, respectively. Similar to the Q-h and Q-T_Z relations, inflection points are captured at different loading levels in both stationary-crack and growing-crack analyses. In Fig. 3.30, as the distance from the crack tip increases, the A_2 and h parameters are correlated almost linearly. Before $r/(J/\sigma_0)$ reaches a certain value, the A_2-h relation are almost linear, and after that certain value, these two constraint parameters present a new correlation. Figure 3.31 shows the relation between A_2 and T_Z parameters. Similar to the Q-T_Z relation, inflection points are captured at different loading levels in both stationary-crack and growing-crack analyses. The T_Z parameter is essentially independent on A_2 parameter near the crack-tip region. As the distance $r/(J/\sigma_0)$ becomes greater than the inflection point distance, the T_Z parameter becomes almost linearly correlated to the A_2 parameter, especially for lower loading level.

Chapter 4 Normalization method for SE(T) specimen

4.1 Overview

The normalization (NM) method (also known as the normalization data reduction technique) is standardized in ASTM E1820-17 [12] as an alternative method to develop the *J-R* curves for deeply-cracked (i.e. $0.45 \leq a_0/W \leq 0.70$) SE(B) and C(T) specimens for testing cases where the unloading compliance method becomes unfeasible or impractical (e.g. tests involving high loading rates, extreme temperatures or aggressive environments). The NM method does not require measurements of the crack growth during the *J-R* curve testing. It only requires recording the load-displacement history (i.e. *P*-LLD or *P*-CMOD curve), initial crack length (a_0) and finial crack length (a_f) [125]. The crack growth path from a_0 to a_f is inferred iteratively by forcing the normalized load, normalized plastic displacement, and crack length to be on a fitted normalized calibration curve for a given specimen after the test has been completed.

As describe in Section 4.2, the NM method as standardized in ASTM E1820-17 [12] involves somewhat tedious computation of the *J*-integral. The research reported in this chapter is aimed at improving the computational efficiency of the NM method with respect to its application to the *J-R* curve evaluation for the SE(T) specimen. To this end, a so-called *k* factor-based NM method is developed, in which the *J* value is directly evaluated using the *k* factor. In the following sections, a review of the NM method is first presented followed by the description of the development of the *k* factor method.

4.2 Review of NM method

4.2.1 Procedure of NM method

The procedure of NM method for SE(B) or C(T) specimens has been standardized in ASTM E1820-17 [12] and is summarized as follows.

1) During the toughness testing of the fracture specimen, a load-CMOD curve should be recorded (see Fig. 4.1 for an illustration), together with the initial and final crack length

(i.e. a_0 and a_f) measured using the 9-point average technique as specified in ASTM E1820-17 [12] by breaking up the specimen after the completion of the test.

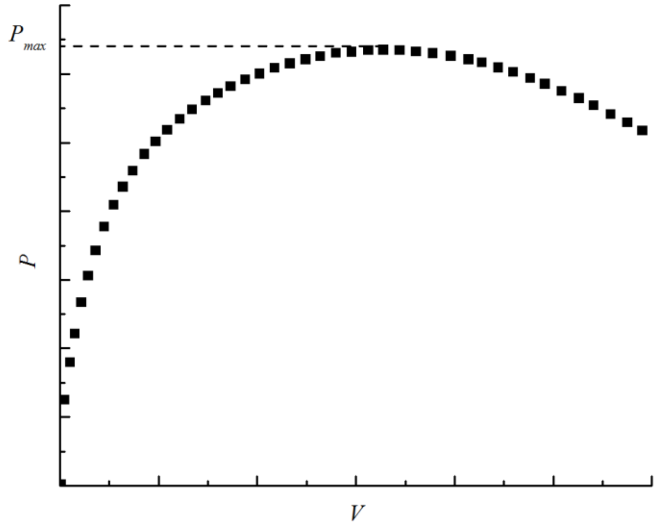

Fig. 4.1 Load-CMOD curve

2) Each load point P_i up to, but excluding the maximum load P_{max}, on the load-CMOD curve is normalized using the following equation:

$$P_{Ni} = \frac{P_i}{BW\left(1 - \frac{a_{bi}}{W}\right)^{\eta_{pl}}} \tag{4.1}$$

where

P_{Ni} is the normalized load at the i-th loading step ($i = 1, 2, \ldots$) (note that P_{Ni} has the same unit as stress);

η_{pl} is the so-called plastic eta factor, which relates the plastic area under the load-CMOD curve to J and is typically a function of the crack length [126]. The equations for evaluating η_{pl} for SE(B) and C(T) specimens are specified in ASTM E1820-17 [12].

a_{bi} is the blunting corrected crack length at the i-th loading step and given by:

$$a_{bi} = a_0 + \frac{J_i}{2\sigma_Y} \tag{4.2}$$

with J_i being the J-integral at the i-th loading step and calculated from:

$$J_i = \frac{K_i^2(1-\nu^2)}{E} + J_{pli} \tag{4.3}$$

where

K_i is the stress intensity factor at the i-th loading step;

J_{pli} is the plastic component of J_i and can be calculated using the following equation:

$$J_{pli} = \left[J_{pl(i-1)} + \left(\frac{\eta_{pl(i-1)}}{b_{(i-1)}}\right)\left(\frac{A_{pli} - A_{pl(i-1)}}{B_N}\right)\right]\left[1 - \frac{\gamma_{LLD(i-1)}\left(a_i - a_{(i-1)}\right)}{b_{(i-1)}}\right] \tag{4.4}$$

in which

γ_{LLD} is a plastic parameter and typically a function of the crack length [127]. Since the crack length a_i (i = 1, 2, …) is unknown at this step, the values of K_i, J_{pli} and η_{pl} are calculated using the initial crack size a_0.

3) The plastic component of CMOD (normalized by W) at the i-th step, V_{pli}/W, is obtained by:

$$\frac{V_{pli}}{W} = \frac{V_i - P_iC_i}{W} \tag{4.5}$$

where

C_i is the CMOD-based compliance of the test specimen, which is a function of the crack length [128]. At this step, the blunting corrected crack size a_{bi} as given by Eq. (4.2) is used to estimate C_i.

4) The load and CMOD corresponding to the last point on the load-CMOD curve are normalized using Eqs. (4.1) and (4.5), respectively, except that a_f (without blunting correction) is used in Eq. (4.1) and to evaluate the compliance of the specimen. Figure 4.2 illustrates the final normalized load-CMOD curve, whereby the final point markedly differs from the rest of the curve because of the normalization based on a_f.

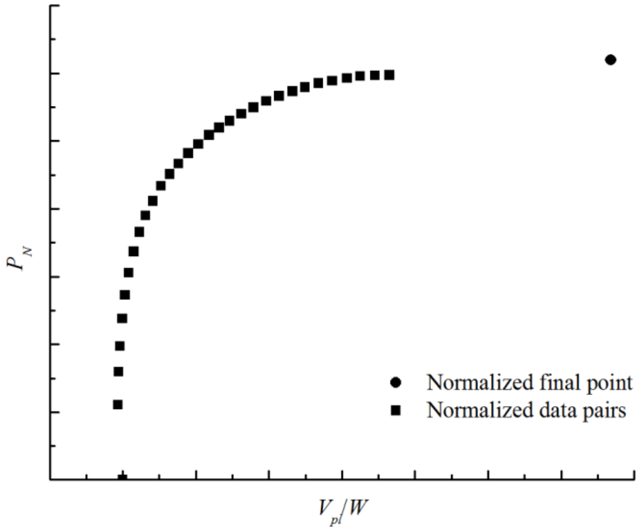

Fig. 4.2 Normalized load versus normalized CMOD

5) The normalized load-CMOD pairs (P_{Ni}, V_{pli}/W) with $V_{pli}/W > 0.001$ up to, but excluding the maximum load, as well as the final normalized pair, are fitted by using the following so-called 'NM function' (see Fig. 4.3 for an illustration):

$$P_N = \frac{L + M \cdot \left(\frac{V_{pl}}{W}\right) + N \cdot \left(\frac{V_{pl}}{W}\right)^2}{O + \left(\frac{V_{pl}}{W}\right)} \tag{4.6}$$

where

L, M, N, and O are fitting coefficients to be determined, e.g. using the least squares technique.

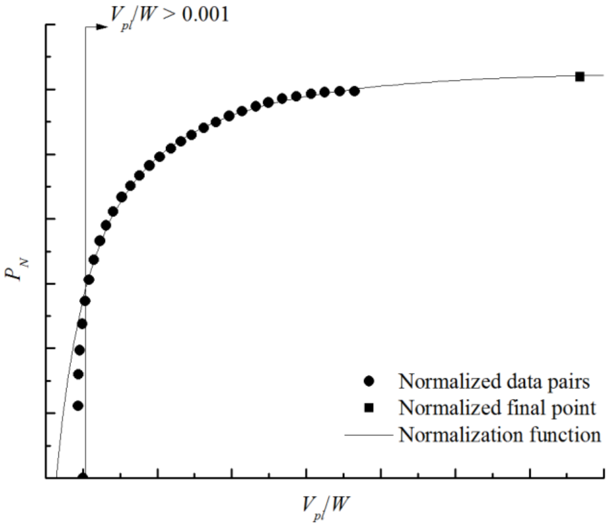

Fig. 4.3 Normalization function shown fitted to the normalization data

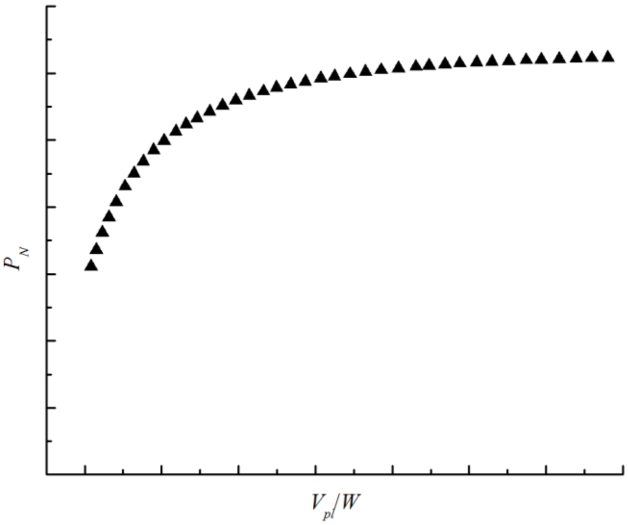

Fig. 4.4 Data adjusted to place all points on the analytical NM function

6) Starting at the first data point with $V_{pli}/W > 0.002$, an iterative procedure is used to force P_{Ni}, V_{pli}/W and a_i data at each loading point to lie on the curve described by Eq. (4.6) by adjusting the crack size a_i (see Fig. 4.4).

7) Now that the crack size at each loading step is obtained, Eqs. (4.3) and (4.4) are used to evaluate the J value at each load point.

8) The *J*-*R* curve (schematically shown in Fig. 4.5) is generated by plotting $J_i(a_i)$ obtained in step 7) against the crack extension $\Delta a_i = a_i - a_0$.

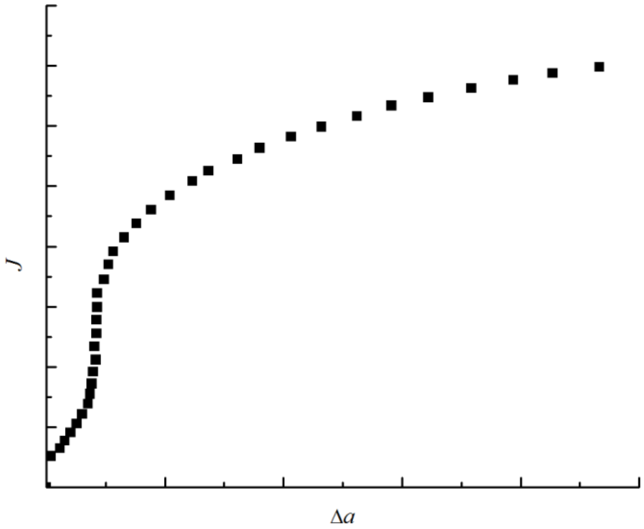

Fig. 4.5 The resulting *J*-*R* curve

In summary, the NM method involves normalizing the load-CMOD pairs, fitting the NM function, calculating the crack size at each loading step through an iterative procedure, calculating the *J*-integral and plotting the *J*-*R* curve. Note that the difference between the application of the NM method for the SE(T) specimen and that for the SE(B) or C(T) specimen only lies in the specific equations used to evaluate K_i, C_i, η_{pl} and γ_{LLD}.

4.2.2 Evolution of NM method

The NM method evolves from early studies of the ‘key curve’ (also called ‘F_1 function’) method and principle of load separation developed in the late 1970s [129-131]. Ernst et al. [129] conducted dimensional analyses of the relationships among the load, crack length and normalized plastic displacement, and proposed the following equation:

$$P = \frac{b^2}{W} F_1\left(\frac{V_{pl}}{W}, \frac{a}{W}, \frac{B}{W}\right) \tag{4.7}$$

where

F_1 is the key curve function, which is a function of V_{pl}/W, a/W and B/W.

Equation (4.7) indicates that the function F_1 represents the load-plastic displacement relationship. Note that F_1 presents the early form of the plastic function H, which will be introduced in Eq. (4.16).

The work in [129] and [130] led to the concept of load separation [131]. In the test of a precracked specimen, the load, the displacement V can be separated into the elastic (V_{el}) and plastic (V_{pl}) components:

$$V = V_{el} + V_{pl} \tag{4.9}$$

where

$$V_{el} = PC\left(\frac{a}{W}\right) \tag{4.10}$$

The load P is assumed to be a function of a/W and V_{pl}/W by two multiplicative functions:

$$P = G\left(\frac{a}{W}\right) H\left(\frac{V_{pl}}{W}\right) \tag{4.11}$$

Rearranging Eq. (4.11) results in the normalized load P_N as follows:

$$P_N = \frac{P}{G\left(\frac{a}{W}\right)} = H\left(\frac{V_{pl}}{W}\right) \tag{4.12}$$

where

G is a geometry function that depends on the crack length only, and H is the plasticity function (or calibration function), which depends on the plastic component of the displacement only.

Sharobeam et al. [132] proposed $G(a/W)$ to be

$$G\left(\frac{a}{W}\right) = \frac{Bb^2}{W} \tag{4.13}$$

for the SE(B) specimen, and

$$G\left(\frac{a}{W}\right) = \frac{Bb^2}{W} e^{0.522\left(\frac{b}{W}\right)} \tag{4.14}$$

for the C(T) specimen.

Joyce [133] proposed the following geometry function for SE(B) and C(T) specimens:

$$G\left(\frac{a}{W}\right) = BW\left(1 - \frac{a_{bi}}{W}\right)^{\eta_{pl}} \tag{4.15}$$

The earliest form of the *H* function was proposed by Landes et al. [134] and Herrera et al. [135] to be a power-law function as follows:

$$H\left(\frac{V_{pl}}{W}\right) = P_N = \left(\frac{V_{pl}}{W\varsigma}\right)^{1/n} \tag{4.16}$$

where

ς is the fitting coefficient to be determined;

n is the strain-hardening exponent in the Ramberg-Osgood stress-strain relationship.

Equation (4.16) implies that only one point on the load-displacement curve (e.g. the final displacement and corresponding load) is needed to determine the constants ς and then the entire calibration curve.

The following two-branch function consisting of a power-law function and a linear function was later proposed in [136] to improve Eq. (4.16).

$$P_N = \begin{cases} \left(\frac{V_{pl}}{W\varsigma}\right)^{1/n} & V_{pl} > 0.1 \\ D_1 + D_2\left(\frac{V_{pl}}{W}\right) & V_{pl} \le 0.1 \end{cases} \tag{4.17}$$

where

D_1 and D_2 are the fitting coefficients.

The so-called ‘*LMN*’ function, based on the work of Orange [137], was proposed by Landes et al. [138]:

$$P_N = \left[\frac{L + M \cdot \left(\frac{V_{pl}}{W} \right)}{N + \left(\frac{V_{pl}}{W} \right)} \right] \left(\frac{V_{pl}}{W} \right) \tag{4.18}$$

where

L, *M* and *N* are the fitting coefficients.

Equation (4.18) represents a power-law relationship between P_N and V_{pl}/W for small values of V_{pl}/W, and an approximately linear relationship between P_N and V_{pl}/W for large values of V_{pl}/W. Experimental results of 67 different-sized C(T) specimens made of six different materials in [138] showed that the ‘*LMN*’ function markedly improved the accuracy of the *J*-*R* curve compared with Eq. (4.17).

In 2001, the NM method was standardized in the ASTM E1820-01 standard for the *J*-*R* curve testing under high loading rates. A slightly revised ‘*LMN*’ function, i.e. the ‘*LMNO*’ function was adopted in the standard:

$$P_N = \frac{L + M \cdot \left(\frac{V_{pl}}{W} \right) + N \cdot \left(\frac{V_{pl}}{W} \right)^2}{O + \left(\frac{V_{pl}}{W} \right)} \tag{4.19}$$

where

L, *M*, *N*, and *O* are the fitting coefficients.

Zhu et al. [119] developed *J*-*R* curves for standard and non-standard SE(B) specimens ($0.135 \leq a_0/W \leq 0.83$) made of HY80 steel using the NM method. They found that the developed *J*-*R* curves are in good agreement with those obtained by the UC method. Their study suggests that the NM method is applicable to both standard and non-standard SE(B) specimens. Zhu et al. [166] further employed the NM method to develop *J*-*R* curves for pin-loaded deeply-cracked side-grooved SE(T) specimens of X60-grade steel. It was shown that the *J-R* curve developed from the NM method agreed well with that obtained from the UC method.

Fortes et al. [139] showed that the NM method employing the '*LMN*' function leads to *J-R* curves that agree well with those obtained from the UC method for side-grooved SE(B) specimens tested at four different temperatures. Scibetta et al. [118] validated the NM method based on numerical simulation of 2D FEA of SE(B) and C(T) specimens made of typical low and high toughness ferritic steels. The numerical validation results showed that the NM method is very accurate in terms of predicting the *J-R* curves in all cases.

Kong et al. [140] recently proposed a modified NM method in which the normalized load P_N was further normalized by the yield strength σ_{YS} to become dimensionless. The CTOD-*R* curves for three SE(T) specimens fabricated from a section of X90-grade pipeline segment were obtained from the modified NM and UC methods. It was observed that the CTOD-*R* curves obtained from these two methods agree well.

4.3 Validation of NM method for SE(T) specimens

Although the application of the NM method to the SE(T) specimen-based *J-R* curve testing has been studied in previous studies, there is a lack of a systematic investigation of the adequacy of the NM method with respect to the SE(T) specimen. To this end, the NM method was employed to determine *J-R* curves for six SE(T) specimens tested by Wang et al. [114] (see Section 3.1 for details of these specimens) and 21 SE(T) specimens analyzed using the GTN model and computational cell methodology (see Section 3.5 for details of these models). The equations of *J*-integral calculation (i.e. equations for the calculation of *K*, *C* and η_{pl}) for SE(T) specimen are given in APPENDIX B. The *J-R* curves determined from the NM method are then compared with those determined from the UC method to systematically investigate the adequacy of the NM method for SE(T) specimens. The fitting coefficients (i.e. *L*, *M*, *N* and *O*) of the NM function (see Eq. (4.6)) for six test specimens are listed in Table C.1 of APPENDIX C.

i) Validation using six test specimens:

Figure 4.6 compares the *J-R* curves obtained from the NM and UC methods for all 6 test specimens. According to ASTM E1820-17 [12], the *J-R* curves are fitted in the following power-law form:

$$J = C_1 \cdot \Delta a^{C_2} \tag{4.20}$$

where

C_1 and C_2 are coefficients of the power-law function determined from curve fitting the J-Δa data points.

Table 4.1 shows the comparison of crack lengths obtained from the 9-point average technique and UC method for six specimens. The errors of initial crack length, final crack length, and crack extension between the two methods are respectively defined as follows:

$$e_{a1} = \frac{a_{0\mathrm{NM}} - a_{0\mathrm{UC}}}{a_{0\mathrm{UC}}} \times 100\% \tag{4.21}$$

$$e_{a2} = \frac{a_{f\mathrm{NM}} - a_{f\mathrm{UC}}}{a_{f\mathrm{UC}}} \times 100\% \tag{4.22}$$

$$e_{a3} = \frac{a_{\Delta a\mathrm{NM}} - a_{\Delta a\mathrm{UC}}}{a_{\Delta a\mathrm{UC}}} \times 100\% \tag{4.23}$$

Table 4.1 Crack lengths obtained from 9-point average technique and UC method

Specimen Number	9-point			UC			Error (%)		
	a_0 (mm)	a_f (mm)	Δa (mm)	a_0 (mm)	a_f (mm)	Δa (mm)	e_{a1}	e_{a2}	e_{a3}
SE(T)-SG05-01	10.151	12.886	2.735	10.312	13.649	3.337	1.6	5.9	22.0
SE(T)-SG05-02	10.447	12.730	2.283	10.367	12.532	2.165	-0.8	-1.6	-5.2
SE(T)-PS05-01	11.221	14.264	3.043	10.667	12.309	1.642	-4.9	-13.7	-46.0
SE(T)-PS05-02	11.492	14.270	2.778	10.376	12.516	2.141	-9.7	-12.3	-22.9
SE(T)-SG25-01	5.165	8.421	3.256	5.218	8.404	3.186	1.0	-0.2	-2.1
SE(T)-SG25-02	5.233	8.741	3.508	5.290	8.677	3.387	1.1	-0.7	-3.5

Figure 4.6 indicates that for the SG05 and SG25 SE(T) specimens, the fitted *J-R* curves obtained by the UC and NM methods agree reasonably well. However, for the two PS05 specimens, non-negligible deviations exist between the fitted lines. This is due to the inaccurate estimation of the crack lengths performed by the UC method (i.e. the maximum error of Δa is about 46%). As indicated in Table 4.1, the initial crack lengths of SE(T)-PS05-01 and SE(T)-PS05-02 specimens are underestimated by the UC method by 4.9% and 9.7%, respectively, while the final crack lengths are underestimated by the UC method by 46.0% and 22.9%, respectively.

It is worth pointing out that the *J-R* curves determined from the NM method tend to inaccurate for small crack extensions (less than about 0.2 mm) [118]. This is due to the high sensitivity of the crack length to the normalized load, whereby relatively small changes in the normalized load can result in large changes in the estimated crack length. The oscillations are not shown in current figures by eliminating the portion before the crack extension of Δa = 0.2 mm and replacing with a straight-line between the origin and the point corresponding to the crack extension of Δa = 0.2 mm.

In order to quantify the adequacy of the NM method in terms of generating *J-R* curves for the SE(T) specimen, the relative error, e_{J1}, is defined as:

$$e_{J1} = \frac{J_{\mathrm{NM}} - J_{\mathrm{UC}}}{J_{\mathrm{UC}}} \times 100\% \tag{4.24}$$

where

J_{NM} and J_{UC} denote the *J* values at a given crack extension Δa in the fitted *J-R* curves corresponding to the UC and NM methods, respectively.

Table 4.2 lists the error of *J* values determined from the NM method compared with those determined from the UC method, at selected values of the crack extension. The table indicates that $|e_{J1}|$ in general decreases as Δa increases. The difference between J_{NM} and J_{UC} is the smallest for SG05 specimens among all the specimens ($|e_{J1}| < 10\%$). The largest difference between J_{NM} and J_{UC} occurs for the SE(T)-PS05-01 specimen, with $|e_{J1}|$ being as large as over 20%. As discussed previously, this is due to the inaccurate estimation of the crack lengths performed by the UC method.

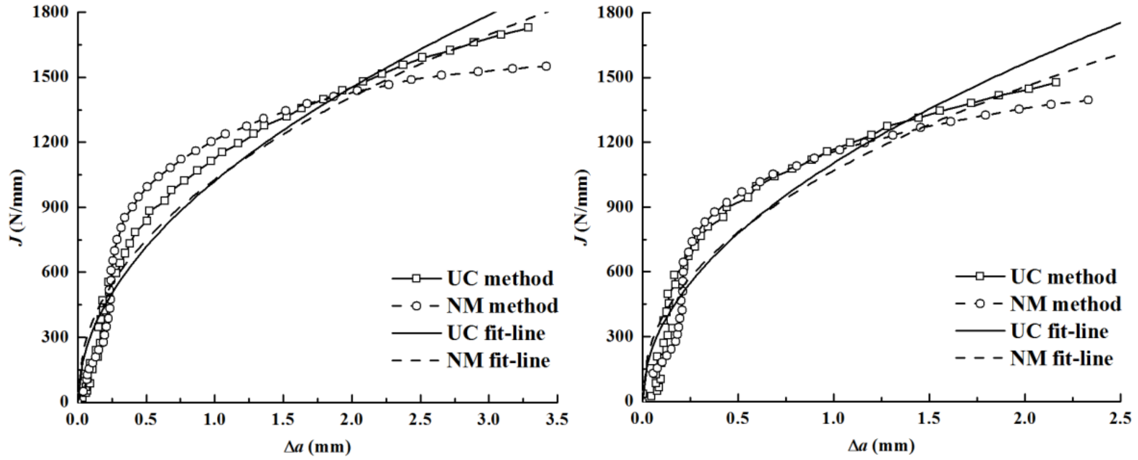

(a) SE(T)-SG05-01 (b) SE(T)-SG05-02

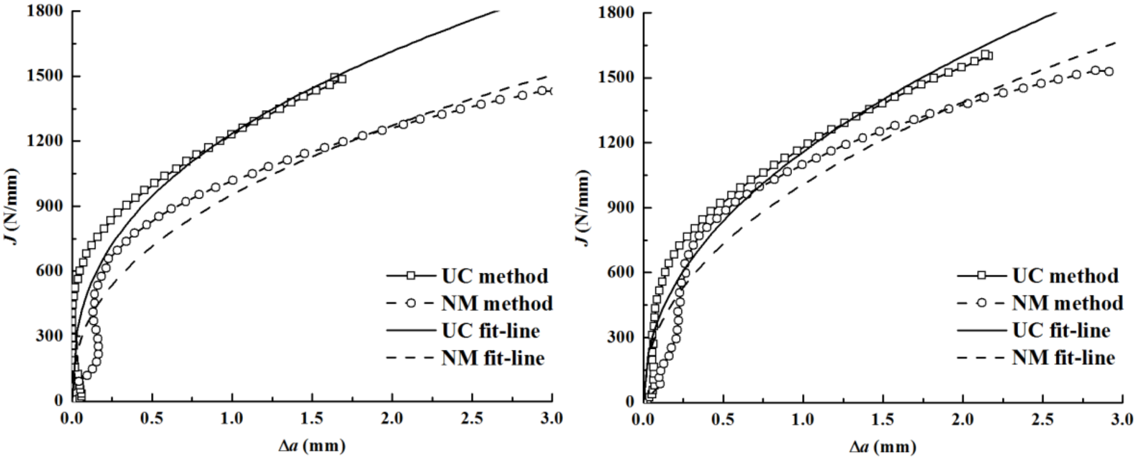

(c) SE(T)-PS05-01 (d) SE(T)-PS05-02

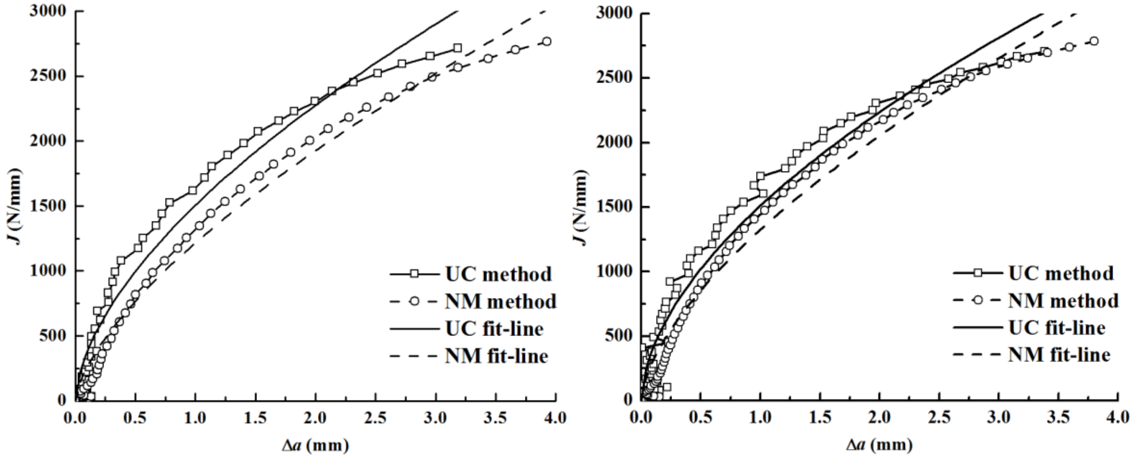

(e) SE(T)-SG25-01 (f) SE(T)-SG25-02

Fig. 4.6 Comparison of *J-R* curves obtained from UC method and NM method

Table 4.2 Error of the predicted *J-R* curves using NM method for six test specimens

Specimen Number	Error e_{J1} (%)					
	Δa=0.2 (mm)	Δa=0.5 (mm)	Δa=1.0 (mm)	Δa=1.5 (mm)	Δa=2.0 (mm)	Δa=2.5 (mm)
SE(T)-SG05-01	9.7	4.5	0.7	-1.5	-3.0	-4.1
SE(T)-SG05-02	6.2	0.8	-3.2	-5.4	-6.9	-8.1
SE(T)-PS05-01	-26.5	-24.5	-22.9	-21.9	-21.3	-20.7
SE(T)-PS05-02	-12.2	-12.6	-13.0	-13.1	-13.3	-13.4
SE(T)-SG25-01	-27.5	-22.9	-19.3	-17.0	-15.4	-14.1
SE(T)-SG25-02	-21.3	-16.3	-12.3	-9.9	-8.1	-6.8

ii) Validation using 21 growing-crack FE models:

Figure 4.7 compares the *J-R* curves obtained from the NM and UC methods for the 21 FE models described in Section 3.3.1. The fitting coefficients (i.e. *L*, *M*, *N* and *O*) of the NM function (see Eq. (4.6)) for 21 GTN-based FE models are listed in Table C.2 of APPENDIX C. For simplicity, only fitted curves are shown in Fig. 4.7. It can be observed that the results obtained from the NM method agree reasonably well with those obtained from the UC method for all cases, especially for deeply-cracked FE models.

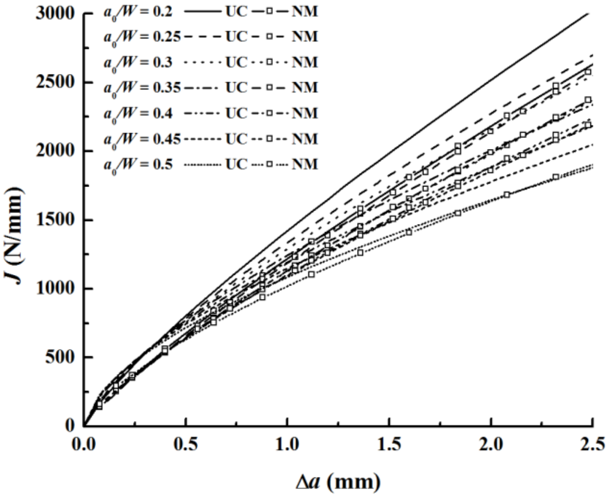

(a) PS specimens with *B*/*W* = 1

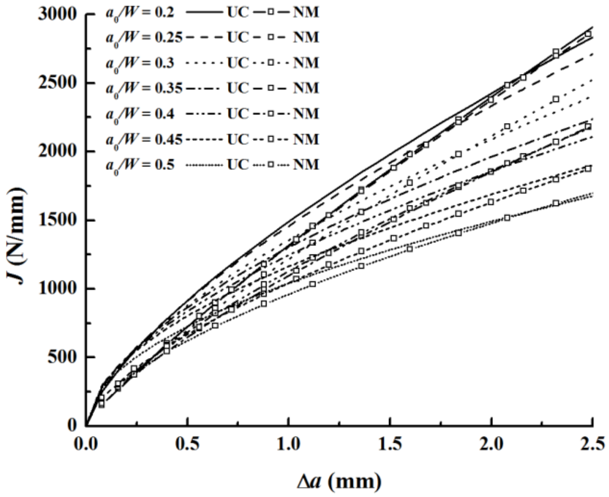

(b) SG specimens with B/W = 1

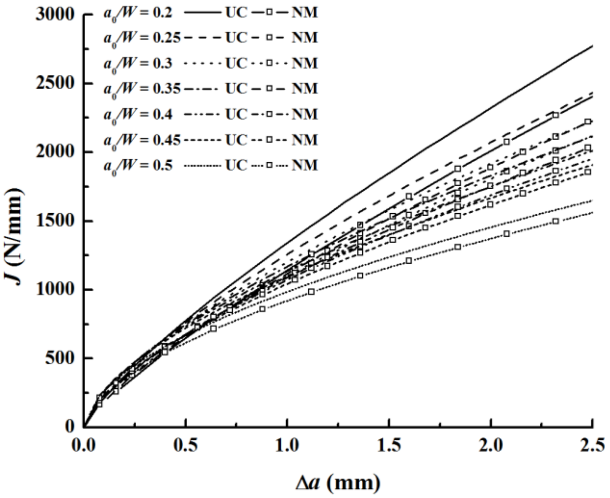

(c) PS specimens with B/W = 0.5

Fig. 4.7 *J-R* curves obtained from UC method and NM method for 21 FE models

Table 4.3 lists the values of e_{J1} at selected crack extensions for all FE models. For all cases at relatively small crack extensions (e.g. $\Delta a \leq 1.0$ mm), the J values evaluated using the NM method are smaller than those evaluated using the UC method. As the crack extension increases, the value of e_{J1} becomes smaller. At the crack extension of $\Delta a = 2.5$ mm, the relative error for all SG specimens are within 6%, and the relative error for intermediate to deeply-cracked (e.g. $a_0/W \geq 0.3$) specimens are also small, within 8%. However, for PS specimens with relatively shallow cracks (i.e. $a_0/W \leq 0.25$), the relative error can be as high as -13%.

Table 4.3 Error of the predicted *J-R* curves using NM method for 21 FE models

(a) PS specimens with *B*/*W* = 1

a_0/W	Error e_{J1} (%) Δa=0.2 mm	Δa=0.5 mm	Δa=1.0 mm	Δa=1.5 mm	Δa=2.0 mm	Δa=2.5 mm
0.2	-16.5	-15.3	-14.3	-13.7	-13.3	-13.0
0.25	-21.5	-18.2	-15.6	-14.1	-12.9	-12.1
0.3	-22.7	-14.6	-8.0	-3.8	-0.8	1.6
0.35	-25.2	-16.3	-8.9	-4.3	-0.9	1.9
0.4	-23.5	-14.9	-7.7	-3.2	0.1	2.7
0.45	-22.7	-12.9	-4.6	0.6	4.4	7.5
0.5	-18.3	-12.0	-6.8	-3.7	-1.4	0.4

(b) PS specimens with *B*/*W* = 0.5

a_0/W	Error e_{J1} (%) Δa=0.2 mm	Δa=0.5 mm	Δa=1.0 mm	Δa=1.5 mm	Δa=2.0 mm	Δa=2.5 mm
0.2	-17.5	-16.0	-14.8	-14.0	-13.5	-13.1
0.25	-16.3	-13.4	-11.2	-9.9	-8.9	-8.2
0.3	-14.3	-11.0	-8.4	-6.9	-5.8	-4.9
0.35	-12.4	-9.3	-6.8	-5.4	-4.3	-3.5
0.4	-9.7	-7.3	-5.4	-4.2	-3.4	-2.8
0.45	-9.1	-6.8	-4.9	-3.8	-3.0	-2.4
0.5	-8.6	-7.5	-6.5	-6.0	-5.6	-5.3

(c) SG specimens with *B*/*W* = 1

a_0/W	Error e_{J1} (%) Δa=0.2 mm	Δa=0.5 mm	Δa=1.0 mm	Δa=1.5 mm	Δa=2.0 mm	Δa=2.5 mm
0.2	-31.6	-20.8	-11.5	-5.5	-1.1	2.5
0.25	-32.4	-20.4	-10.0	-3.3	1.8	5.9
0.3	-31.7	-20.1	-10.1	-3.7	1.2	5.1
0.35	-33.5	-22.7	-13.3	-7.3	-2.8	0.9
0.4	-30.3	-20.4	-12.0	-6.7	-2.7	0.5
0.45	-24.5	-16.7	-10.3	-6.3	-3.4	-1.0
0.5	-21.4	-13.8	-7.6	-3.7	-0.9	1.4

4.4 *J*-CMOD relationship

4.4.1 *J*-CMOD relationship for test specimens

Let J_N and V_N denote the normalized J and CMOD values, respectively. The following equations are used to define J_N and V_N, respectively:

$$J_N = \frac{J}{b_0 \sigma_Y} \tag{4.25}$$

$$V_N = \frac{V}{a_0} \tag{4.26}$$

where

σ_Y is the effective yield strength and is calculated as the average of ultimate tensile strength σ_{TS} and 0.2%-offset yield strength σ_{YS}, (see Eq. (3.3)).

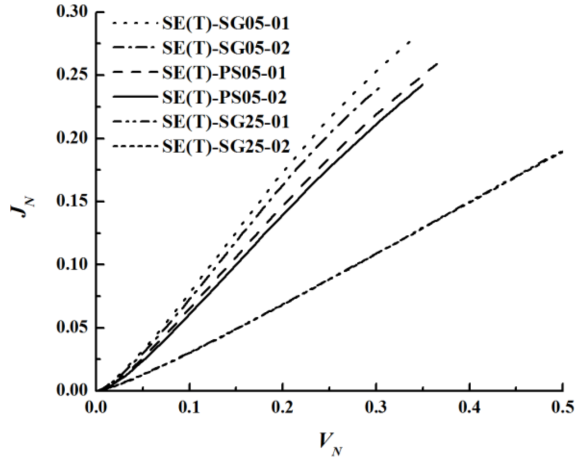

Fig. 4.8 J_N-V_N relationship for test specimens

Figure 4.8 shows the relationship between J_N and V_N for the SE(T) specimens tested by Wang et al. [114] (see Chapter 3). As can be observed, the J_N-V_N relationship is approximately linear (and close to power-law for some specimens). This observation is consistent with the observation made by Bolinder et al. [72, 141] for notched bend type specimens with different crack depths, with or without residual stresses. The approximate linear relationships between the material resistance and displacement (i.e. CTOD, CMOD and the rotational angle of the crack plane) for SE(B) or SE(T) specimens have also been reported in other studies [101, 142-144].

4.4.2 *J*-CMOD relationship for growing-crack FE models

Figure 4.9 shows the J_N-V_N relationship for the 21 GTN-based FE models described in Chapter 3. As can be observed, the J_N-V_N relationship is approximately linear for some specimens and close to power-law for the other.

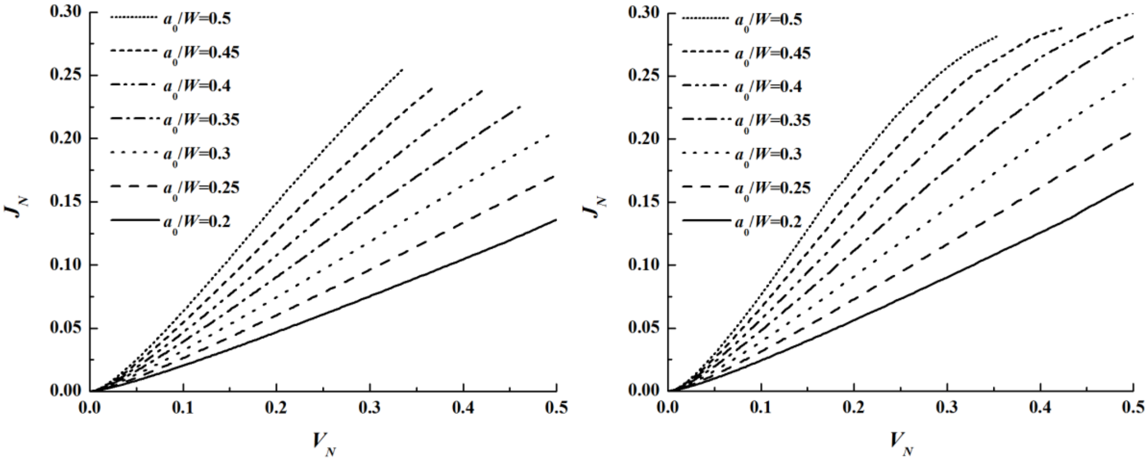

(a) PS FE models with *B*/*W* = 1 (b) SG FE models with *B*/*W* = 1

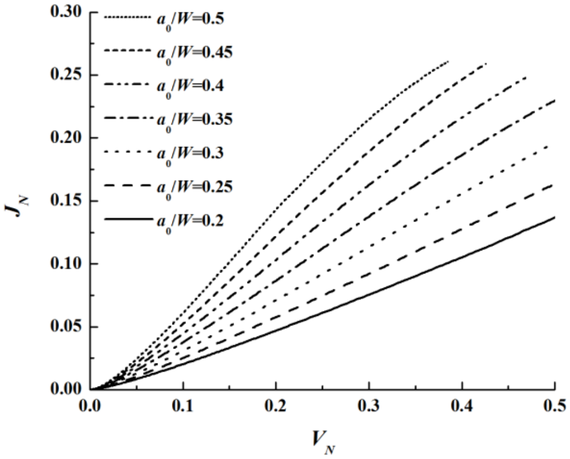

(c) PS FE models with *B*/*W* = 0.5

Fig. 4.9 J_N-V_N relationship for GTN models with growing crack

4.4.3 *J*-CMOD relationship for stationary-crack FE models

Huang et al. [145] studied the *J*-CTOD relationship for the SE(T) specimen by carrying out FEA of a series of SE(T) models with wide ranges of geometric configurations and material properties, i.e. a_0/W = 0.2, 0.3, 0.4, 0.5, 0.6 and 0.7; B/W = 1 and 2; PS/SG; n = 5, 8.5, 10, 15 and 20, where n is the strain hardening exponent. The stationary-crack assumption was adopted in their analysis. Figure 4.10 shows the J_N-V_N relationships for the PS SE(T) models with B/W = 1 analyzed by Huang et al. [145]. As can be observed, the J_N-V_N relationship is similar to that shown in Figs. 4.8 and 4.9. The J_N-V_N relationships for the other models analyzed by Huang et al. [145] are similar to those shown in Fig. 4.10 and therefore not shown for the sake of brevity.

Figures 4.8 through 4.10 suggest that the approximate linear/power-law relationship between J_N and V_N can be exploited to develop an empirical equation to evaluate *J* directly from CMOD, which markedly simplifies the procedure for the *J* evaluation currently employed in the NM method. Because the FE SE(T) models analyzed by Huang et al. [145] cover wide ranges of specimen configurations and material properties, and because the virtual crack extension method used to evaluate *J* in Huang et al.'s study is considered the exact method for the *J* evaluation (the η factor- based method used to evaluate *J* for the test specimens and GTN-based FE models is considered an approximate approach), the J_N-V_N results obtained by Huang et al. were used to develop the empirical equation to evaluate *J*, whereas the J_N-V_N results corresponding to the test specimens and GTN models are used to validate the developed empirical equation.

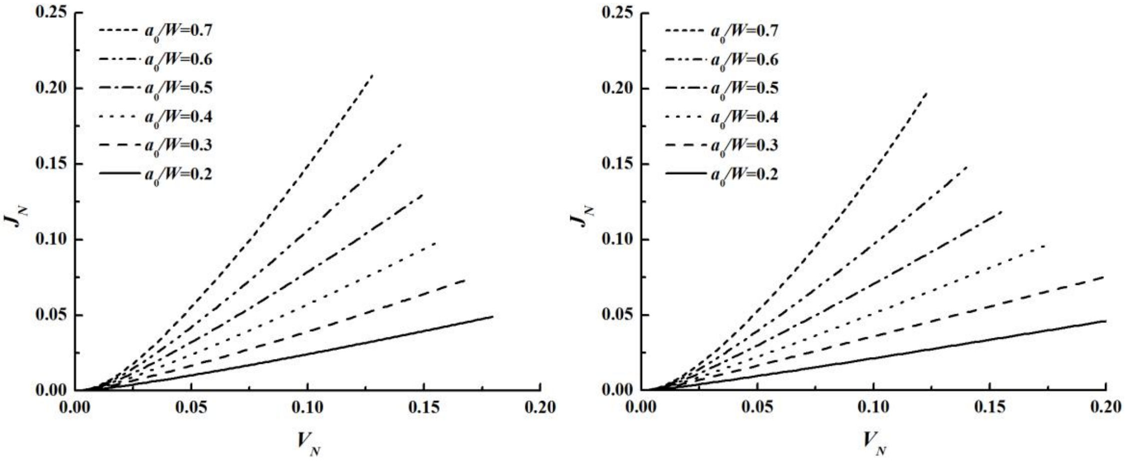

(a) *n* = 5 **(b) *n* = 8.5**

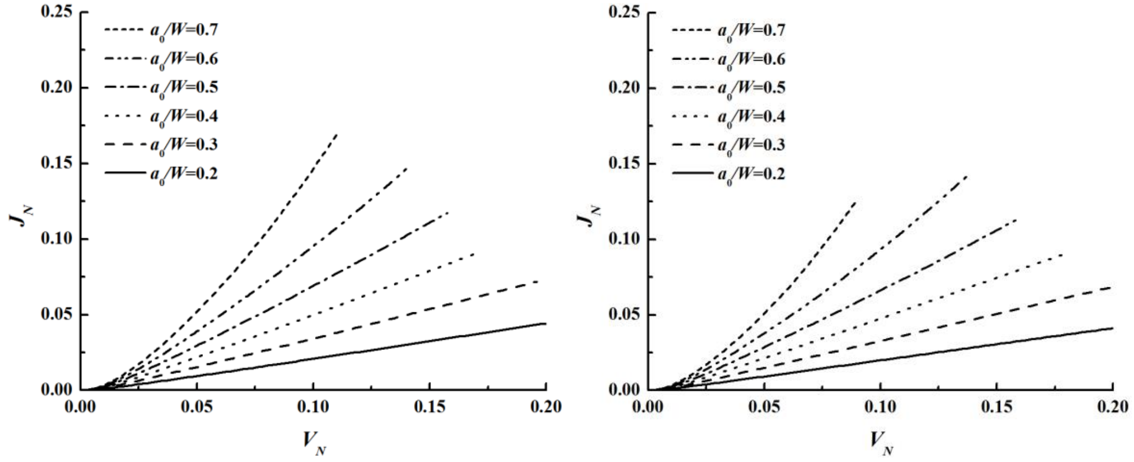

(c) ***n*** **= 10** (d) ***n*** **= 15**

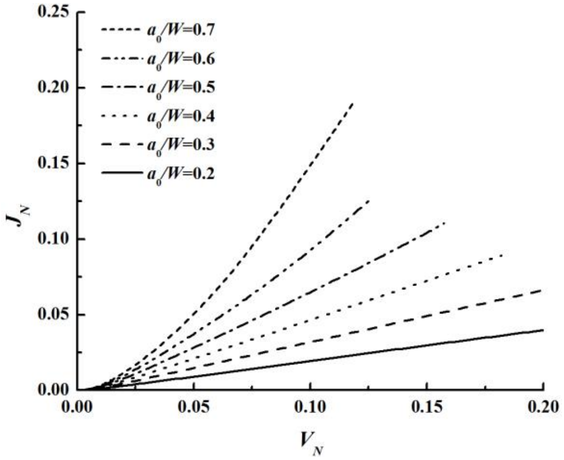

(e) ***n*** **= 20**

Fig. 4.10 J_N-V_N relationship for stationary-crack PS FE models with $B/W = 1$

4.5 Evaluation of J using CMOD and k

Given Figs. 4.8 through 4.10, it is proposed that the following empirical equation be used to evaluate *J*:

$$J_N = kV_N \tag{4.27}$$

where

k is the empirical factor that relates V_N to J_N. Note that Eq. (4.27) is inspired by the commonly-used J-CTOD relationship as follows:

$$\frac{J}{\sigma_{YS}} = m\delta \tag{4.28}$$

where

m is known as the constraint factor, which relates J to CTOD.

As indicated in Section 4.4.3, the J_N and V_N results corresponding to the SE(T) specimens analyzed by Huang et al. [145] are used to develop the empirical equation for evaluating k. To this end, the values of k (obtained from J_N/V_N) for PS SE(T) specimens with $B/W = 1$ analyzed by Huang et al. are depicted in Figs. 4.11. The figure indicates that k is an increasing function of V_N. The value of k increases approximately linearly with V_N for relatively small values of V_N, say, $V_N \leq 0.02$; however, as V_N further increases, k increases slowly with V_N. Figure 4.12 shows the impact of the strain hardening exponent n on the value of k by re-plotting the results shown in Fig. 4.11 in terms of a_0/W and n. Figure 4.12 indicates that for given a_0/W ratio and loading level, k generally decreases as n increases. However, for $n > 8.5$, k is weakly dependent on n. Note that the above-mentioned observations are also applicable to the other SE(T) specimens analyzed by Huang et al., i.e. PS specimens with $B/W = 2$, and SG specimens with $B/W = 1$ and 2. For brevity, these results are not shown.

Figure 4.13 depicts the k values as a function of V_N for PS and SG specimens with $B/W =$ 1 and 2 and $n = 10$. The figure suggests that the B/W ratio has a negligible impact on k. On the other hand, Fig. 4.13 suggests that side-grooving has a non-negligible impact on k. The values of k for the SG specimens are generally 12%-14% higher than those for the PS specimens, all the other relevant parameters being the same. The above observations may be explained by the fact that side-grooving makes the plane-strain (as opposed to the plane-stress) condition more prevalent along the crack front, which tends to increase the k value. This is similar to the fact that the m value in the J-CTOD relationship as expressed in Eq. (4.26) is higher for the plane-strain condition than that for the plane-stress condition.

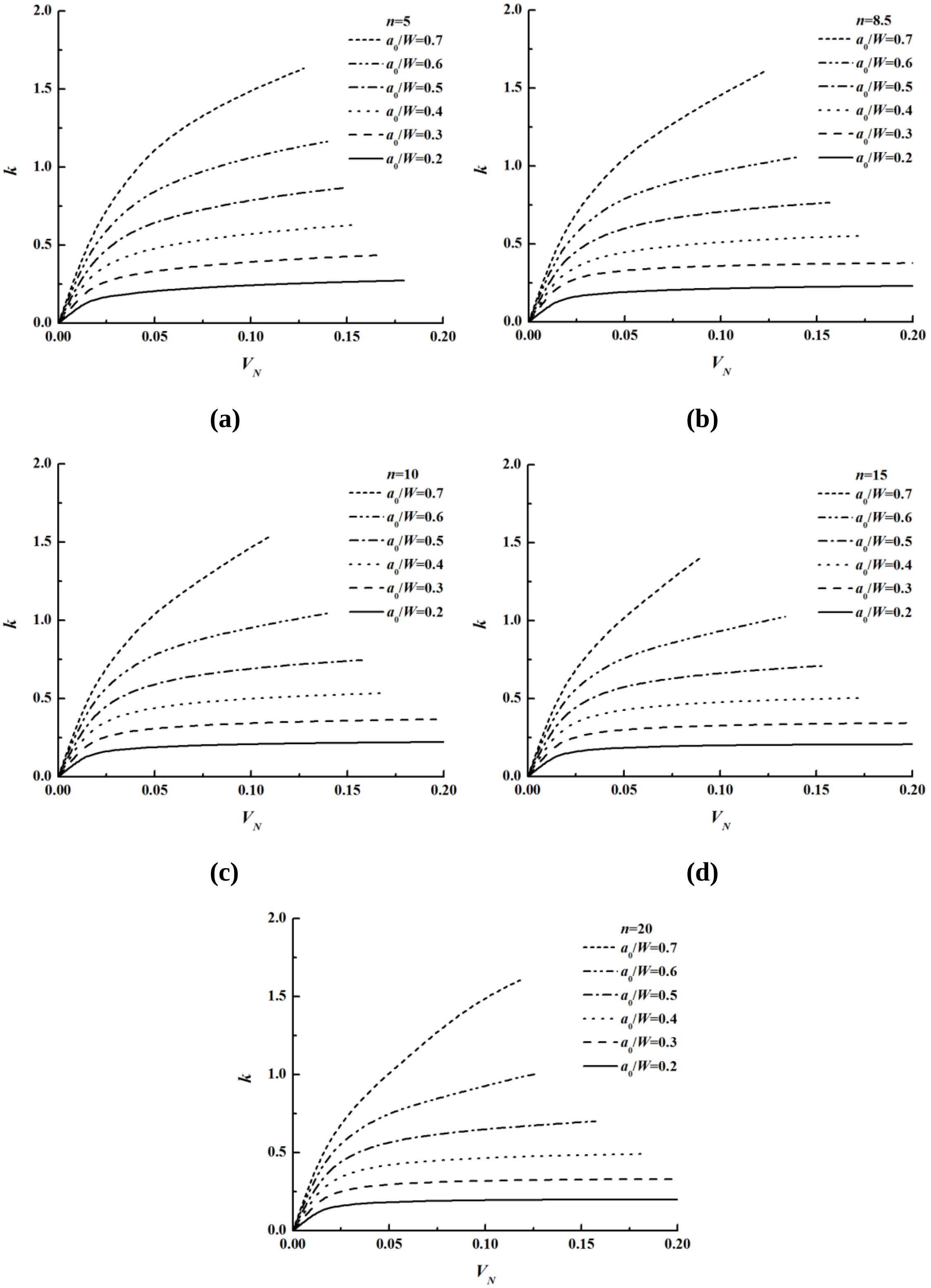

(a)

(b)

(c)

(d)

(e)

Fig. 4.11 Variation of k with V_N for various a_0/W for PS FE models with B/W = 1

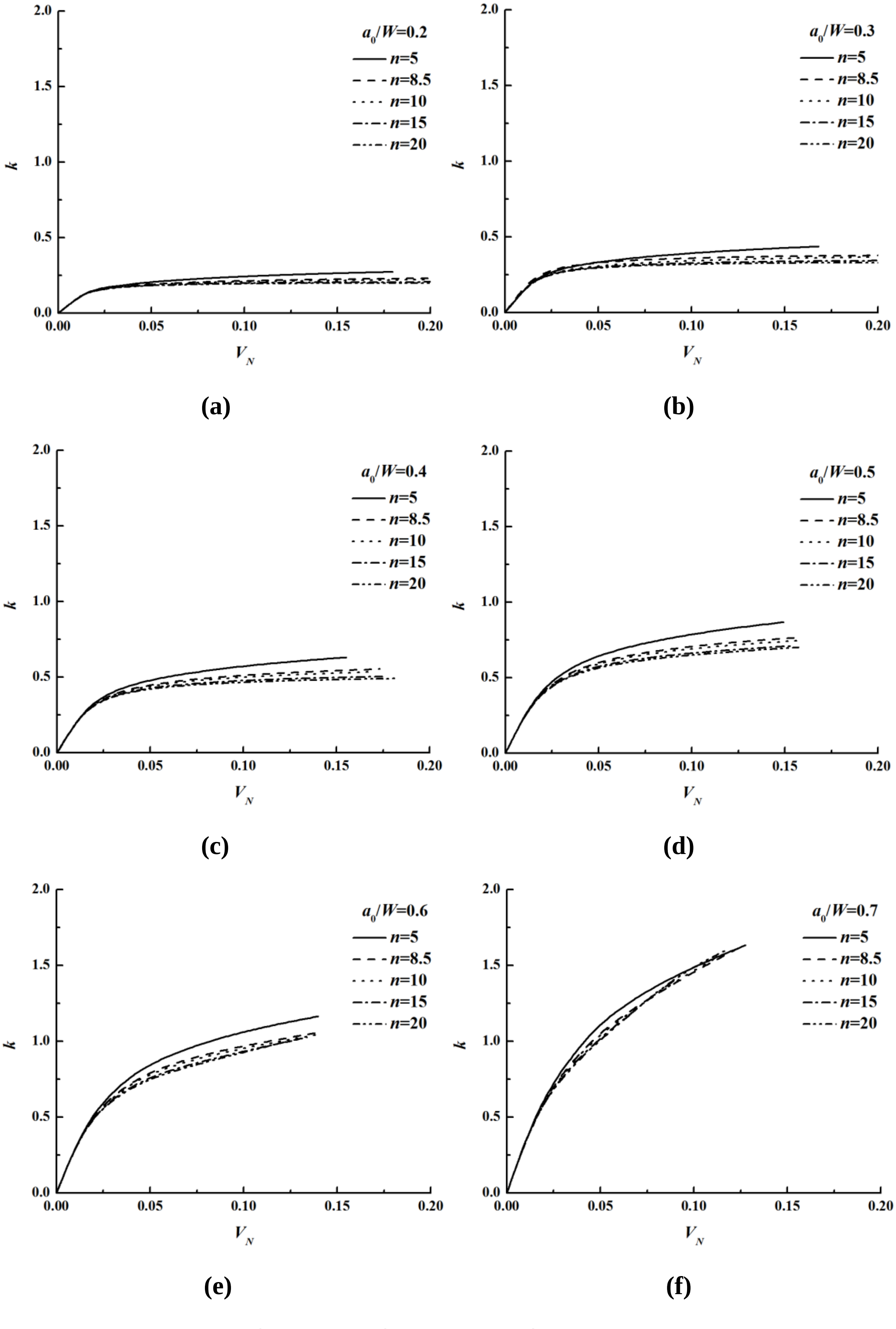

(a) (b)

(c) (d)

(e) (f)

Fig. 4.12 Variation of *k* with V_N for various *n* for PS FE models with *B*/*W* = 1

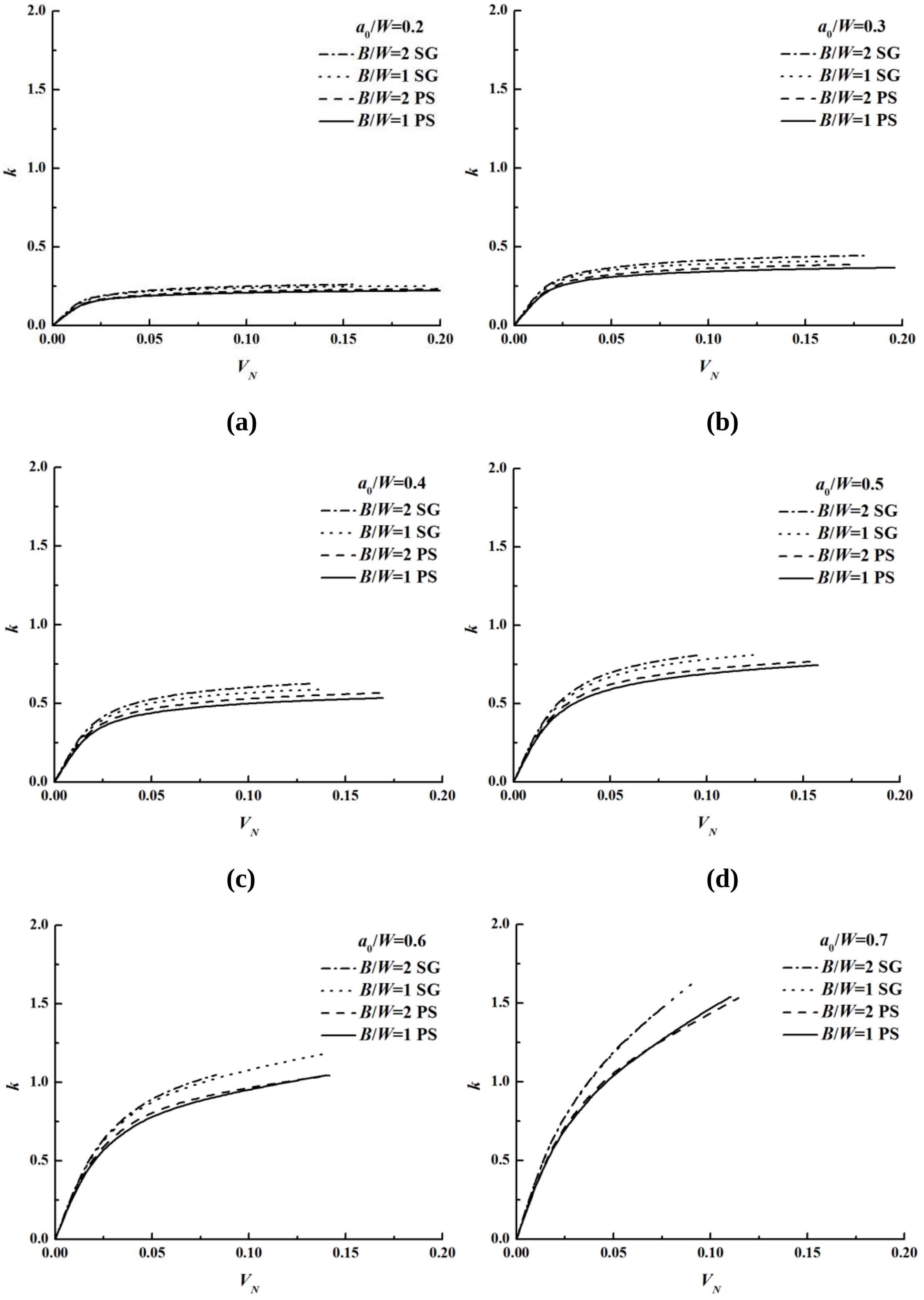

(a) (b)

(c) (d)

(e) (f)

Fig. 4.13 Variation of k with V_N for FE models with n = 10, various B/W and PS/SG

4.6 *k* equation

Based on the observations made from Figs. 4.11 through 4.13, the following empirical equation is proposed to evaluate *k*.

$$k = \begin{cases} \alpha \cdot 0.02^{\beta-1} \cdot \left(\dfrac{V}{a_0}\right) & \dfrac{V}{a_0} \leq 0.02 \\ \alpha \cdot \left(\dfrac{V}{a_0}\right)^{\beta} & \dfrac{V}{a_0} > 0.02 \end{cases} \tag{4.29}$$

where

α and β are fitting coefficients that depend on a_0/W, n and whether the specimen is plane-sided or side-grooved.

The values of α and β obtained using the least squares technique for different values of a_0/W and n are tabulated in Table 4.4. Note that the values of α and β for a_0/W and n values that are not listed in Table 4.4 but within the corresponding ranges (i.e. $0.2 < a_0/W < 0.7$ and $5 < n < 20$) can be evaluated using the linear interpolation.

Table 4.4 Coefficients *α* and *β*

(a) Plane-sided SE(T) specimen

PS		B/W = 1 or 2					
		$a_0/W = 0.2$	$a_0/W = 0.3$	$a_0/W = 0.4$	$a_0/W = 0.5$	$a_0/W = 0.6$	$a_0/W = 0.7$
α	$n = 5$	0.411	0.682	1.065	1.619	2.420	4.325
	$n = 8.5$	0.286	0.477	0.813	1.263	2.032	4.589
	$n = 10$	0.267	0.487	0.772	1.203	2.000	4.879
	$n = 15$	0.242	0.433	0.700	1.120	2.034	5.350
	$n = 20$	0.221	0.404	0.660	1.090	2.065	5.330
β	$n = 5$	0.232	0.244	0.273	0.316	0.360	0.463
	$n = 8.5$	0.133	0.130	0.207	0.257	0.323	0.498
	$n = 10$	0.116	0.160	0.195	0.246	0.322	0.521
	$n = 15$	0.093	0.130	0.173	0.231	0.337	0.555
	$n = 20$	0.066	0.111	0.158	0.228	0.346	0.555

(b) Side-grooved SE(T) specimen

SG		B/W = 1 or 2					
		$a_0/W = 0.2$	$a_0/W = 0.3$	$a_0/W = 0.4$	$a_0/W = 0.5$	$a_0/W = 0.6$	$a_0/W = 0.7$
α	$n = 5$	0.492	0.798	1.294	1.988	2.801	5.219
	$n = 8.5$	0.349	0.582	0.987	1.561	2.387	5.955
	$n = 10$	0.320	0.567	0.929	1.481	2.352	6.277
	$n = 15$	0.278	0.481	0.827	1.349	2.347	6.793
	$n = 20$	0.247	0.474	0.790	1.293	2.406	6.957
β	$n = 5$	0.248	0.252	0.296	0.344	0.371	0.485
	$n = 8.5$	0.158	0.170	0.230	0.287	0.340	0.542
	$n = 10$	0.133	0.167	0.215	0.275	0.3396	0.561
	$n = 15$	0.097	0.121	0.186	0.253	0.347	0.590
	$n = 20$	0.058	0.122	0.177	0.244	0.359	0.600

4.7 Validation of proposed k equation

The proposed k equation, i.e. Eq. (4.29), is first validated using the results obtained from the GTN-based FE models described in Chapter 3. Figure 4.14 shows the comparison of J-CMOD curves obtained from the η factor- and k factor-based methods for the PS and SG specimens with a_0/W = 0.2, 0.25, 0.3, 0.35, 0.4, 0.45 and 0.5, and B/W = 1. The figure indicates that for all cases considered, the J-CMOD curves obtained from the k factor-based method agree well with those obtained from the η factor-based method. To quantify the differences between the results of the two methods, the relative error e_{J2} is defined as follows:

$$e_{J2} = \frac{J_k - J_\eta}{J_\eta} \times 100\% \tag{4.30}$$

where

J_η and J_k are the J-integral values determined by the η factor- and k factor-based methods, respectively.

Figure 4.15 shows the variation of e_{J2} with CMOD. The figure indicates that $|e_{J2}|$ is in general less than about 11% for $V > 0.5$ mm. At CMOD around 0.2 mm, which corresponds to the initial crack blunting, e_{J2} can be as high as 40%. Furthermore, J_k values tend to agree with J_η somewhat better for the SG specimens than for the PS specimens.

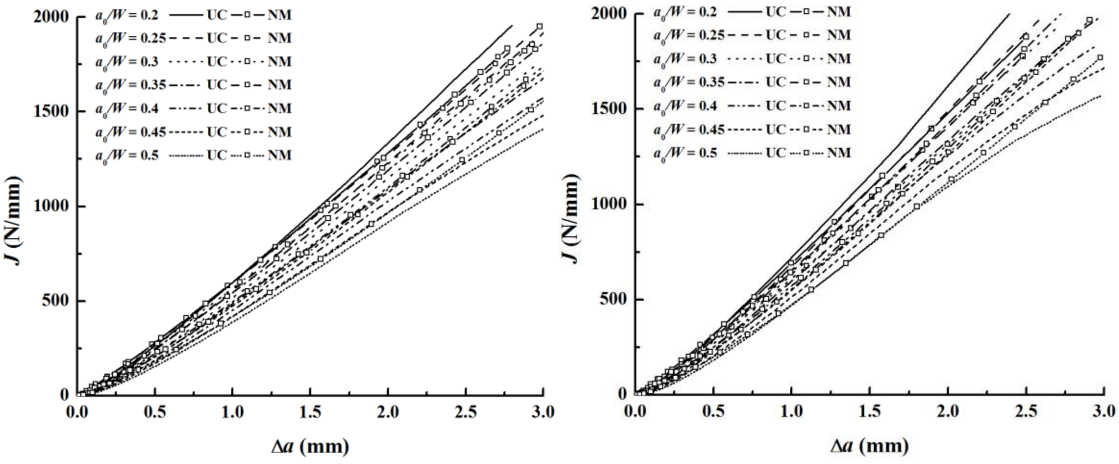

(a) PS models with *B*/*W* = 1 **(b) SG models with *B*/*W* = 1**

Fig. 4.14 Comparison of *J*-CMOD curves determined using *η* factor- and *k* factor-based methods for GTN models

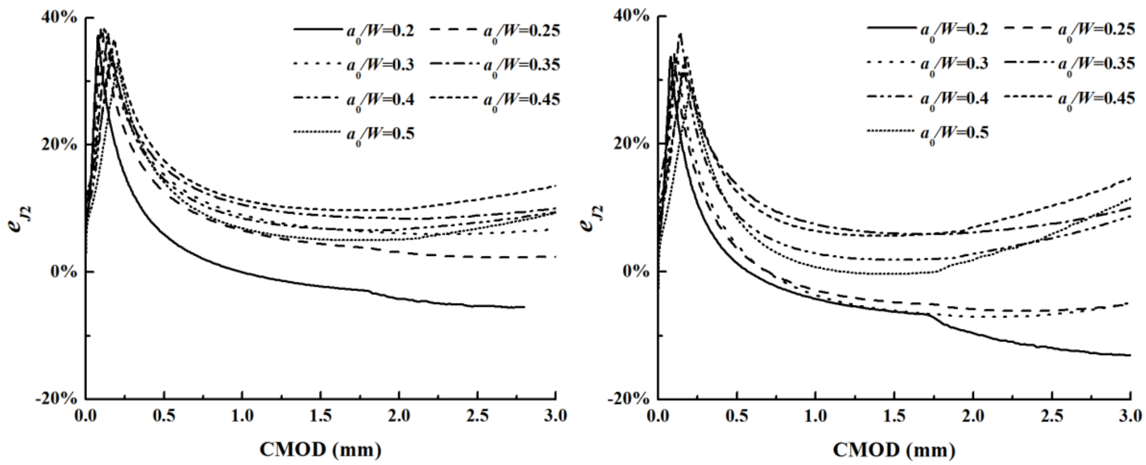

(a) PS models with *B*/*W* = 1 **(b) SG models with *B*/*W* = 1**

Fig. 4.15 Variation of relative error e_{J2} with CMOD

The results for the six SE(T) specimens tested by Wang et al. [114] are also used to validate the proposed *k* factor-based method for evaluating *J*. The *J*-CMOD curves obtained from the *η* factor- and *k* factor-based methods for the six specimens are compared in Fig. 4.16. It is observed that for deeply-cracked SG SE(T) specimens, the two methods yield essentially the same *J*-CMOD curves, whereas for shallow-cracked SG and deeply-cracked PS SE(T) specimens, the *J* values obtained from the *k* factor-based method are generally higher than those corresponding to the *η* factor-based method at high CMOD values.

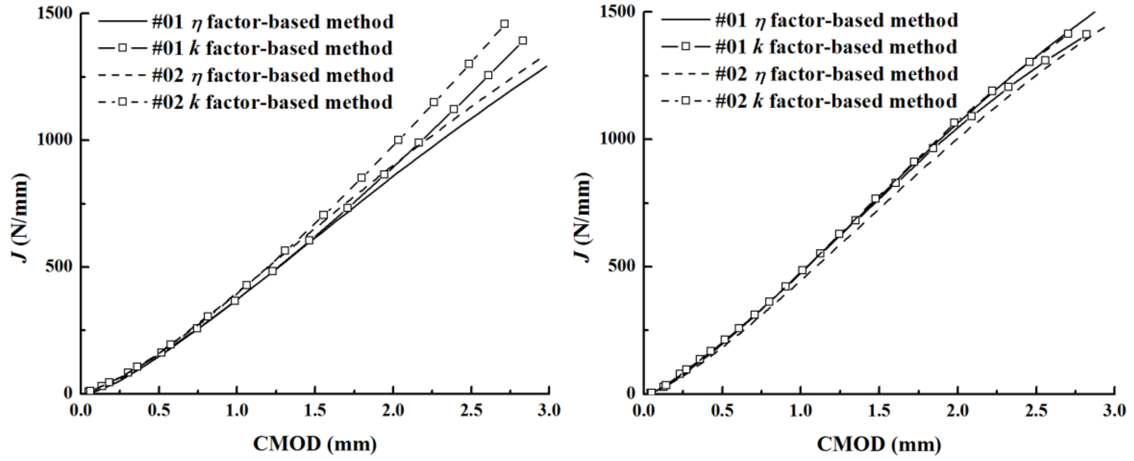

(a) PS SE(T) specimens with a_0/W = 0.5 **(b) SG SE(T) specimens with a_0/W = 0.5**

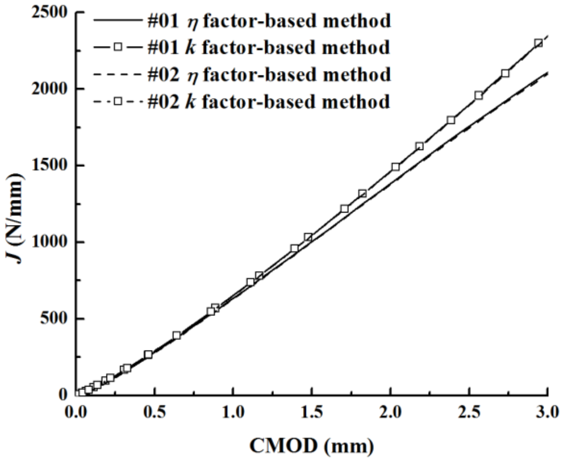

(c) SG SE(T) specimens with a_0/W = 0.25

Fig. 4.16 *J*-CMOD curves determined by the *η* factor- and *k* factor-based methods for test specimens

4.8 *k* factor-based NM method

The *k* factor-based method for evaluating *J* can be incorporated into the NM method to markedly simplify the *J* evaluation procedure involved in the NM method for the SE(T) specimen. The steps involved in the *k* factor-based NM method are the same as those described in Section 4.2.1, except that Eq. (4.4) for evaluating J_i is replaced by the following equation in step 2) and 7) as demonstrated in Section 4.2.1:

$$J_i = \frac{k_i V_i b_0 \sigma_Y}{a_0} \tag{4.31}$$

in which

k equation is given as Eq. (4.29).

4.9 Evaluation of *J-R* Curve Using *k* factor-based NM method

The six SE(T) specimens tested by Wang et al. [114] are used to illustrate the application of the proposed *k* factor-based NM method in this section. The X80-grade pipeline steel corresponds with σ_{YS}/σ_{TS} = 0.732 and n = 8.5 in the stationary-crack FEA. The corresponding α and β coefficients are interpolated from Table 4.4 given n = 8.5 as well as a_0/W listed in Table 4.5. The fitting coefficients C_1 and C_2 are also tabulated in the table. The initial crack length, final crack length and crack extension obtained from 9-point average measurement technique and UC method, as well as the corresponding errors are already tabulated in Table 4.1. Figure 4.17 presents the comparison results of *J-R* curves obtained from the UC, conventional NM and *k* factor-based NM method. It is worth noting that the *J-R* curves obtained from the *k* factor-based NM methods also present obvious oscillations at the beginning part, which has been discussed in Section 4.3 for the conventional NM method. The oscillations are not shown in current figures by eliminating the portion before the crack extension of Δa = 0.2 mm and replacing with a straight-line between the origin and the point corresponding to the crack extension of Δa = 0.2 mm.

Table 4.5 Values for *k* factor-based NM method

Specimen Number	*k* factor-based method			Fitting coefficients	
	a_0/W	α	β	C_1	C_2
SE(T)-SG05-01	0.508	1.626	0.291	1050	0.485
SE(T)-SG05-02	0.522	1.742	0.298	1063	0.553
SE(T)-PS05-01	0.561	1.732	0.297	958	0.468
SE(T)-PS05-02	0.575	1.840	0.307	1028	0.489
SE(T)-SG25-01	0.258	0.484	0.165	1270	0.731
SE(T)-SG25-02	0.262	0.494	0.165	1328	0.682

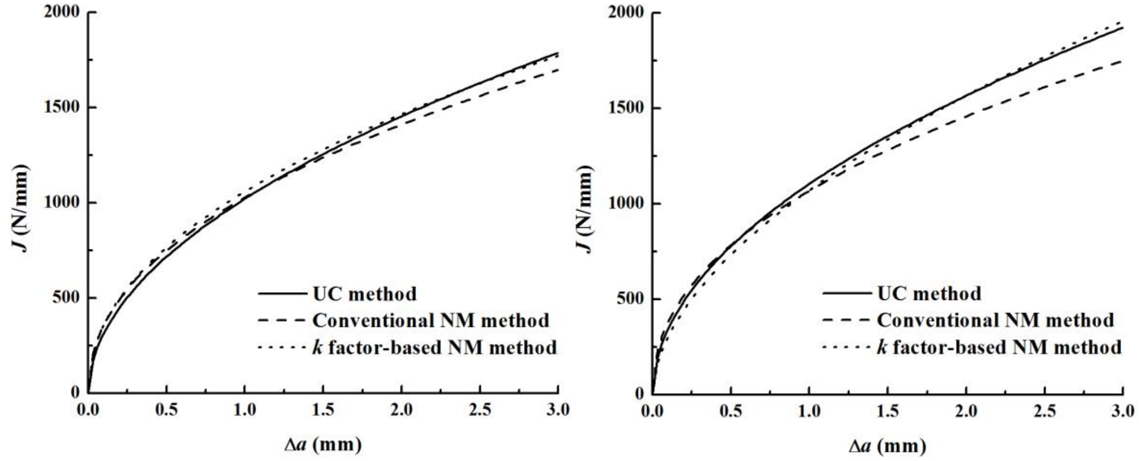

(a) SE(T)-SG05-01 **(b) SE(T)-SG05-02**

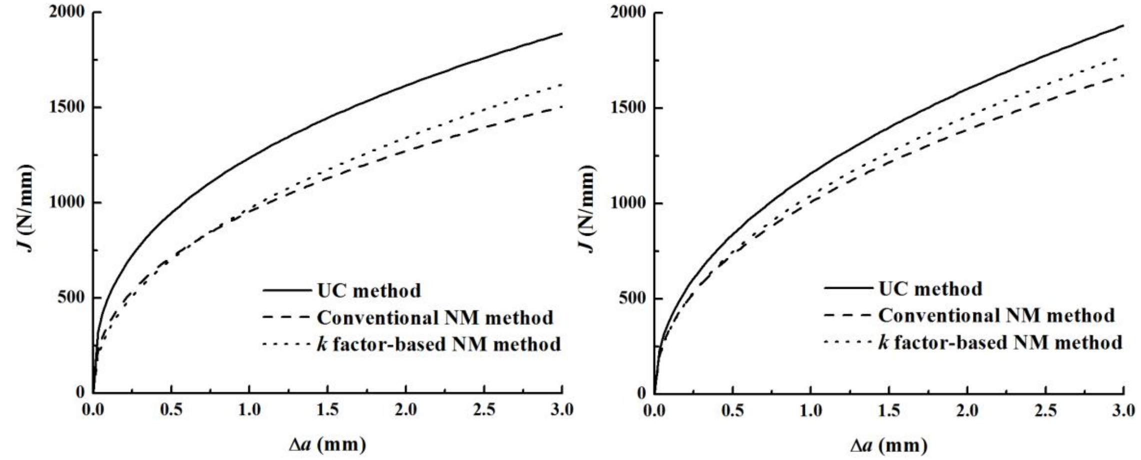

(c) SE(T)-PS05-01 **(d) SE(T)-PS05-02**

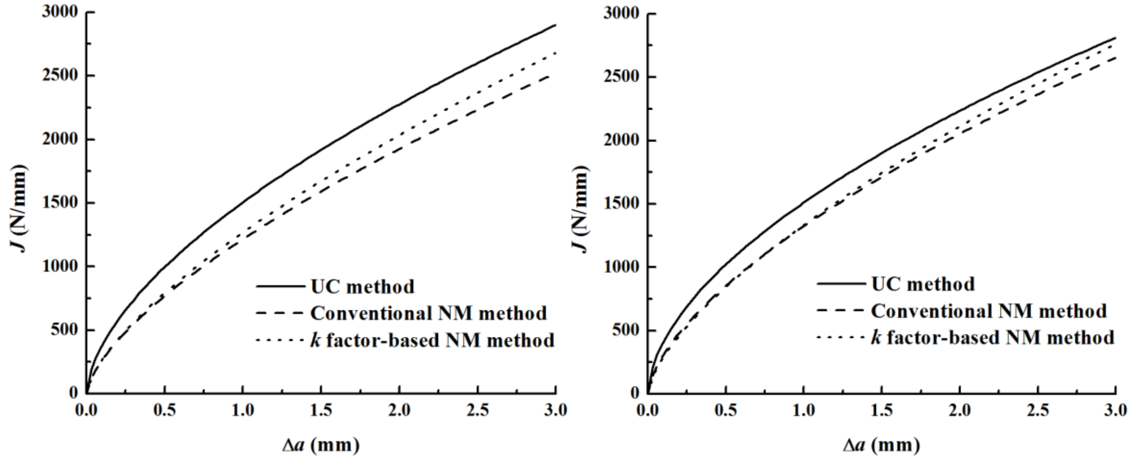

(e) SE(T)-SG25-01 **(f) SE(T)-SG25-02**

Fig. 4.17 *J-R* curves determined by UC method, conventional NM method and *k* factor-based NM method

For the two SG05 SE(T) specimens, the *J-R* curves obtained from the UC and *k* factor-based NM methods are almost identical. For the two SG25 SE(T) specimens, the *J-R* curves determined by the *k* factor-based NM method are slightly more conservative compared with those determined by the UC method. However, for the two PS05 SE(T) specimens, especially SE(T)-PS05-01, non-negligible deviation exists between the UC and conventional NM as well as *k* factor-based NM methods. This is due to the inaccurate estimation of the crack lengths performed by the UC method (e.g. the maximum error of Δa is about 46%, see Table 4.1).

Another observation is that the conventional NM method tends to generate a more conservative *J*-integral value than that obtained from the proposed *k*-based NM method for deeply-cracked specimens (i.e. a_0/W = 0.5), which is also observed from the validation results of the GTN models. In current analyses, the *k* factor-based NM method reduces the conservatism of the conventional NM method.

Therefore, the above results suggest that the *k* factor-based NM method is effective and can be regarded as a viable alternative method to the UC as well as the conventional NM methods in terms of developing *J-R* curves for SE(T) specimens.

Chapter 5 Summary, conclusions and recommendations

5.1 Summary

The fracture toughness resistance curve (e.g. *J-R* curve) of pipeline steel is a key input to the integrity assessment and strain-based design of oil and gas pipelines with respect to planar defects (i.e. cracks). The SE(T) specimen is becoming more popular for developing the fracture toughness resistance curve in the pipeline industry since the crack-tip stress and strain fields of the SE(T) specimen are more relevant to those of the full-scale pipe containing surface cracks under internal pressure and longitudinal tension. The NM method is an alternative method to develop the *J-R* curves for testing cases where the UC method becomes unfeasible or impractical (e.g. tests involving high loading rates or extreme temperatures or aggressive environments).

In Chapter 2, a comprehensive review of the mechanism of ductile crack growth is presented. The review focuses on the GTN dilatant plasticity model for voided material, which belongs to the category of coupled model as a local approach. The hydrostatic stress and void volume fraction are included in the Gurson yield condition. Nine GTN parameters and two length scale parameters are used to model the nucleation-growth-coalescence of the micro-void in the material. These micromechanical parameters adopted in previous literatures are tabulated in Table A.1.

In Chapter 3, 2D and 3D FEA, in which the GTN dilatant plasticity model is implemented is conducted to study the ductile fracture process for SE(B) and SE(T) specimens made of X80-grade pipeline steel. To this end, the calibration process of the micromechanical parameters is performed. The initiation toughness J_{IC} as well as $J_{1\mathrm{mm}}$ and $J_{1.5\mathrm{mm}}$ are plotted against a_0/W ratio to study the in-plane constraint effect. On top of that, the stress fields near the crack tip and four constraint parameters (i.e. Q, A_2, h, T_Z) are examined based on both stationary-crack and growing-crack analyses.

In Chapter 4, the development of the conventional NM method is first reviewed. As a standardized method to develop *J-R* curves for SE(B) and C(T) specimens, the applicability of NM method for SE(T) specimen is subsequently examined. Next, the so-called '*k* factor-based' NM method is proposed based on the J-CMOD relationship to improve the efficiency of the conventional NM method. As for the application of the proposed 'k factor-based' NM method, an empirical k equation is derived for SE(T) specimens with various geometric configurations and hardening properties.

5.2 Conclusions

The main conclusions in this thesis are highlighted and listed as follow:

1). The load-CMOD histories from the GTN models with different D and f_0 values are almost identical. D and f_0 have significant impacts on the J-R curve. A larger D and/or a smaller f_0 value corresponds to an elevated J-R curve. f_F has a negligible impact on the J-R curve. $D/2 = 0.15$ and $f_0 = 0.00015$ are found to give the best match with the experiments.

2). The GTN damage model, in which the calibrated micromechanical parameters are used, is adequate for modelling the ductile fracture process of SE(B) and SE(T) specimens made of X80-grade pipeline steel, in terms of predicting the load-displacement history, J-R curve, and crack plane profile.

3). J_{IC}, J_{1mm} and $J_{\text{1.5mm}}$ are all dependent on initial crack length, and decrease linearly with the increase of a_0/W. Relatively speaking, J_{1mm} and $J_{\text{1.5mm}}$ are strongly dependent on the in-plane constraint level. In contrast, J_{IC} is only weakly dependent on a_0/W.

4). The distribution of $\sigma_{\theta\theta}/\sigma_0$ at the mid-plane ahead of the crack tip is dependent on a_0/W and loading level. For deeply-cracked specimens, the distribution of $\sigma_{\theta\theta}/\sigma_0$ is approximately linear at a distance of $r\sigma_0/J > 1$ ahead of the crack tip, due to the strong bending effect caused by the eccentricity between the applied load and the centroid of the remaining ligament on the crack-tip field.

5). The distribution of $\sigma_{\theta\theta}/\sigma_0$ versus distance from the crack tip (original crack tip in stationary-crack analysis and instantaneous crack tip in growing-crack analysis) at the mid-plane decreases from the mid-plane to free surface at a certain loading level. The stationary-crack and growing-crack analyses result in similar distribution of $\sigma_{\theta\theta}/\sigma_0$.

6). Q, h and T_Z parameters decreases markedly as the loading level and/or the distance from the crack tip increases, while A_2 parameter is almost independent of the loading level and distance from the crack tip. The distribution of the constraint parameters along $1 < r/(J/\sigma_0) < 5$ becomes more sensitive to the loading level as a_0/W increases. As the loading level increases, the distribution of the constraint parameters in growing-crack analysis deviates from that in the stationary-crack analysis.

7). Q and h parameters are well correlated for SE(T) models. As the distance from the crack tip increases, the Q and h parameters are correlated almost linearly. When $r/(J/\sigma_0)$ reaches an 'inflection point', a new linear correlation presents. The T_Z parameter is essentially independent of the Q parameter near the crack-tip region. As $r/(J/\sigma_0)$ reaches an 'inflection point', T_Z becomes linearly correlated to the Q parameter. Similar to the Q-h and Q-T_Z relations, inflection points characterized by certain distances from the crack tip are captured for A_2-h and A_2-T_Z relations. After the 'inflection point' presents, the Q-h and Q-T_Z relations are dependent on the loading level.

8). The NM method is validated to be effective to develop J-R curves for SE(T) specimens with various geometric configurations. Error analyses of the test specimens show that for both shallow-cracked and deeply-cracked SG specimens at the crack extension of $\Delta a \geq 2.0$ mm, e_{J1} is within 15%, while for deeply-cracked PS specimens, e_{J1} can be over 20% because of the inaccurate crack length estimation performed by the UC method. Error analyses of the GTN models show that at the crack extension of $\Delta a \geq 1.0$ mm, e_{J1} is generally small. For shallow-cracked models (i.e. $a_0/W < 0.3$), e_{J1} is within 15%. For deeply-cracked models (i.e. $a_0/W > 0.3$), e_{J1} is within 8%.

9). A so-called 'k factor-based' NM method is proposed to overcome the cumbersome integrative procedure required to normalize load-CMOD pairs and the inaccuracy involved when evaluating the instantaneous compliance. For the application of the k factor-based NM method, the k equation and Table 4.4 are applied for SE(T) specimens with various geometric configurations and hardening properties.

10). The conventional NM method tends to yield a more conservative *J*-integral value than that derived from the proposed *k*-based NM method for deeply-cracked specimens. In current analyses, the *k* factor-based NM method reduces the conservatism of the *J-R* curves obtained from the conventional NM method. The *k* factor-based NM method obtained from the stationary-crack analysis is proved to be effective, and can be regarded as an alternative method to the UC method as well as the conventional NM method.

5.3 Recommendations

Some of the limitations and corresponding recommendations for future research are listed as follows:

1). For other types of material (i.e. different grades of steels and alloys) as well as other specimens (e.g. SE(B) and C(T) specimens), the *k* factor-based NM method needs to be verified. Also, the fitting coefficients α and β for other types of materials and specimens considering a_0/W, n, and PS/SG need to be found. In addition, the proposed *k* factor-based NM method needs additional experiments to verify. A suitable series of experimental studies need to be conducted in the future.

2). In the current study, only homogeneous material is considered. However, pipelines installed in seismic or permafrost regions need to possess sufficient material resistance against buckling or weld fracture caused by large ground movements [98]. The regions near the girth weld joints with surface notch in the weld metal or HAZ are prone to form local strain concentration, ductile fracture initiation and growth, as well as plastic instability and even brittle cleavage due to the non-homogeneous nature of the material. In this case, the material constraint can be characterized by the strength mismatch ratio (σ_{M1}/σ_{M2}, where σ_{M1} and σ_{M2} denotes the yield strength of material 1 and 2, respectively) and the hardening mismatch deviation (n_{M1}- n_{M2}, where n_{M1} and n_{M2} denotes the hardening exponent of material 1 and 2, respectively). Further study can be focused on calibrating the micromechanical parameters and modelling the fracture process for bi-material specimens with non-homogeneous nature.

3). Constraint effect on the upper-shelf, mode I fracture toughness of ferritic steels is a key issue for the safety assessment of pipeline [53]. The geometry constraint (i.e. crack depth a/W, specimen thickness B, specimen width W, specimen size, loading mode (e.g. bending or tension) and material mismatch (i.e. strength mismatch and work hardening mismatch) can individually as well as correlatively [85, 87, 146] pose effect on the fracture toughness. In addition, the micromechanical effect may also be involved [60]. In future study, the in-plane and out-of-plane constraint effects based on a more comprehensive set of 3D GTN models need to be investigated on both global and local aspects.

4). 3D FEA was previously conducted by Huang et al. [122] to develop the constraint-corrected *J-R* curves for the X80-grade pipeline steels. A given *J-R* curve was associated with a given value of the constraint parameter through correlating the power-law coefficients C_1 and C_2 with the constraint parameter. Throughout their study, stationary-crack analysis was adopted and only SE(B) specimens were considered. In future study, with the application of the current GTN models, the constraint-corrected *J-R* curves by incorporating the experimentally determined *J-R* curves and constraint parameters for SE(T) specimens as well as real pipe sections can be developed based on growing-crack analysis.

5). Existing empirical *m*-factor equation (which correlates *J*-integral and CTOD) for SE(T) specimen can be found in the studies by Shen el al. [147], Ruggieri [148], Huang et al. [145] and Sarzosa et al. [101]. Some preliminary analyses have shown that for current GTN models, after a transitional behavior early in the loading (which is most likely associated with the intense crack-tip blunting), the *m* value for shallow-cracked specimens (e.g. $a_0/W \le 0.35$) attains an essentially constant value independent of the loading level, which is consistent with the result in [101]. In addition, it is found that the *m*-equation proposed in [145] gives an asymptotic result for deeply-cracked specimens at a higher loading level, and predicts better results than those given in any other studies. Future study will be focused on the systematic comparison of the *m*-factor equations in the above-mentioned studies based on the current GTN-based FE models.

Appendix A

Table A. 1 Micromechanical parameters from literature

Reference	Specimen	Material	D/2 [mm]	q_1	q_2	q_3	f_0	f_C	f_F	ε_N	s_N	f_N	Dimension
[5]	C(T); pipe specimens with different crack sizes and depths	X60	0.1	1.43	0.83	2.0449	0.008	-	0.2	-	-	-	2D
[26]	SE(B)	Two base materials MB1 MB2; weld material	0.1	1.5	1	2.25	0.0001	CGM	0.15	0.3	0.1	0.004	2D; 3D
[30]	Notched tensile specimen	A992 steel	0.075	1.5	1	2.25	0	0.03	0.5	0.45	0.05	0.02	3D
[50]	Smooth tensile specimen; unit cell under biaxial tension	X65 Al-4.3%Si Alloy	0.1	1.25	1	1.5625	0.002 0.0008	-	0.15	-	-	-	2D
[51]	Round tensile bar	Copper	-	1.5	1	2.25	0	0.15	0.25	0.3	0.1	0.04	2D
[53]	SE(B); C(T)	A533B A516-70	0.1 0.125	1.5	1	2.25	0.0035 0.002	-	0.15	0.75	0.05	0.5	2D; 3D
[54]	Unit cell with different void shapes	GGG40/1AZ GGG40/3AZ	0.3 × 0.4 0.6 × 0.8	1.2	1	1.44	0.114 0.12	0.175	0.235	-	-	-	2D
[60]	SE(B); SE(T)	Power law hardening	0.1 × 0.05	1.5	1	2.25	0.005 0.0005	CGM	0.21 0.201	-	-	-	2D
[61]	SE(T)	X100	0.1 × 0.05	1.5	1	2.25	0.0005	CGM	0.20005	-	-	-	2D
[62, 149]	Surface-cracked wide tension plate; SE(T)	X70	0.25 0.1	1.43	0.95	2.0449	0.002	CGM	0.19	0.3	0.1	0.00018	3D

Reference	Specimen	Material	$D/2$ [mm]	q_1	q_2	q_3	f_0	f_C	f_F	ε_N	s_N	f_N	Dimension
[64]	Notched tension bar	X65	[0.05,0.15]	1.508	0.913	2.2741	[0.0025, 0.005]	-	0.15	0.9	[0.01, 0.05]	[0.04,0.1]	2D SSY; 3D
[65]	SE(B); SE(T)	214Cr1Mo	0.15	2	0.77	4	0.0035	-	[0.1,0.2]	-	-	-	3D
[66]	Medium curved wide plate; SE(T); SE(B)	Base metal X65; Girth weld metal X80 GMAW	0.1	1.517 1.386	0.916 0.972	2.3 1.92	0.0001	-	0.15	-	-	-	3D
[71]	C(T); pipe specimen with external/ internal longitudinal flaws	X60	0.1	1.47	0.94	2.1609	0.02	-	0.2	-	-	-	2D; 3D
[72]	(non)preloaded SE(B); notched test specimen	A533B-1	0.125	1.64	0.87	2.6896	0.0065	0.1	0.2	-	-	-	3D
[73]	Tensile notched round specimen; C(T)	NiCr steel (12NC6)	0.2	1.5	1	2.25	0.00001	0.004	0.335	A_1=0.001			2D
[74]	Smooth and notched tensile bars with different notch radii; SE(B); plate specimen	X65	0.15	1.5	1	2.25	0.000125 0.00014 0.0002	0.015	0.25	0.3	0.1	0.0008	2D; 3D
[82]	Square plate specimen; tensile coupon	Grade A (Lloyd's) steel	0.05	1.5	1	2.25	0	0.07	0.1	0.1979	0.01	0.0294	2D; 3D
[85]	SE(B); SE(T)	Power law hardening	0.1 × 0.05	1.5	1	2.25	0.002	CGM	-	-	-	-	2D
[86, 87]	SE(B); SE(T); C(T); CCT	Low-alloy steel A508	0.1 × 0.05 0.1 × 0.1	1.5	1	2.25	0.0002	0.04	0.17	0.3	0.1	0.002	2D; 3D

Reference	Specimen	Material	$D/2$ [mm]	q_1	q_2	q_3	f_0	f_C	f_F	ε_N	s_N	f_N	Dimension
[90, 107]	DET specimen; pipe section; SE(B); SE(T)	X65 X80 X100	0.25 0.25 0.2	1.5	1	2.25	0.00015	0.02	-	0.3	0.1	0.0005 0.00015 0.005	3D
[91]	SE(B); SE(T)	X65	0.125	1.5	1	2.25	0.00015	0.13	0.1503	-	-	-	3D
[92]	U-notched tension bar	Iron with equiaxed grains	-	1.25	0.95	1.5625	0.06 0.026 0.004	0.12 0.07 0.04	0.25	-	-	-	2D
[98]	Wide plate specimen; notched round bar	X100 X80 X80 girth weld	0.05	1.5	1	2.25	0.0002 0.0002 0.004	0.045 0.08 0.025	-	0.24 0.3 0.3	0.1	0.002 0.005 0.005	2D; 3D
[99]	SE(B)	Ductile medium strength steel	0.1	1.5	1	2.25	0.00015	0.035	0.15	0.3	0.1	0.00085	2D
[100, 101]	SE(B); SE(T); pipe specimen with external circumferential crack	X70	0.1	1.43	0.97	2.0449	0.0005	-	0.15	-	-	-	2D; 3D
[102]	C(T)	BM FZ Al-Mg-Si alloy	0.15 0.035	1.5	1.0 1.5	2.25	0.0115 0.035	0.0195 0.16	0.14893 0.23522	-	-	-	3D
[103]	SE(B)	High-strength low-alloyed steel; over/under-matching filler	0.15	1.5	1	2.25	0.002	0.0188 0.0173 0.0238	0.0188 0.0173 0.0238	-	-	0	2D

Reference	Specimen	Material	$D/2$ [mm]	q_1	q_2	q_3	f_0	f_C	f_F	ε_N	s_N	f_N	Dimension
[104]	SE(B)	BM HAZ WM	0.578 0.497 0.202	1.6	1	2.56	0.0094 0.0086 0.0194	CGM	0.1688 0.1672 0.1888	0.3	0.1	0.014748 0.014748 0.010685	2D
[105]	SE(B)	A508/ A508-N	0.1 × 0.05	1.5	1	2.25	0.00008	0.04	0.25	0.3	0.1	0.002	2D
[106]	MT; SE(B); SE(T); C(T); pipe section	DIN StE 460	0.1	1.5	1	2.25	0.000675	-	-	0.5	0.05	0.5	2D
[113]	Tensile bar; C(T)	DH36	0.05	1.5	1	2.25	0.001	0.15	0.25	-	-	-	3D
[150]	C(T); SE(T)	C-Mn steel	0.2	1.5	1	2.25	0.002	0.004	-	-	-	-	2D
[151]	Cylindrical cell	22 NiMoCr37	-	1.15	1	1.3225	0.002	0.033	0.15	0.3	0.1	0.004	3D
[152]	Axisymmetric notched specimen	C-Mn steel	0.25	1.5	1	2.25	0.0023	0.004	-	-	-	-	2D
[153]	C(T)	GGG40 ferritic cast iron	0.1	1.5	1	2.25	0.077	0.12	0.2	-	-	-	2D; 3D
[154]	Round bar; circumferentially notched specimen	C-Mn Alloy	0.1	1	1.25	1	[0.0015, 0.005]	-	[0.15,0.2]	-	-	-	3D
[155]	SE(B)	A580 Alloy52Mb Alloy52Mw 316L	0.1 × 0.05	1.5	1	2.25	0.00008 0.000001 0.00015 0.000001	0.04	0.25	0.3	0.1	0.02	2D
[156]	Notch tip and hole	Power law hardening	-	1.5	1	2.25	-	0.15	0.25	0.3	0.1	0.04	2D
[157]	Tensile specimen; SE(B)	Al-Al3Ti composite	0.186 × 0.213	1.5	1	2.25	0.08 0 0 0	0.15 0.02 0.2 0.15	0.28 0.34 0.32 0.28	0 0.5 0.05 0.025	0 0.2 0.02 0.025	0 0.04 0.4 0.08	2D

Reference	Specimen	Material	$D/2$ [mm]	q_1	q_2	q_3	f_0	f_C	f_F	ε_N	s_N	f_N	Dimension
[158]	Unit cell	Porous ductile material	-	1.5	1	2.25	0	0.04	0.195	0.3	0.1	0.008	3D
[159]	SE(B)	20MnMoNi55 base material; HAZ; cladding	0.1	1.5	1	2.25	0	0.06 0.04 0.03	0.212 0.197 0.189	0.3	0.1	0.002 0.002 0.012	2D; 3D
[160]	C(T); middle tension (MT)	StE460	0.1	1.5	1	2.25	0.0025	0.02	0.02747	0.3	0.1	0.02	2D
[161]	Flat plate buttwelded at midsection	St52-3N (CMn)	0.033	1.25	1	2.25	0.00033	0.026	0.15	0.3	0.1	0.006	3D
[162]	Smooth/notched round tension bars; C(T)	A710	0.075	1.5	1	2.25	0.00057	0.03	0.15	0.3	0.1	0.004	2D
[163]	SE(B)	A508 Alloy 82 Alloy 182 316L	0.1 × 0.05	1.5	1	2.25	0.005 0.004 0.001 0.000001	0.05	0.3	0.3	0.1	0.008 0 0.008 0.0055	2D
[164]	SE(B); double edge notched tension panel; center cracked panel	A533B	0.1	1.25	1	1.5625	0.005	-	0.2	0.04	0.01	0.001	2D
[165]	Smooth tensile specimen; center cracked tensile panel	22 NiMoCr37	0.125	1.5	1	2.25	[0.0005, 0.002]	[0.0019, 0.0145]	0.2	0.3	0.1	[0.00075, 0.003]	2D

Appendix B

Equations of K, C, F_r, η_{pl} and γ_{LLD} for SE(T) specimen

1. Stress intensity factor K:

$$K_i = \left[\frac{P_i\sqrt{\pi a}}{W\sqrt{BB_N}}\right] G\left(\frac{a_i}{W}\right) \tag{B.1}$$

where

$$G\left(\frac{a}{W}\right) = \sum_{i=1}^{12} t_i \left(\frac{a}{W}\right)^{i-1} \tag{B.2}$$

The parameters t_i (i = 1 to 12) are tabulated in Table B.1.

2. Compliance C:

$$C_i = \frac{\frac{2a_i}{W} F\left(\frac{a_i}{W}\right)}{BE\left(1 - \frac{a_i}{W}\right)^2} \tag{B.3}$$

where

$$F\left(\frac{a}{W}\right) = \sum_{i=1}^{7} u_i \left(\frac{a}{W}\right)^{i-1} \tag{B.4}$$

The parameters u_i (i = 1 to 7) are tabulated in Table B.2. Note that for SG specimens, the effective thickness B_e should be used, where B_e is given as:

$$B_e = B - \frac{(B - B_N)^2}{B} \tag{B.5}$$

where

B_N denoting the net thickness.

3. Rotation correction factor F_r:

$$F_r = \frac{C_0}{C_i} = \frac{1}{1 - 0.165\,\frac{a}{W}\left(\frac{P}{P_Y}\right)} \tag{B.6}$$

where

C_0 is the compliance of the un-deformed specimen;

C_i is the compliance of the deformed specimen;

P_Y is the limit load for the specimen given as:

$$P_Y = B_N(W - a)\sigma_Y \tag{B.7}$$

4. Plastic factor η_{pl}:

$$\eta_{pl} = \sum_{i=0}^{2} q_i \left(\frac{a}{W}\right)^i \tag{B.8}$$

where

$$q_i = \sum_{j=0}^{3} N_{ij} \left(\frac{\sigma_{YS}}{\sigma_{TS}}\right)^j \tag{B.9}$$

The parameters N_{ij} (i = 0 to 2; j = 0 to 3) are tabulated in Table B.3.

5. Plastic factor γ_{LLD}:

$$\gamma_{LLD} = 1 - \eta_{LLD} - \left(1 - \frac{a}{W}\right)\frac{\eta'_{LLD}}{\eta_{LLD}} \tag{B.10}$$

where

$$\eta_{LLD} = \sum_{i=0}^{10} \psi_i \left(\frac{a}{W}\right)^i \tag{B.11}$$

$$\eta'_{LLD} = \sum_{i=1}^{10} i\psi_i \left(\frac{a}{W}\right)^{i-1} \tag{B.12}$$

The parameters ψ_i (i = 0 to 10) are tabulated in Table B.4.

Table B. 1 Coefficients t_i for K_i

i	1	2	3	4	5	6
t_i	1.197	-2.133	23.886	-69.051	100.462	-41.397
i	7	8	9	10	11	12
t_i	-36.137	51.215	-6.607	52.3222	18.574	19.465

Table B. 2 Coefficients u_i for C_i

i	1	2	3	4	5	6	7
u_i	2.9086	-5.8808	20.3409	-53.8231	96.017	-101.172	41.6725

Table B. 3 Coefficients N_{ij} for η_{pl}

		j = 3	j = 2	j = 1	j = 0
Plane-sided	i = 2	19.164	-42.000	29.053	-6.982
	i = 1	-10.250	22.285	-14.340	2.533
	i = 0	-1.282	2.815	-2.474	1.708
Side-grooved	i = 2	25.040	-42.248	20.037	-3.196
	i = 1	-23.177	36.942	-15.685	1.261
	i = 0	4.645	-6.629	2.244	0.946

Table B. 4 Coefficients ψ_i for γ_{LLD}

i	0	1	2	3	4	5	6	7	8	9	10
ψ_i	-0.880	15.190	-35.440	18.644	18.399	-1.273	-12.756	-12.202	-4.447	5.397	14.187

Appendix C

Table C. 1 Coefficients of NM function for test SE(T) specimens

Specimen ID	SE(T)-PS05-01	SE(T)-PS05-02	SE(T)-SG05-01	SE(T)-SG05-02	SE(T)-SG25-01	SE(T)-SG25-02
L	3.986	3.622	5.260	5.258	2.717	2.416
M	675.811	679.875	723.904	709.151	727.981	730.981
N	-587.808	-627.556	-227.084	-390.020	363.435	361.833
O	0.017	0.014	0.017	0.019	0.008	0.007

Table C. 2 Coefficients of NM function for GTN-based FE SE(T) models

				PS B/W=1			
a_0/W	0.2	0.25	0.3	0.35	0.4	0.45	0.5
L	1.042	1.284	2.678	2.497	4.371	5.519	7.603
M	762.863	750.795	748.659	719.553	732.975	736.662	757.929
N	638.295	756.145	797.289	1024.875	878.173	734.944	497.230
O	0.004	0.004	0.008	0.007	0.012	0.015	0.020
				SG B/W=1			
a_0/W	0.2	0.25	0.3	0.35	0.4	0.45	0.5
L	3.668	5.727	7.270	9.693	11.923	12.054	13.660
M	831.841	860.454	859.536	873.374	896.489	888.834	907.959
N	-234.486	-394.157	-304.560	-358.425	-587.067	-662.263	-1174.445
O	0.009	0.013	0.017	0.023	0.029	0.030	0.036
				PS B/W=0.5			
a_0/W	0.2	0.25	0.3	0.35	0.4	0.45	0.5
L	1.734	2.695	5.095	6.959	9.171	10.758	8.932
M	748.115	748.892	761.996	775.012	800.618	824.953	786.079
N	418.968	422.115	365.740	287.412	77.270	-193.765	-52.231
O	0.005	0.008	0.013	0.018	0.024	0.029	0.026

References

1. Murray, A. and Paviglianiti, J. (2011). Pipeline regulation in Canada, Integrity of Pipelines Transporting Hydrocarbons, Springer, Dordrecht, p. 27-36.

2. Lam, C. (2015). Statistical analyses of historical pipeline incident data with application to the risk assessment of onshore natural gas transmission pipelines. M.E.Sc Thesis, Western University, London, Canada.

3. Zhou, W. (2016). Introduction to pipeline design and assessment, Second edition. Lecture notes, Western University, London, Canada.

4. Anderson, T. L. (2005), Fracture mechanics: fundamentals and applications, Third edition. CRC Press, Boca Raton.

5. Dotta, F. and Ruggieri, C. (2004). Structural integrity assessments of high pressure pipelines with axial flaws using a micromechanics model. International Journal of Pressure Vessels & Piping, 81(9): 761-770.

6. Hutchinson, J. W. (1983). Fundamentals of the phenomenological theory of nonlinear fracture mechanics. Journal of Applied Mechanics, 50(4b): 1042-1051.

7. Rice, J. R. (1968). A path independent integral and the approximate analysis of strain concentration by notches and cracks. Journal of Applied Mechanics, 35: 379-86.

8. Wells, A. A. (1961). Unstable crack propagation in metals: cleavage and fast fracture. Proceedings of the Crack Propagation Symposium, 1(84).

9. Hutchinson, J. W. (1968). Singular behaviour at the end of a tensile crack in a hardening material. Journal of the Mechanics & Physics of Solids, 16(1): 13-31.

10. Rice, J. and Rosengren, G. F. (1968). Plane strain deformation near a crack tip in a power-law hardening material. Journal of the Mechanics & Physics of Solids, 16(1): 1-12.

11. Hollstein, T. and Blauel, J. (1977). On the relation of the crack opening displacement to the J-integral. International Journal of Fracture, 13(3): 385-390.

12. ASTM (2017). ASTM E1820-17: Standard Test Method for Measurement of Fracture Toughness. American Society for Testing Materials International, West Conshohocken, PA.

13. Brocks, W. and Schmitt, W. (1995). The second parameter in J-R curves: constraint or triaxiality?. Constraint Effects in Fracture Theory and Applicatons, Second Volume, ASTM International.

14. Tang, H., Macia, M., Minnaar, K., Gioielli, P.,Kibey, S. and Fairchild, D. (2010). Development of the SENT test for strain-based design of welded pipelines. Proceedings of the 8th International Pipeline Conference, IPC.

15. BSI (2014). Method of Test for Determination of Fracture Toughness in Metallic Material Using Single Edge Notched Tension (SENT) Specimens, British Standard Institution, London.

16. Besson, J. (2010). Continuum models of ductile fracture: a review. International Journal of Damage Mechanics, 19(1): 3-52.

17. Larsson, S. G. and Carlsson, A. J. (1973). Influence of non-singular stress terms and specimen geometry on small-scale yielding at crack tips in elastic-plastic materials. Journal of the Mechanics & Physics of Solids, 21(4): 263-277.

18. O'dowd, N. and Shih, C. F. (1991). Family of crack-tip fields characterized by a triaxiality parameter—I. Structure of fields. Journal of the Mechanics & Physics of Solids, 39(8): 989-1015.

19. O'dowd, N. and Shih, C. F. (1992). Family of crack-tip fields characterized by a triaxiality parameter—II. Fracture applications. Journal of the Mechanics & Physics of Solids, 1992. 40(5): 939-963.

20. Yang, S., Chao, Y. and Sutton, M. (1998). Complete theoretical analysis for higher order asymptotic terms and the HRR zone at a crack tip for mode I and mode II loading of a hardening material. Acta Mechanica, 98(1): 79-98.

21. Yang, S., Chao, Y. and Sutton, M. (1993). Higher order asymptotic crack tip fields in a power-law hardening material. Engineering Fracture Mechanics, 45(1): 1-20.

22. Brocks, W. and Schmitt, W. (1993). Quantitative assessment of the role of crack tip constraint on ductile tearing. Constraint Effects in Fracture, ASTM International.

23. Guo, W. (1993). Elastoplastic three dimensional crack border field—I. Singular structure of the field. Engineering Fracture Mechanics, 46(1): 93-104.

24. Guo, W. (1993). Elastoplastic three dimensional crack border field—II. Asymptotic solution for the field. Engineering Fracture Mechanics, 46(1): 105-113.

25. Guo, W. (1995). Elasto-plastic three-dimensional crack border field—III. Fracture parameters. Engineering Fracture Mechanics, 51(1): 51-71.

26. Penuelas, I., Betegon, C. and Rodriguez, C. (2006). A ductile failure model applied to the determination of the fracture toughness of welded joints. Numerical simulation and experimental validation. Engineering Fracture Mechanics, 73(18): 2756-2773.

27. Betegón, C. and Peñuelas, I. (2006). A constraint based parameter for quantifying the crack tip stress fields in welded joints. Engineering Fracture Mechanics, 73(13): 1865-1877.

28. Lemaitre, J. (1986). Local approach of fracture. Engineering Fracture Mechanics, 25(5-6): 523-537.

29. Sun, D. Z., Kienzler, R., Voss, B. and Schmitt, W. (1992). Application of micromechanical models to the prediction of ductile fracture. Fracture Mechanics: Twenty-Second Symposium, Volume II, ASTM International.

30. Kiran, R. and Khandelwal, K. (2014). Gurson model parameters for ductile fracture simulation in ASTM A992 steels. Fatigue & Fracture of Engineering Materials & Structures, 37(2): 171-183.

31. Rice, J. R. and Tracey, D. M. (1969). On the ductile enlargement of voids in triaxial stress fields∗. Journal of the Mechanics & Physics of Solids, 17(3): 201-217.

32. Scheider, I. and Brocks, W. (2003). Simulation of cup–cone fracture using the cohesive model. Engineering Fracture Mechanics, 70(14): 1943-1961.

33. Cornec, A., Scheider, I. and Schwalbe, K. H. (2003). On the practical application of the cohesive model. Engineering Fracture Mechanics, 70(14): 1963-1987.

34. Tai, W. H. and Yang, B. X. (1986). A new microvoid-damage model for ductile fracture. Engineering Fracture Mechanics, 25(3): 377-384.

35. Tai, W. H. and Yang, B. X. (1987). A new damage mechanics criterion for ductile fracture. Engineering Fracture Mechanics, 27(4): 371-378.

36. McClintock, F. A. (1968). A criterion for ductile fracture by the growth of holes. ASME.

37. Thomason, P. (1990). Ductile fracture of metals. Pergamon Press plc, Ductile Fracture of Metals (UK), 219.

38. Rousselier, G. (1987). Ductile fracture models and their potential in local approach of fracture. Nuclear Engineering & Design, 105(1): 97-111.

39. Gurson, A. L. (1977). Continuum theory of ductile rupture by void nucleation and growth: Part I—Yield criteria and flow rules for porous ductile media. Journal of Engineering Materials & Technology, 99(1): 2-15.

40. Gurson, A. L. (1977). Plastic flow and fracture behavior of ductile materials incorporating void nucleation, growth, and interaction. PH.D. Thesis, Brown University.

41. Tipper, C. E. (1948). The fracture of mild steel plate: Report No. R. 3. HMSO.

42. Puttick, K. (1959). Ductile fracture in metals. Philosophical Magazine, 4(44): 964-969.

43. Rogers, H. (1960). The tensile fracture of ductile metals. AIME trans, 218(3): 498-506.

44. Gurland, J. and Plateau, J. (1963). The mechanism of ductile rupture of metals containing inclusions. Brown University, Providence; Institut de Recherches de la Siderugie, St.-Germain-en-Laye, France.

45. Goods, S. and Brown, L. (1979). Overview No. 1: The nucleation of cavities by plastic deformation. Acta Metallurgica, 27(1): 1-15.

46. Hahn, G. and Rosenfield, A. (1975). Metallurgical factors affecting fracture toughness of aluminum alloys. Metallurgical Transactions A, 6(4): 653-668.

47. Gardner, R. N., Pollock, T. C. and Wilsdorf, H. G. (1977). Crack initiation at dislocation cell boundaries in the ductile fracture of metals. Materials Science & Engineering, 29(2): 169-174.

48. Garrison, W. and Moody, N. (1987). Ductile fracture. Journal of Physics & Chemistry of Solids, 48(11): 1035-1074.

49. Tvergaard, V. (1989). Material failure by void growth to coalescence. Advances in Applied Mechanics, 27: 83-151.

50. Zhang, Z., Thaulow, C. and Ødegård, J. (2000). A complete Gurson model approach for ductile fracture. Engineering Fracture Mechanics, 67(2): 155-168.

51. Tvergaard, V. and Needleman, A. (1984). Analysis of the cup-cone fracture in a round tensile bar. Acta Metallurgica, 32(1): 157-169.

52. Zhang, Z. and Hauge, M. (1999). On the Gurson micro-mechanical parameters. Fatigue & Fracture Mechanics, 29th Volume, ASTM International.

53. Ruggieri, C., Panontin, T. L. and Dodds, R. (1996). Numerical modeling of ductile crack growth in 3-D using computational cell elements. International Journal of Fracture, 82(1): 67-95.

54. Steglich, D. and Brocks, W. (1997). Micromechanical modelling of the behaviour of ductile materials including particles. Computational Materials Science, 9(1-2): 7-17.

55. Needleman, A. and Rice, J. (1978). Limits to ductility set by plastic flow localization. Mechanics of Sheet Metal Forming, Springer, 237-267.

56. Chu, C. and Needleman, A. (1980). Void nucleation effects in biaxially stretched sheets. Journal of Engineering Materials & Technology (Transactions of the ASME), 102(3): 249-256.

57. Pardoen, T. and Hutchinson, J. W. (2000). An extended model for void growth and coalescence. Journal of the Mechanics & Physics of Solids, 48(12): 2467-2512.

58. Zhang, Z. (1995). Explicit consistent tangent moduli with a return mapping algorithm for pressure-dependent elastoplasticity models. Computer Methods in Applied Mechanics & Engineering, 121(1-4): 29-44.

59. Zhang, Z. (1995). On the accuracies of numerical integration algorithms for Gurson-based pressure-dependent elastoplastic constitutive models. Computer Methods in Applied Mechanics & Engineering, 121(1-4): 15-28.

60. Xu, J., Zhang, Z. L., Østby, E., Nyhus, B., and Sun, D. B. (2009). Effects of crack depth and specimen size on ductile crack growth of SENT and SENB specimens for fracture mechanics evaluation of pipeline steels. International Journal of Pressure Vessels & Piping, 86(12): 787-797.

61. Li, Y., Mao, W., Ji, L. and Huo, C. (2014). The Effect of Constraint on Ductile Crack Growth for Anisotropy Evaluation of X100 Pipeline Steels. Procedia Materials Science, 3: 1505-1511.

62. Chen, Y. and Lambert, S. (2005). Numerical modeling of ductile tearing for semi-elliptical surface cracks in wide plates. International Journal of Pressure Vessels & Piping, 82(5): 417-426.

63. Gullerud, A. S., Gao, X., Dodds, R. H. and Haj-Ali, R. (2000). Simulation of ductile crack growth using computational cells: numerical aspects. Engineering Fracture Mechanics, 66(1): 65-92.

64. Qian, X. (2011). An out-of-plane length scale for ductile crack extensions in 3-D SSY models for X65 pipeline materials. International Journal of Fracture, 167(2): 249-265.

65. Gao, X., Faleskog, J. and Shih, C. F. (1998). Cell model for nonlinear fracture analysis–II. Fracture-process calibration and verification. International Journal of Fracture, 89(4): 375-398.

66. Sarzosa, D. F., Verstraete, M., Hertelé, S., Denys, R. and Ruggieri, C. (2016). Numerical simulation of ductile crack growth in medium wide plate specimens using 3-D computational cells. Engineering Fracture Mechanics, 168: 26-45.

67. Xia, L. and Shih, C. F. (1995). Ductile crack growth—I. A numerical study using computational cells with microstructurally-based length scales. Journal of the Mechanics & Physics of Solids, 43(2): 233-259.

68. Xia, L. and Shih, C. F. (1995). Ductile crack growth—II. Void nucleation and geometry effects on macroscopic fracture behavior. Journal of the Mechanics & Physics of Solids, 43(12): 1953-1981.

69. Faleskog, J., Gao, X. and Shih, C. F. (1998). Cell model for nonlinear fracture analysis–I. Micromechanics calibration. International Journal of Fracture, 89(4): 355-373.

70. Ruggieri, C. and Hippert, E. (2003). Cell model predictions of ductile fracture in damaged pipelines, Fatigue & Fracture Mechanics, 33rd Volume, ASTM International.

71. Ruggieri, C. and Dotta, F. (2011). Numerical modeling of ductile crack extension in high pressure pipelines with longitudinal flaws. Engineering Structures, 33(5): 1423-1438.

72. Bolinder, T. (2014). Numerical simulation of ductile crack growth in residual stress fields. Strålsäkerhetsmyndigheten.

73. Benseddiq, N. and Imad, A. (2008). A ductile fracture analysis using a local damage model. International Journal of Pressure Vessels & Piping, 85(4): 219-227.

74. Oh, C. K., Kim, Y. J., Baek, J. H., Kim, Y. P. and Kim, W. (2007). A phenomenological model of ductile fracture for API X65 steel. International Journal of Mechanical Sciences, 49(12): 1399-1412.

75. Li, Z., Bilby, B. and Howard, I. (1994). A study of the internal parameters of ductile damage theory. Fatigue & Fracture of Engineering Materials & Structures, 17(9): 1075-1087.

76. Tvergaard, V. (1981). Influence of voids on shear band instabilities under plane strain conditions. International Journal of Fracture, 17(4): 389-407.

77. Tvergaard, V. (1982). Ductile fracture by cavity nucleation between larger voids. Journal of the Mechanics & Physics of Solids, 30(4): 265-286.

78. Koplik, J. and Needleman, A. (1988). Void growth and coalescence in porous plastic solids. International Journal of Solids & Structures, 24(8): 835-853.

79. Perrin, G. and Leblond, J. (1990). Analytical study of a hollow sphere made of plastic porous material and subjected to hydrostatic tension-application to some problems in ductile fracture of metals. International Journal of Plasticity, 6(6): 677-699.

80. Rostoker, W. and Dvorak, J. R. (2012). Interpretation of metallographic structures. Elsevier.

81. Devaux, J. C., Mudry, F., Pineau, A. and Rousselier, G. (1988). Experimental and numerical validation of a ductile fracture local criterion based on a simulation of cavity growth. Nonlinear Fracture Mechanics: Volume II Elastic-Plastic Fracture, ASTM International.

82. Cuesta, I., Alegre, J. and Lacalle, R. (2010). Determination of the Gurson–Tvergaard damage model parameters for simulating small punch tests. Fatigue & Fracture of Engineering Materials & Structures, 33(11): 703-713.

83. Le Roy, G., Embury, J. D., Edwards, G. and Ashby, M. F. (1981). A model of ductile fracture based on the nucleation and growth of voids. Acta Metallurgica, 29(8): 1509-1522.

84. Shih, C. (1981). Relationships between the J-integral and the crack opening displacement for stationary and extending cracks. Journal of the Mechanics & Physics of Solids, 29(4): 305-326.

85. Østby, E., Thaulow, C. and Zhang, Z. (2007). Numerical simulations of specimen size and mismatch effects in ductile crack growth–Part I: Tearing resistance and crack growth paths. Engineering Fracture Mechanics, 74(11): 1770-1792.

86. Yang, J., et al., Unified characterisation of in-plane and out-of-plane constraint based on crack-tip equivalent plastic strain. Fatigue & Fracture of Engineering Materials & Structures, 2013. 36(6): 504-514.

87. Yang, J., Wang, G. Z., Xuan, F. Z. and Tu, S. T. (2014). Unified correlation of in-plane and out-of-plane constraints with fracture toughness. Fatigue & Fracture of Engineering Materials & Structures, 37(2): 132-145.

88. Franklin, A. (1969). Comparison between a quantitative microscope and chemical methods for assessment of non-metallic inclusions. Journal of the Iron & Steel Institute, 207(2): 181-186.

89. Sun, D. Z., Siegele, D., Voss, B. and Schmitt, W. (1989). Application of local damage models to the numerical analysis of ductile rupture. Fatigue & Fracture of Engineering Materials & Structures, 12(3): 201-212.

90. Nonn, A. and Kalwa, C. (2010). Modelling of damage behaviour of high strength pipeline steel. Proceedings of the 18th European Conference on Fracture, Dresden, Germany.

91. Han, K., Shuai, J., Deng, X., Kong, L., Zhao, X. and Sutton, M. (2014). The effect of constraint on CTOD fracture toughness of API X65 steel. Engineering Fracture Mechanics, 124: 167-181.

92. Becker, R., Needleman, A., Richmond, O. and Tvergaard, V. (1988). Void growth and failure in notched bars. Journal of the Mechanics & Physics of Solids, 36(3): 317-351.

93. Zhang, Z. and Niemi, E. (1994). A new failure criterion for the Gurson-Tvergaard dilational constitutive model. International Journal of Fracture, 70(4): 321-334.

94. Guillemer-Neel, C., Bobet, V. and Clavel, M. (1999). Cyclic deformation behaviour and Bauschinger effect in ductile cast iron. Materials Science & Engineering: A, 272(2): 431-442.

95. Dybwad, J., Törnqvist, R., Østby, E. and Thaulow, C. (2009). Simulations of ductile tearing at large strains of biaxially loaded pipes. International Conference on Offshore Mechanics & Arctic Engineering (OMAE), Honolulu, Hawaii, USA.

96. Kwon, D. and Asaro, R. (1990). A study of void nucleation, growth, and coalescence in spheroidized 1518 steel. Metallurgical & Materials Transactions A, 21(1): 117-134.

97. Qiu, H., Mori, H., Enoki, M. and Kishi, T. (1999). Evaluation of ductile fracture of structural steels by microvoid model. ISIJ international, 39(4): 358-364.

98. Ishikawa, N., Sueyoshi, H. and Igi, S. (2010). Application of damage mechanics modeling to strain based design with respect to ductile crack initiation. Proceedings of the 8th International Pipeline Conference, Alberta, Canada.

99. Betegon, C., Rodriguez, C. and Belzunce, F. (1997). Analysis and modelisation of short crack growth by ductile fracture micromechanisms. Fatigue & Fracture of Engineering Materials & Structures, 20(5): 633-644.

100. Sarzosa, D. F. and Ruggieri, C. (2014). A numerical investigation of constraint effects in circumferentially cracked pipes and fracture specimens including ductile tearing. International Journal of Pressure Vessels & Piping, 120: 1-18.

101. Sarzosa, D.F., Souza, R. F. and Ruggieri, C. (2015). J–CTOD relations in clamped SE(T) fracture specimens including 3-D stationary and growth analysis. Engineering Fracture Mechanics, 147: 331-354.

102. Nègre, P., Steglich, D. and Brocks, W. (2004). Crack extension in aluminium welds: a numerical approach using the Gurson–Tvergaard–Needleman model. Engineering Fracture Mechanics, 71(16): 2365-2383.

103. Rakin, M., Gubeljak, N., Dobrojević, M. and Sedmak, A. (2008). Modelling of ductile fracture initiation in strength mismatched welded joint. Engineering Fracture Mechanics, 75(11): 3499-3510.

104. Younise, B., Sedmak, A., Rakin, M., Gubeljak, N., Medjo, B., Burzić, M. and Zrilić, M. (2012). Micromechanical analysis of mechanical heterogeneity effect on the ductile tearing of weldments. Materials & Design, 37: 193-201.

105. Fan, K., Wang, G. Z., Tu, S. T. and Xuan, F. Z. (2016). Geometry and material constraint effects on fracture resistance behavior of bi-material interfaces. International Journal of Fracture, 201(2): 143-155.

106. Hippert, E., Dotta, F. and Ruggieri. C. (2002). Structural integrity assessments of pipelines using crack growth resistance curves. Proceedings of the 4th International Pipeline Conference, ASME.

107. Scheider, I., Nonn, A., Völling, A., Mondry, A. and Kalwa, C. (2014). A damage mechanics based evaluation of dynamic fracture resistance in gas pipelines. Procedia Materials Science, 3: 1956-1964.

108. Tvergaard, V. and Needleman, A. (1992). Effect of crack meandering on dynamic, ductile fracture. Journal of the Mechanics & Physics of Solids, 40(2): 447-471.

109. Tvergaard, V. and Needleman, A. (1993). An analysis of the brittle-ductile transition in dynamic crack growth. International Journal of Fracture, 59(1): 53-67.

110. Mathur, K., Needleman, A. and Tvergaard, V. (1994). 3D analysis of failure modes in the Charpy impact test. Modelling & Simulation in Materials Science & Engineering, 2(3A): 617.

111. Needleman, A. and Tvergaard, V. (1994). Mesh effects in the analysis of dynamic ductile crack growth. Engineering Fracture Mechanics, 47(1): 75-91.

112. Nahshon, K. and Hutchinson, J. W. (2008). Modification of the Gurson model for shear failure. European Journal of Mechanics-A/Solids, 27(1): 1-17.

113. Xue, Z., Pontin, M. G., Zok, F. W. and Hutchinson, J. W. (2010). Calibration procedures for a computational model of ductile fracture. Engineering Fracture Mechanics, 77(3): 492-509.

114. Wang, E., Zhou, W., Shen, G. and Duan, D. (2012). An experimental study on J (CTOD)-R curves of single edge tension specimens for X80 steel. Proceedings of the International Pipeline Conference (IPC2012).

115. ASTM (2016). ASTM E8/E8M-16a: Standard Test Methods for Tension testing of Metallic Materials. American Society of Testing and Materials International, West Conshohocken, PA.

116. Simulia, D. S. (2013). ABAQUS 6.13 User’s manual. Dassault Systems, Providence, RI.

117. Xia, L., Shih, C. F. and Hutchinson, J. W. (1995). A computational approach to ductile crack growth under large scale yielding conditions. Journal of the Mechanics & Physics of Solids, 43(3): 389-413.

118. Scibetta, M., Lucon, E., Schuurmans, J. and van Walle, E. (2006). Numerical simulations to support the normalization data reduction technique. Engineering Fracture Mechanics, 73(4): 524-534.

119. Zhu, X. K. and Joyce, J. A. (2007). J–resistance curve testing of HY80 steel using SE(B) specimens and normalization method. Engineering Fracture Mechanics, 74(14): 2263-2281.

120. Nyhus, B., Østby, E., Knagenhjelm, H. O., Black, S. and Røstadsand, P. A. (2005). Fracture control—Offshore pipelines: Experimental studies on the effect of crack depth and asymmetric geometries on the ductile tearing resistance. Proceedings of the 24th International Conference on Offshore Mechanics & Arctic Engineering, ASME.

121. Wang, E., Zhou, W. and Shen, G. (2014). Three-dimensional finite element analysis of crack-tip fields of clamped single-edge tension specimens–Part I: Crack-tip stress fields. Engineering Fracture Mechanics, 116: 122-143.

122. Huang, Y., Zhou, W. and Wang, E. (2014). Constraint-corrected J-R curve based on three-dimensional finite element analyses. Fatigue & Fracture of Engineering Materials & Structures, 37(10): 1101-1115.

123. Chao, Y. J. and Zhang, L. (1997). Tables of plane strain crack tip fields: HRR and higher order terms. Department of Mechanical Engineering, University of South Carolina, Technical Report No. ME-Report, 1997: 97-1.

124. Wang, E., Zhou, W. and Shen, G. (2014). Three-dimensional finite element analysis of crack-tip fields of clamped single-edge tension specimens–Part II: Crack-tip constraints. Engineering Fracture Mechanics, 116: 144-157.

125. Zhu, X. K. and Joyce, J. A. (2012). Review of fracture toughness (G, K, J, CTOD, CTOA) testing and standardization. Engineering Fracture Mechanics, 85: 1-46.

126. Huang, Y. and Zhou, W. (2014). Investigation of plastic eta factors for clamped SE(T) specimens based on three-dimensional finite element analyses. Engineering Fracture Mechanics, 132: 120-135.

127. Shen, G. and Tyson, W. R. (2009). Crack size evaluation using unloading compliance in single-specimen single-edge-notched tension fracture toughness testing. Journal of Testing & Evaluation, 37(4): 347-357.

128. John, R. and Rigling, B. (1998). Effect of height to width ratio on K and CMOD solutions for a single edge cracked geometry with clamped ends. Engineering Fracture Mechanics, 60(2): 147-156.

129. Ernst, H., Paris, P. C., Rossow, M. and Hutchinson, J. W. (1979). Analysis of load-displacement relationship to determine J-R curve and tearing instability material

properties. Proceedings of the 11th National Symposium on Fracture Mechanics, Part I, ASTM International.

130. Joyce, J., Ernst, H. and Paris, P. (1980). Direct evaluation of J-resistance curves from load displacement records. Fracture Mechanics, ASTM International.

131. Ernst, H., Paris, P. and Landes, J. D. (1981). Estimations on J-integral and tearing modulus T from a single specimen test record. Fracture Mechanics, ASTM International.

132. Sharobeam, M. H., Landes, J. D. and Herrera, R. (1991). Development of eta factors in elastic-plastic fracture testing using a load separation technique. Elastic-plastic fracture test methods: the user's experience (second volume), ASTM International.

133. Joyce, J. A. (2001). Analysis of a high rate round robin based on proposed annexes to ASTM E 1820. Journal of Testing & Evaluation, 29(4): 329-351.

134. Landes, J. D. and Herrera, R. (1988). A new look at J-R curve analysis. International Journal of Fracture, 36(1): R9-R14.

135. Herrera, R. and Landes, J. D. (1988). A direct J-R curve analysis of fracture toughness tests. Journal of Testing & Evaluation, 16(5): 427-449.

136. Herrera, R. and Landes. J. D. (1990). Direct J-R curve analysis: a guide to the methodology. Fracture Mechanics: Twenty-First Symposium, ASTM International.

137. Orange, T. W. (1990). Method and models for R-curve instability calculations. Fracture Mechanics: Twenty-First Symposium, ASTM International.

138. Landes, J. D., Zhou, Z., Lee, K. and Herrera, R. (1991). Normalization method for developing J-R curves with the LMN function. Journal of Testing & Evaluation, 19(4): 305-311.

139. Fortes, C. and Bastian, F. (1997). A modified normalization method for developing J-R and CTOD-R curves with the LMN function. Journal of Testing & Evaluation, 25(3): 302-307.

140. Kong, L. Z., Zhou, X. Y., Chen, L. Q., Huang, K. and Peng, H. T. (2017). CTOD-R curve tests of API 5L X90 by SENT specimen using a modified normalization method. Fatigue & Fracture of Engineering Materials & Structures, 40(2): 288-299.

141. Bolinder, T. and Sattari-Far, I. (2011). Experimental evaluation of influence from residual stresses on crack initiation and ductile crack growth at high primary loads. Strål-Säkerhets-Myndigheten Report, 2011: 19.

142. Qian, X. and Li, Y. (2013). A compliance-based approach to measure fracture resistance curve for surface cracked steel plates. International Journal of Fracture, 182(1): 1-19.

143. Qian, X. and Li, Y. (2013). CMOD-based J integral measurement for surface cracked specimens, ICF13.

144. Sarzosa, D. F. and Ruggieri, C. (2015). Further insights on the relationship between J and CTOD for SE(B) and SE(T) specimens including ductile crack propagation. Proceedings of the ASME 2015 Pressure Vessels & Piping Conference, ASME.

145. Huang, Y. and Zhou, W. (2014). J-CTOD relationship for clamped SE(T) specimens based on three-dimensional finite element analyses. Engineering Fracture Mechanics, 131: 643-655.

146. Østby, E., Thaulow, C. and Zhang, Z. (2007). Numerical simulations of specimen size and mismatch effects in ductile crack growth–Part II: Near-tip stress fields. Engineering Fracture Mechanics, 74(11): 1793-1809.

147. Shen, G. and Tyson, W. R. (2009). Evaluation of CTOD from J-integral for SE(T) specimens. Proceedings of the Pipeline Technology Conference.

148. Ruggieri, C. (2012). Further results in J and CTOD estimation procedures for SE(T) fracture specimens–Part I: Homogeneous materials. Engineering Fracture Mechanics, 79: 245-265.

149. Chen, Y. and Lambert, S. (2003). Analysis of ductile tearing of pipeline-steel in single edge notch tension specimens. International Journal of Fracture, 124(3): 179-199.

150. Bauvineau, L., Burlet, H., Eripret, C. and Pineau, A. (1996). Modelling ductile stable crack growth in a C-Mn steel with local approaches. Le Journal de Physique IV, 6(C6): C6-33-C6-42.

151. Brocks, W., Sun, D. Z. and Ho, A. (1996). Verification of micromechanical models for ductile fracture by cell model calculations. Computational Materials Science, 1996. 7(1-2): 235-241.

152. Decamp, K., Bauvineau, L., Besson, J. and Pineau, A. (1997). Size and geometry effects on ductile rupture of notched bars in a C-Mn steel: experiments and modelling. International Journal of Fracture, 88(1): 1-18.

153. Dong, M. J., Berdin, C., Beranger, A. S. and Prioul, C. (1996). Damage effect in the fracture toughness of nodular cast iron. Le Journal de Physique IV, 6(C6): C6-65-C6-74.

154. Dos Santos, F. and Ruggieri, C. (2003). Micromechanics modelling of ductile fracture in tensile specimens using computational cells. Fatigue & Fracture of Engineering Materials & Structures, 26(2): 173-181.

155. Fan, K., Wang, G. Z., Xuan, F. Z. and Tu, S. T. (2015). Local fracture resistance behavior of interface regions in a dissimilar metal welded joint. Engineering Fracture Mechanics, 136: 279-291.

156. Ghosal, A. and Narasimhan, R. (1996). Numerical simulations of hole growth and ductile fracture initiation under mixed-mode loading. International Journal of Fracture, 77(4): 281-304.

157. He, R., Steglich, D., Heerens, J., Wang, G. X., Brocks, W. and Dahms, M. (1998). Influence of particle size and volume fraction on damage and fracture in Al-Al3Ti composites and micromechanical modelling using the GTN model. Fatigue & Fracture of Engineering Materials & Structures, 21(10): 1189-1201.

158. Kuna, M. and Sun, D. Z. (1996). Three-dimensional cell model analyses of void growth in ductile materials. International Journal of Fracture, 81(3): 235-258.

159. Schmitt, W., Sun, D. Z. and Blauel, J. (1997). Damage mechanics analysis (Gurson model) and experimental verification of the behaviour of a crack in a weld-cladded component. Nuclear Engineering & Design, 174(3): 237-246.

160. Siegmund, T., Bernauer, G. and Brocks. W. (1998). Two models of ductile fracture in contest: porous metal plasticity and cohesive elements. ECF12, Sheffield.

161. Skallerud, B. and Zhang, Z. (1997). A 3D numerical study of ductile tearing and fatigue crack growth under nominal cyclic plasticity. International Journal of Solids & Structures, 34(24): 3141-3161.

162. Sun, D. Z., Voss, B. and Schmitt, W. (1989). Numerical prediction of ductile fracture resistance behaviour based on micromechanical models. EGF9.

163. Wang, H. T., Wang, G. Z., Xuan, F. Z. and Tu, S. T. (2011). Numerical investigation of ductile crack growth behavior in a dissimilar metal welded joint. Nuclear Engineering & Design, 241(8): 3234-3243.

164. Xia, L. and Cheng, L. (1997). Transition from ductile tearing to cleavage fracture: a cell-model approach. International Journal of Fracture, 87(3): 289-305.

165. Zhang, Z. (1996). A sensitivity analysis of material parameters for the Gurson constitutive model. Fatigue & Fracture of Engineering Materials & Structures, 19(5): 561-570.

166. Zhu, X. K., Cravero, S. and Ruggieri, C. (2009). Determination of JR curve for X60 pipeline steel using SENT specimens and normalization method. ASME 2009 Pressure Vessels & Piping Conference, 1219-1224.

Curriculum Vitae

Name:	Cheng Qian
Post-secondary Education and Degrees:	Dalian University of Technology Dalian, Liaoning, China 2011 - 2015, B.E. (Naval Architecture and Offshore Engineering) Delft University of Technology Delft, Netherlands 2014 - 2015, Exchange student (Civil Engineering) The University of Western Ontario London, Ontario, Canada 2016 - 2017, M.E.Sc. (Structural Engineering)
Honours and Awards:	China National Scholarship, Ministry of Education of the People's Republic of China 2013 Western Graduate Research Scholarship, UWO 2016-2017
Related Work Experience	Research Assistant The University of Western Ontario 2016 - 2017 Teaching Assistant The University of Western Ontario 2016 - 2017